國立臺灣大學理學院地質科學系

博士論文

Department of Geosciences

College of Science

National Taiwan University

Doctoral Dissertation

利用衛星大地測量技術分析地表變形與地震行為

Space-based Geodetic Observation in Understanding

Surface Deformation and Earthquakes

童　忻

Hsin Tung

指導教授：胡植慶 博士

陳宏宇 博士

Advisor: Jyr-Ching Hu, Ph.D.

Horng-Yue Chen, Ph.D.

中華民國 108 年 08 月

August 2019

Abstract

Recently, according to the improvements of quantity and quality from satellite-geodetic measurements. Global Positioning System and Interferometric Synthetic Aperture Radar technique have increasingly been applied in geosciences as a powerful tool to monitor land surface deformation. In this study, precise deformation velocity maps of the northern Taiwan area, Taipei, are presented from 2011 to 2013 by using persistent scatterer interferometry technique from high-resolution COSMO-SkyMed (CSK) constellation images. According to the result, the maximum subsidence rates are found in Luzou and Wuku area in the whole dataset. However, dramatic change from severe subsidence to uplift in surface deformation was revealed in the Taipei Basin within two consecutive years which show high correlation with groundwater level change, indicating the relationship between surface deformation and groundwater level is mainly dominated by the confined aquifer. Also, the storativity can be obtained by calculating this relationship. In 2014, Sentinel-1 satellite was launched by ESA, opening a new page on earthquake hazard assessment by its policy of open data access. Instantaneous surface ground motion and permanent displacement induced by two disastrous earthquake from continuous GPS data and SAR images are provided within a short time after the 2016 Meinong earthquake and the 2018 Hualien earthquake, respectively. However, epicenter-away locations of surface rupture indicate surrounding shallow faults and unknown fault system have been triggered during these two events. By comparing the coseismic displacement revealed from daily solution and strong-motion results, the kinematic positioning has proven its reliability of coseismic displacement obtaining within a short time after the main shock and successful to distinguish coseismic displacements of multi-events occurred in a short time span compared to the daily solutions. Moreover, the peak ground displacement (PGD) from the high-rate GPS result show high relationship with damage buildings providing a new factor to earthquake hazard assessment in the future.

Keywords: GPS, InSAR, Land subsidence, Coseismic displacement

摘要

　　近年來，由於衛星資料數量與精度的提升，衛載大地測量已經成為地球科學研究上一項利於觀測地表變形的工具。透過全球衛星定位系統與合成孔徑雷達干涉技術所獲取的大量影像與座標資訊，有助於我們獲得更連續性的地表變形資訊。本研究首先利用持久性散射體雷達干涉技術分析北台灣 2011 年至 2013 年間的高解析度雷達影像，獲得蘆洲與五股為主要下陷區域。然而，若將整體影像分為前後兩年，台北盆地地表變形卻呈現完全相反的劇烈變化。經由計算地表變形與地下水位高的的相關性，可獲得含水層的儲水系數，並且發現台北盆地的地表變形與受壓含水層的地下水位變動有極高的相關性。此外，2014 年歐洲的 Sentinel 衛星升空，其公開的資料讓使用者能在事件發生後於數日內取得及分析，提供防救災全面性的資料，更是將雷達影像應用在地球觀測領域帶入一個新的境界。因此，針對 2016 年的美濃地震及 2018 年的花蓮地震，本研究利用連續 GPS 測站與衛星雷達影像在數天內即獲得瞬間的同震地表變形與永久地表變形行為。結果顯示，兩次地震所測得的最大垂直同震位移都將近 10 公分。但整體而言，同震變形顯示出主要地表破裂區域並非位於震央附近，而是觸發了周圍較淺層的斷層或是其他未知斷層的活動，造成不小的傷亡。此外，利用對比傳統每日解與強震站資料，證明動態 GPS 解算能在地震後短時間內即獲得連續 GPS 測站的同震變形，當連續地震事件發生時，也能避免同震變形估計的干擾。並且，藉由計算高頻 GPS 資料發現房屋倒塌與最大地表位移的高度相關，有望成為未來地震災害評估的一項因子。

關鍵字： 全球定位系統，合成孔徑干涉技術，地表變形，同震變形

致謝

　　博士班生涯終於告一段落。這一篇論文能夠順利完成，首先要感謝我的指導老師－胡植慶博士。感謝老師在研究以及課業方面的協助，給我極高的自由度，讓我選擇研究的目標與方向，鼓勵並提供我多次到國外與學者學習交流的機會。再來要感謝我的共同指導老師－陳宏宇博士。在中研院工作超過十年的時間，感謝老師一路指導我野外大地測量與 GPS 解算的方法與知識、報告上以及研究上的要領，從老師身上，我學到不只是研究上面而更多處事的態度，身為唯一弟子，希望我沒有讓您失望。還要感謝我的指導委員會與口試委員，徐澔德博士、許雅儒博士、饒瑞鈞博士、謝嘉聲博士、林士淵博士以及郭昱廷博士，於學生進度報告、資格考與口試期間撥冗擔任學生的口試委員，對於本論文以及研究上不足之處給予非常多的指導和幫助，使研究與論文更加的完整。除此之外，王國龍老師總是在我低潮的時候給予我正面的回應，從老師身上也學到了對研究的堅持。梁文宗老師總是給與我積極正面的鼓勵，幫助我思考未來。顏君毅老師每次在遙測領域上提供的專業的協助與諮詢，都是讓我前進的動力。

　　除此之外，要特別感謝法國格勒諾布爾大學 Erwan 老師與 Bénédicte 老師、中國地震局地殼應力研究所張景發與李永生老師、英國新堡大學李振洪老師給予我雷達影像操作技術的指導，讓我了解到自己還有許多的不足，真心感謝各位老師，希望我還有機會能向各位老師學習。

　　中研院 416 三朵花的依玲、炘旻，感謝兩位在我每每焦躁的時候配合我、分擔我的工作，謝謝你們這段日子的包容，認識你們，是我很大的收穫。9road 朋友的小渝、一剛、小阿姨、幸芳、阿古、曉慧，因為有你們，我的生活才如此的充實與快樂。GPS 組的宜純、美君、啟賢、周大哥、蘇大哥，還有在這裡認識的好朋友們，在中研院的日子承蒙各位的照顧與幫忙。另外，台大的雅琳、秀芳、琪琪、蚯蚓學長，不需要多說，你們就是我最強的後盾，總是幫我散亂的報告書收尾，提供我豐富的資源。還有實驗室的大小朋友，孟涵、鐘哥、冠全、宣維、

Contents

Appendix I Transient deformation induced by groundwater change in Taipei metropolitan area revealed by high resolution X-bandSAR interferometry X

Appendix II Triggered slip on multifaults after the 2018 Mw 6.4 Hualien earthquake by continuous GPS and InSAR measurements XI

List of Figures

List of Tables

Chapter 1

Introduction

1. 1 Motivation

In the past two decades, the quantity and quality of satellite-geodetic measurements of surface deformation have increased dramatically improving our ability to observe active tectonic processes. In Taiwan, island-wide GPS network contain more than 450 continuous GPS stations was established since 1991 in the area of 36,000 square kilometers (Fig. 1-1). To enhance the near real-time applications, most of the stations equip internet transmission and multi-recording functions of the latest generation dual frequency receivers. These dense continuous GPS data give an excellent opportunity to characterize the interseismic deformation (Hsu et al., 2009;Lin et al., 2010;Min-Chien et al., 2015), coseismic and postseismic deformation (Yu et al., 2003;Hu et al., 2007;Hsu et al., 2011), kinematic positioning (Hung et al., 2017) and calibration of atmosphere effect in InSAR study (Chiang et al., 2009). Abundant information of the geodetic observations provide us good opportunities to study the processes on Earth.

On the other hand, SAR satellites include varies wavelengths provide regional to island scales images in different time periods from 1995 to 2009 with C-band ERS1/2 and ENVISAT satellite, 2007 to 2011 with L-band ALOS satellite, 2011 to 2015 with X-band COSMO_SkyMed Constellation, and from 2014 to nowadays with L-band ALOS-2 and open accessed C-band Sentinel-1A/B satellites. The techniques of extended-SAR images show great potentials for monitoring the regional surface deformation with or without the incorporation the geodetic measurement (Pathier et al., 2003;Chang et al., 2010;Champenois et al., 2012).

2
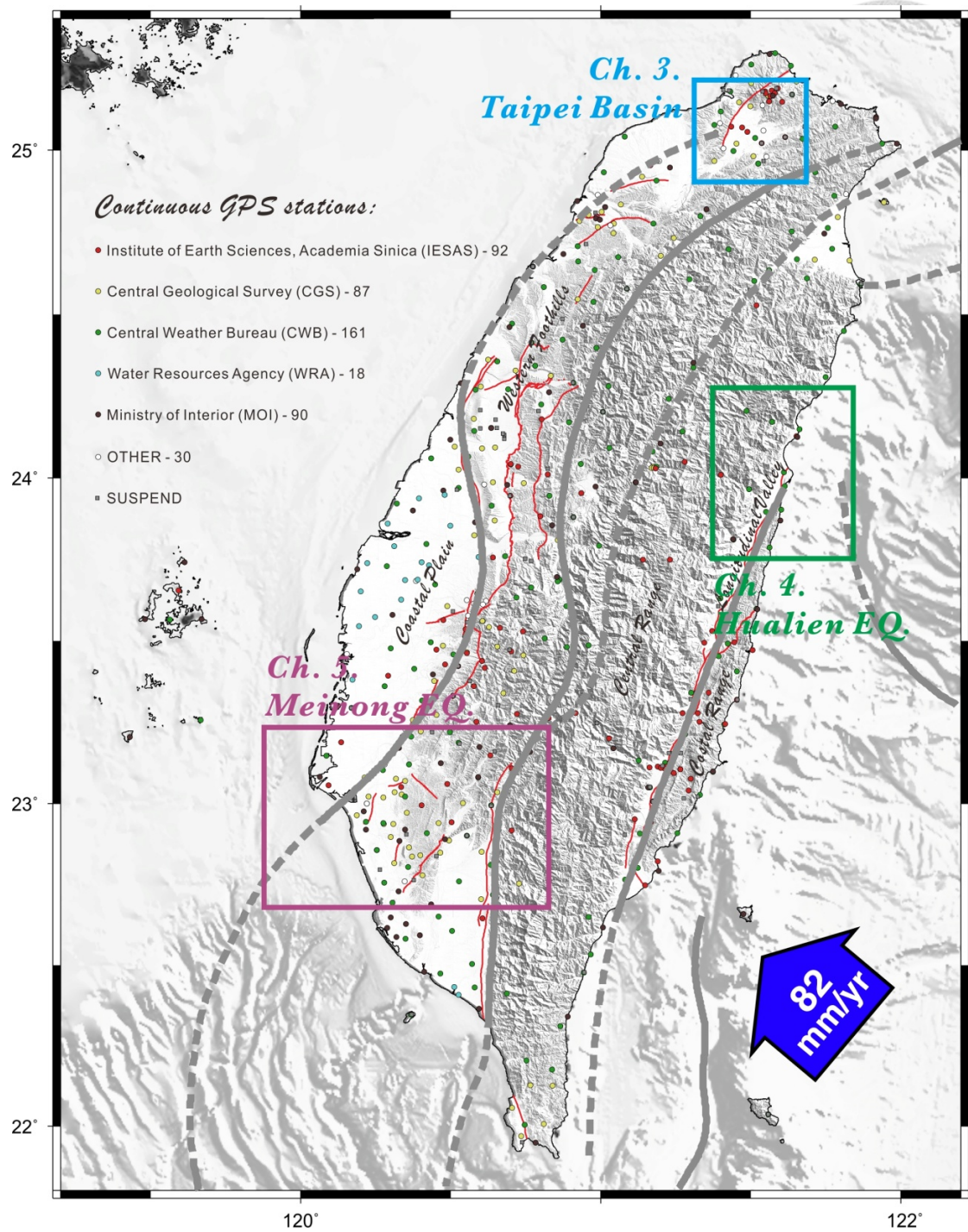
Figure 1-1. Locations for continuous GPS stations (color circles), studies areas in this thesis (color rectangles) and geological divisions in Taiwan. Blue arrow with number represent the convergence rate between Eurasian and Philippine Sea plates (Yu et al., 1997); Lin et al., 2010)

3

Taiwan Island is located along a segment of the oblique convergent boundary between the Philippine Sea Plate and Eurasia Plate, where collision and subduction processes occur (Fig. 1-2). The convergent rate between these two plates is about 82 mm/yr in the N309°E direction (Yu et al., 1997). From west to east, the geological divisions of Taiwan include: The Coastal Plain (CP), Western Foothills (WF), Central Range (CR), Longitudinal Valley (LV) and Coastal Range (CoR) showing various stages of an orogenic evolution from an incipient collision to the South to more mature stages to the North (Ho, 1986). The on-going tectonic processes are highlighted by the high denudation rate, high level of seismicity and disastrous earthquake, makes the young Taiwan orogenic belt become an ideal natural laboratory to study the tectonic processes based on geodetic measurements. Thus, we should routinely respond to earthquake hazard using joint GPS and InSAR observation to map surface ruptures and unknown blind structures according to coseismic and postseismic deformation field. How these geodetic measurements could provide us a robust assessment the kinematic behaviors of seismogenic fault in interseismic period? How deformation evolves with time? Can we capture the transient deformation in time series of GPS and InSAR observations? What are the ability and the challenge to use kinematic position from continuous GPS (cGPS) for near real-time mapping of precise coseismic deformation?
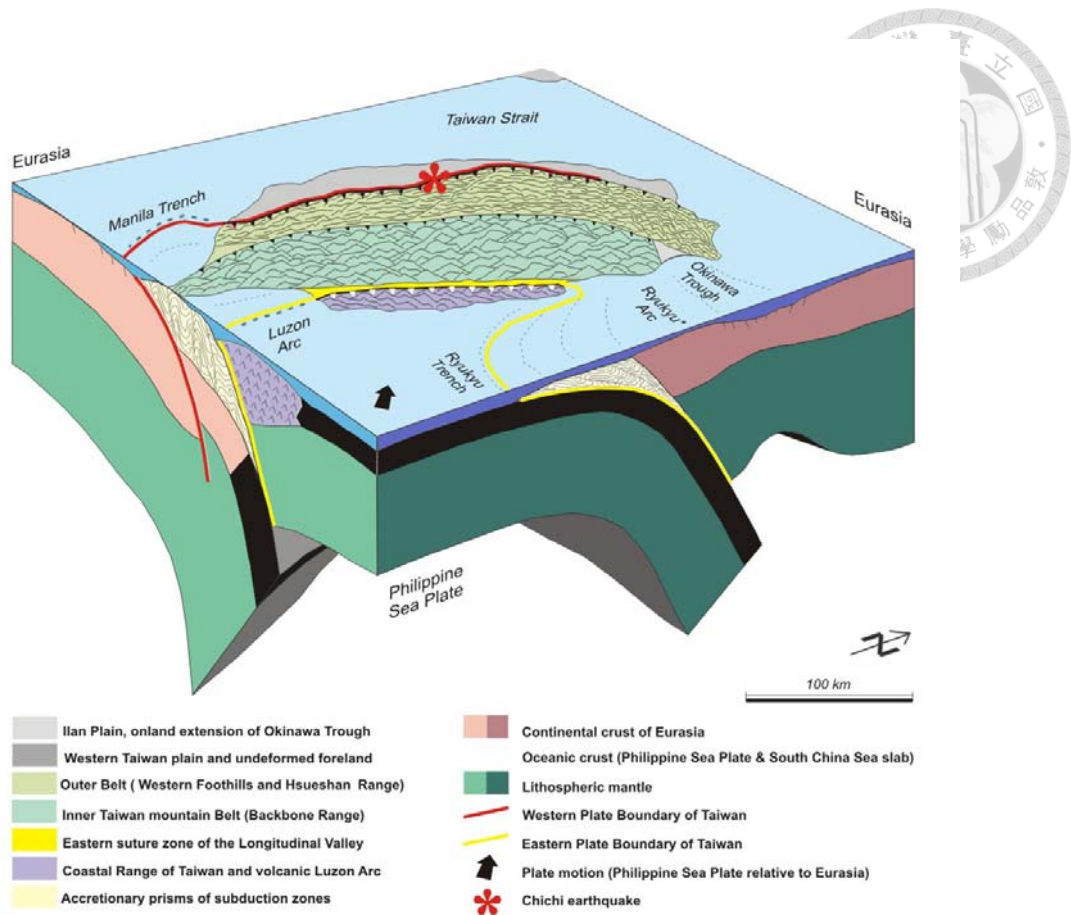
Figure 1-2.   Tectonic framework of Taiwan in 3-D (Angelier et al., 2001).

1. 2 Purpose

The precise measurement of the present-day ground displacements at the scale of the whole Taiwan Island by cGPS and InSAR provide the fundamental knowledge for researchers in several domains of Earth Sciences such as earthquake cycle, earthquake hazard assessment, land subsidence, landslide and active mountain building process. First of all, we routinely process the island-wide cGPS data and provide the mean velocity field and strain rate map. Thus the updated map of mean velocity field and time series could be accessed in the website of TEC (Taiwan Earthquake Center,

5

http://tec.earth.sinica.edu.tw/new_web/index.php) and Taiwan Earthquake Model (TGM). In addition, we also routinely process the InSAR data by Sentinel-1 radar images to provide the deformation map and time series to detect transient deformation. In this research, we study the transient deformation in Taipei basin associated with fluctuations of ground water table due the construction of Mass Rapid Transit (MRT) in Taipei city by using new generation of high resolution X-band SAR data from the COSMO-SkyMed (CSK) constellation. These SAR data provides spatial resolution (between 1x1 and 3x3 m^2) one order of magnitude better than the previous available satellite SAR data, which was been proven that the higher resolution leads to an increase of the density of the measurable targets from 4 up to more than 10 times with respect to those retrieved from medium resolution datasets. Furthermore, the more frequent revisit of the same Area of Interest (AOI) of the present X-band missions counterbalances the possible negative effect of the shorter wavelength on the temporal analysis, in presence of high-rate displacements. By using this high resolution images, substantial improvement in the temporal resolution of deformation time series will be achieved to detect the transient deformation in Taipei basin..

We also focus on the study of seismic deformation induced by big earthquakes in Taiwan by space-based geodetic observations from GPS and InSAR. The InSAR technique had been applied in study of seismic deformation in 1999 Mw 7.6 Chi-Chi earthquake (Pathier et al., 2003) and 2010 Mw 6.2 Jia-Shian earthquake (Huang et al., 2013). Taking advantage of available both ascending and descending modes of radar images, we can now detect the quasi-3D coseismic deformation with different looking angles. These quasi-3D coseismic deformation pattern help us to characterize not only the kinematic behavior of causative faults but also the distribution coseismic slip or afterslip on fault patches of source model. In this study, we focus on coseismic deformation and triggered slip by shallow structures of 2016 Mw 6.4 Meinong earthquake in southwestern Taiwan and 2018 Mw 6.4 Hualien earthquake in eastern

Taiwan (Fig. 1-1). Furthermore, we also use high rate GPS data of cGPS to estimate the coseismic deformation by kinematic position method within a short period. We also use high-rate GPS of cGPS to derive peak ground displacement (PGD) adjacent to the epicentral area to assess the potential seismic damage.
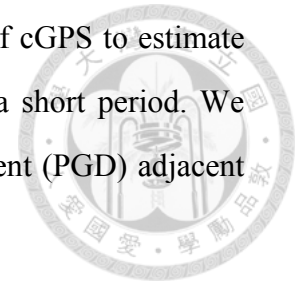
1. 3 SAR Satellite used in this study

The *COSMO-SkyMed* system is a constellation of four radar satellites for Earth Observation founded by the Italian Space Agency and the Italian MoD since 2008. These new sensors provide spatial resolution (between 1x1 and 3x3 m^2) one order of magnitude better than the previous available satellite SAR data, as well as short revisit time of up to 4 days for repeat pass interferometry with the full constellation.

ALOS-2 is the follow-on JAXA L-SAR satellite mission of ALOS launched in 2014. The PALSAR-2 radar is a significant upgrade of the PALSAR radar, allowing higher-resolution (1x3m per pixel) spotlight modes.

Sentinel-1 is the first of the Copernicus Programme satellite constellation conducted by the ESA. The two satellites, Sentinel-1A and Sentinel-1B, carry a C-band SAR instrument which provides a collection of data in all-weather, day or night. The first satellite, Sentinel-1A, launched on 3 April 2014, and Sentinel-1B was launched on 25 April 2016. The repeat cycle is 12 or 6-days with one or two satellite covered.

1. 4 Thesis Roadmap
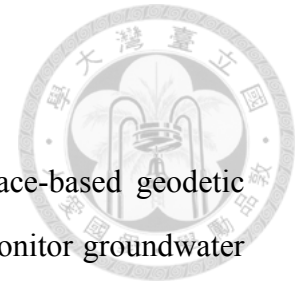
As mentioned before, the aim of this study is applying space-based geodetic observations from GPS and SAR images on the Taipei Basin to monitor groundwater withdraw induced land deformation and coseismic deformation caused by two moderate earthquake occurred in Meinong and Hualien, respectively. Thus Chapter 1 briefly express the scientific backgrounds and goals of this thesis.

The contents of Chapter 2 provide a brief overview of method and software used for processing D-InSAR, PS-InSAR and cGPS in this study. Besides, a fast service research platform TGM is introduced to provide securely archived space-based geodetic data and processed resulted such as velocity field, strain rate, coseismic deformation map for geoscience communities.

The contents in Chapter 3 are mainly composed of the processing of 18 high-resolution X-band SAR images in Taipei metropolitan area to monitor surface deformation induced by groundwater table changes. We present how to calculate the hydraulic parameter of storativity in Jingmei and Wuku Formation based on the correlation of deformation in time series from InSAR and groundwater table height. We also present how to delineate the possible surface trace of the active Shanchiao fault.

In Chapter 4 and Chapter 5, we demonstrate how to apply both GPS and conventional DInSAR observations in coseismic displacements and ground motion behaviors during the Hualien earthquake occurred in northeast Taiwan on Feb. 6, 2018 and Meinong earthquake occurred in southwest Taiwan on Feb. 6, 2016. We also present for how to use high-rate GPS measurements to calculate PGD for assessing the potential seismic damage for providing an alternative or complementary measurements

when earthquake happened.

In Chapter 6, we present the conclusion of the thesis together with the perspective in InSAR and cGPS for future work.

9

Chapter 2

Methodology

2. 1 Interferometry Synthetic Aperture Radar

Interferometric **S**ynthetic **A**perture **R**adar (**InSAR**) technique uses the phase information in two SAR images to determine the phase difference between the two scenes to produce an interferogram used for generating high accuracy DEM (Digital Elevation Model). The first application in earth-based observations of Venus for separating ambiguous echoes from the northern and southern hemispheres was presented by Rogers and Ingalls (1969). Subsequently, the topography of the Moon and Venus were obtained by InSAR technique in 1970s (Zisk, 1972;Rumsey et al., 1974). Until the late 1980s, scientists started using InSAR technique to measure the Earth surface (Zebker and Goldstein, 1986).

10

The most usage Shuttle Radar Topography Mission (SRTM) data was producing a precise global DEM covered about 80 percent of all the land on Earth between 60° north latitude and 54° south latitude during the 11-days in February 2000 by using a single-pass configuration with two radar antennas mounted on a fixed 60 m boom by SAR interferometry technique (Fig. 2-1a). After that, TanDEM-X (**T**erraSAR-X **A**dd-O**n** for **D**igital **E**levation **M**easurement) implemented by a Public-Private Partnership (PPP) between DLR and EADS Astrium launched in 2010 for proposing to generate the worldDEM^{TM} with its twin satellite TerraSAR-X launched in 2007 with a formation flight at distances of a few kilometers down to less than 200 meters. This product can be seen as one of the most consistent, highly accurate and the most complete global DEM data sets of the Earth surface (Fig. 2-1b).
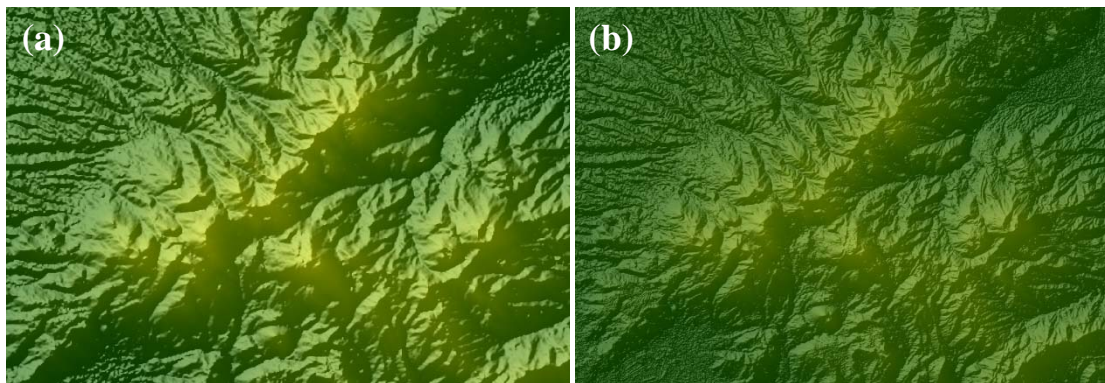
Figure 2-1. Map view of (a) SRTM and (b) TanDEM in Tatun volcano area.

2. 2 Differential Interferometry Synthetic Aperture Radar

The **D**ifferential **In**terferometry **S**ynthetic **A**perture **R**adar (DInSAR) is an extend technique of InSAR and has been applied widely in surface displacement measurements since the first and most famous pioneer work of coseismic displacement pattern on 1992 $M_w7.2$ Landers earthquake published by Massonnet et al. (1993) (Fig.

11

2-2a). The idea is while a target in moving through time, the phase of retuning wave from the target will change and record in different flight (scene). This method basically uses two or more SAR images to generate maps of surface deformation by calculating the retune phase differences. The application of DinSAR technique largely extends to monitor land subsidence, volcanic activity, tectonic activity and ice sheet movement (Fig. 2-1).

In recent years, once a disastrous earthquake occurred, DInSAR technology provide the fastest and comprehensive geospatial information to assess regional seismic hazards immediately after the main shock, such as the 2014 South Napa earthquake in United States (e.g.,(Feng et al., 2015), the 2016 Central Italy earthquake sequence (e.g.,(Cheloni et al., 2017), and the 2017 M_w 7.3 Sarpol Zahab earthquake in Iran (Yang et al., 2018). Furthermore, long-term ground subsidence monitoring (e.g.,(Bawden et al., 2001;Tung and Hu, 2012), volcanic action (e.g., (Amelung et al., 2000;Beauducel et al., 2000;Rivera et al., 2017), tectonic activities, and as well as landslides observations and iceberg movement (e.g.,(Sanchez-Gamez and Navarro, 2017) are also well complement due to accuracy improvement of SAR sensors and DInSAR technique (Fig. 2-2).
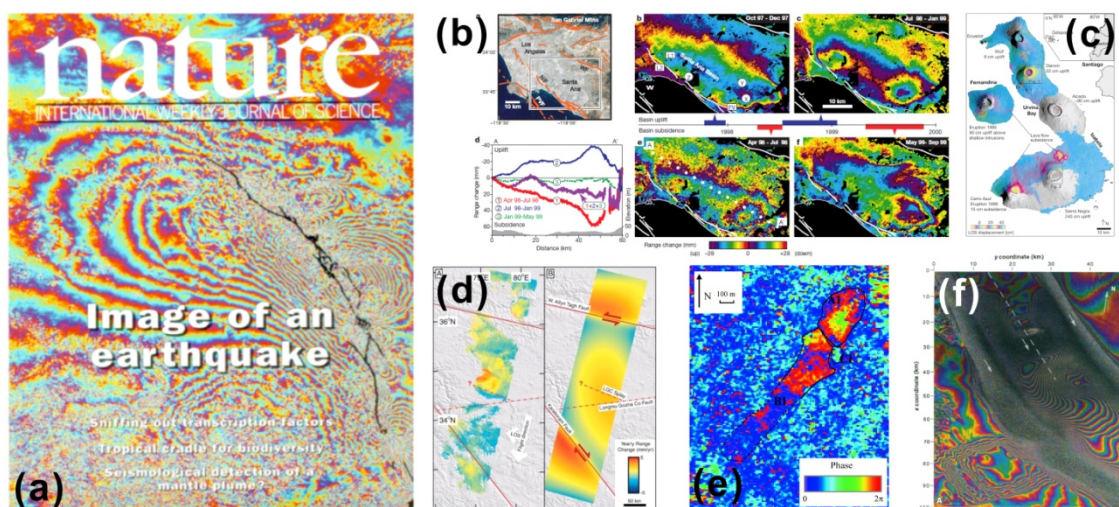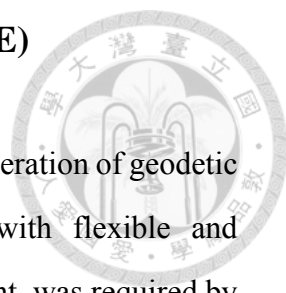
Figure 2-2. Applications of DInSAR: (a) Coseismic deformation of the 1992 Landers

earthquake (Massonnet et al., 1993); (b) Seasonal deformation in the Santa Ana basin (Bawden et al., 2001); (c) Mosaic of two deformation interferograms spanning 1992–7 and 1992–8 at Isabela and Fernandina (Amelung et al., 2000); (d) Observations on the major faults of western Tibet (Wright et al., 2004); (e) One-day geocoded differential SAR interferogram of the La Valette landslide located in the Ubaye valley, southern French Alps (Squarzoni et al., 2003); (f) Radar interferogram of an area that includes a portion of the Rutford Ice Stream (Goldstein et al., 1993).

In Taiwan, Pathier et al. (2003) applied six ERS2-SAR images to determine approximately 30 cm coseismic surface displacement over the footwall of the Chelungpu fault from Taichung city west to the coastline during the 1999 Chichi earthquake occurred. For monitoring in tectonic activity, Huang et al. (2006) monitored an active growing structure with the average uplift rate of ~12.5 mm/yr along the radar line of sight (Hung et al.) in Tainan Tableland by using C-band ERS, Tsukahara and Takada (2018) indicated a quasi-vertical movement of 18 mm/yr and 37 mm/yr at the southern part and north part of Tainan Tableland respectively by using L-band ALOS images and GNSS velocity field. On the other hand, by stacking seven interferograms to reduce the atmospheric phase delay effects, Yen et al. (2008) observed fault activity behavior on the western end of the Meishan Fault, which indicates the Meishan Fault might extend another 10 km to the west of the currently documented location from the historical observations. In monitoring of land subsidence, Hung et al. (2010) first combined leveling, GPS, multi-level compaction monitoring well, and DInSAR data to study the extent of subsidence in Yunlin and its mechanism, showing that the aquifer-system compaction occurs mostly below depths 200 meters, where reduction of groundwater pumping is most needed.

2. 2. 1 InSAR Scientific Computing Environment (ISCE)

InSAR Scientific Computing Environment (ISCE), the new generation of geodetic image processing technology for repeat-pass InSAR sensors with flexible and extensible modular code to encourage modification and improvement, was required by the user community in 2008 (Rosen, 2012). In the middle of 2012, the ISCE package is complete developed by NASA Jet Propulsion Laboratory (JPL) and Stanford University via involving accurate orbit information along with radar motion-compensation techniques to propagate radar echoes from their initial positions to a reference orbit for simplifying the pixel positioning and focusing procedures (Zebker et al., 2010). This software allows users to process a range of available sensors data from the ERS, Envisat, ALOS, COSMO-SkyMed, RADARSAT-1/2, TerraSAR-X, and Sentinel-1 platforms, starting from Level-0 or Level-1 as provided from the data source, and going as far as Level-3 geocoded deformation products using a variety of algorithms. It is also capable of pre-processing products including ISCE, SNAP, GAMMA, and ROI PAC and DORIS. Furthermore, ISCE easily scales to serve as the SAR processing engine at the core of the NASA JPL ARIA (Advanced Rapid Imaging and Analysis) Center for natural hazards as well as a software toolbox for individual scientists working with SAR data, and is planned as the foundational element in processing NISAR data showing its sustainable development.

Two main programs insarApp.py and topsApp.py are used in one differential interferograms generating from a pair of SAR acquisitions. insarApp.py is the most used and maintained application. It is designed to produce stripmap with motion compensated geometry for raw (ENVISAT, ALOS-1, COSMO-SkyMed and zero Doppler data (COSMO-SkyMed SLC stripmap and spotlight, RADARSAT-2, TerraSAR-X stripmap and spotlight, ALOS-2 stripmap); topsApp.py is TOPS (Terrain Observation with Progressive Scan) processor with geometric coregistration for

Sentinel-1 data. All procedures process through xml metadata and python pickle mechanisms. In a xml file, "property" is the ISCE name for an input parameter; "component" is the ISCE name for a collection of input parameters and other components that configure a function to be performed; "catalog" is the ISCE name for a parameter file. Table 2-1 shows full list of Sentinel-1A (S-1A) TOPS processing steps with ISCE and description of the individual steps.

Table 2-1. S-1A TOPS processing with ISCE.

Programs	Description
startup	Initialization of python objects for interferogram processing.
preprocess	Extract raw radar echoes from original sensor files and store them in an ISCE compatible format. Populate metadata fields for use in processing.
computeBaselines	Identifies common bursts between the master and slave products and saves indices.
verifyDEM	Check if the user has provided a DEM. If not download a DEM from the SRTM archive.
topo	Compute pixel-by-pixel lat, lon, hgt, LOS for every pixel in the master product bursts.
subsetoverlaps	Extract burst overlap region outputs for topo into a separate sub-folder.
coarseoffsets	Estimate offset fields to resample slave bursts only for the burst overlap regions.
coarseresamp	Create coregistered Slave SLCs for overlap regions.
overlapifg	Create burst overlap interferograms and take looks.
prepesd	Create cross interferograms for ESD.
esd	Estimate azimuth misregistration using ESD.
rangecoreg	Estimate range misregistration using amplitude correlation of overlap region only.
fineoffsets	Refine slave metadata with range and azimuth misregistration numbers and estimate fine offset fields for full bursts using outputs of topo and refined metadata.
fineresamp	Resample slave bursts using fine offset fields.

15

burstifg	Create burst-by-burst interferograms by cross multiplication.
mergebursts	Merge burst-by-burst products to a stripmap product.
filter	Filter the corrected interferogram using an adaptive filter. Also estimate the coherence for filtered interferogram using the phase standard deviation.
unwrap	Unwrap the interferogram using method of choice.
geocode	Geocode the requested set of outputs.

In April 2014, the first sensor of the Sentinel constellation was launched, spaced-based geodetic observation for Earth Science is going to the next stage. The advantages of Sentinel-1 come from three aspects: Wide range coverage (up to 240 km), high spatial resolution (5 meters in range and 20 meters in azimuth direction) and shorter revisit time (12-days decrease to 6-days with the launch of its twin satellite S-1B since April 2016). Moreover, Sentinel-1 datasets are free to public, which gives the science community more opportunities to explore. Thus, we are processing mass of SAR data from the Sentinel-1 constellation routinely using TOPS processing program "topsApp.py" of ISCE software and generated interferograms of whole Taiwan Island based on the temporal baseline thresholds less than and 30 days to enhance the correlation between SAR image pairs (Fig. 2-3).
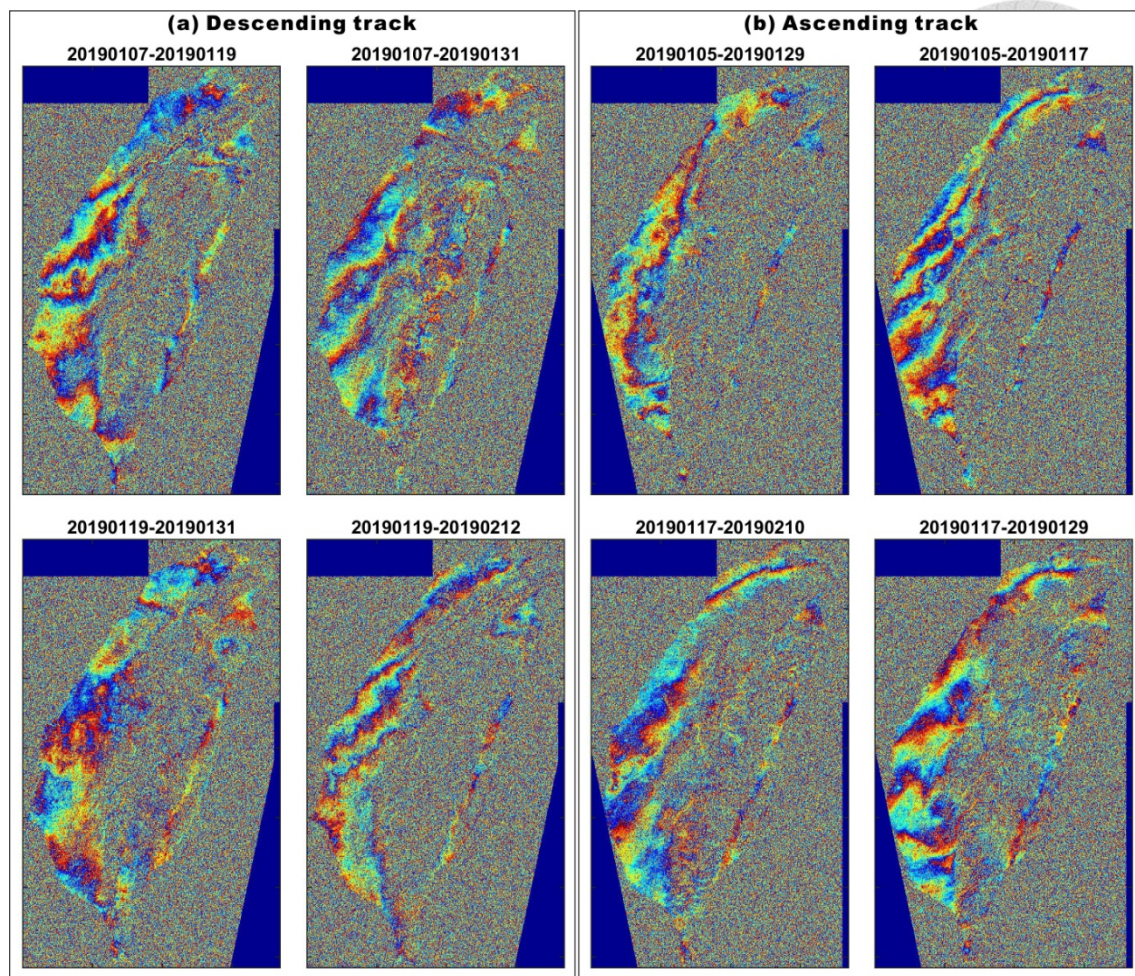
Figure 2-3. Wrapped Sentinel-1 interferograms at the beginning of the 2019 from (a) descending mode of track 105 and (b) ascending mode of track 69. Color bar from blue to red represent phase value change from -π to π.

2. 3 Persistent Scatterers InSAR

The Persistent Scatterers InSAR (PSInSAR) has been brought up in 1999 by Ferretti et al. (2000);(2001) of the Technical University of Milan (POLIMI), and is an advanced technique in comparison with conventional InSAR technique. This technique addresses to overcome the problems of decorrelation for generating a time series of

17

phase changes by computing only on special scatterers, such as buildings, bridges, dams, large rock outcrops, and other prominent natural features. These time–coherent pixels, i.e., persistent scatterers , are stable or strong enough to be precisely tracked for over a long time and as a dominator of the information in the whole area to reduce the uncertain signal of back scatters (Fig. 2-4).
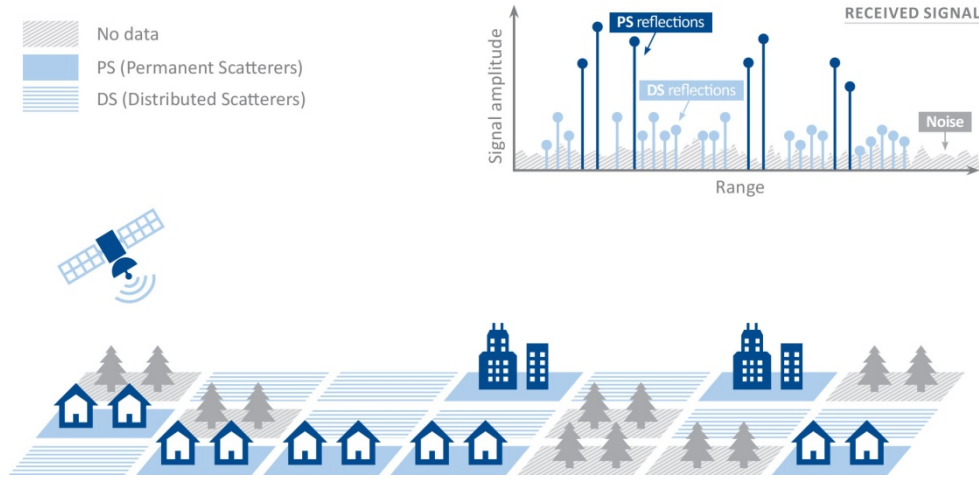
Figure 2-4. Illustration of Persistent Scatterer InSAR (TRE ALTAMIRA, 2019).

The PSInSAR technique is an innovation of conventional DInSAR technique, which processing multi-SAR images (N+1) to form N interferograms with respect to the same master scene. In each differential interferogram, the pixel (ϕ_{int}) phase can be represented as the sum of 5 terms (Hooper et al., 2004),

$$\phi_{int} = \phi_{def} + \Delta\phi_{\varepsilon} + \Delta\phi_{orb} + \phi_{atm} + \phi_{noise}$$

where ϕ_{def} represents the phase change due to movement of the pixel in the range distance, ϕ_{ε} refers to the residual topographic phase due to misfit with the DEM, ϕ_{orb} refers to the error introduced due to the usage of imprecise orbits, ϕ_{atm} corresponds to the phase due to different atmospheric condition between passes, and ϕ_{noise} represents the phase noise term due to temporal and spatial decorrelation, thermal noise and coregistration errors. By considering the ϕ_{def}, ϕ_{atm} and ϕ_{orb} are spatially correlated

18

in a particular distance (1 km) but decorrelation in time domain, and ϕ_ε is proportional to the perpendicular baseline. The important terms can be isolated taking advantage of their different frequency characteristics in space and time.
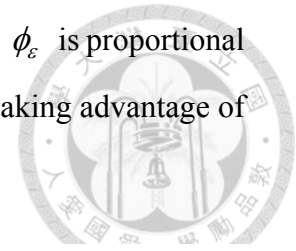
Currently, PSInSAR technique has used for a range of applications, including landslides rate of 3 mm/yr in LOS direction with accuracy of 1 mm/yr in Ancona area, Italy (Ferretti et al., 2001); surface subsidence of 20 cm/yr and uplift of 6 cm/yr in six years in Pononad, United States, by using 40 ERS interferograms (Ferretti et al., 2000); tectonic movement of active San Andreas strike slip fault observation in San Francisco Bay area by using 49 ERS SAR acquisitions between 1992 and 2000 (Ferretti et al., 2004); man-made construction deformation of water level change in Plover Cove Dam of Hong Kong with 62 TerraSAR-X and 11 TanDEM-X images acquired between October 2008 and June 2012 represented maximum displacement of 16 mm in LOS direction (Matus Bakon et al., 2014), and temporal and spatial pattern of deformation of Long Valley Volcanic Caldera in eastern California with 22 ERS SAR images where conventional interferograms showed almost complete decorrelation (Hooper et al., 2004).

In 2010, Chang et al. (2010) investigated active faults behaviors of the northern Taiwan with fifteen years SAR images by using PSInSAR technique and has proven its capability of measuring ground deformation in mountain area of Taiwan (Fig. 2-5a). Furthermore, Peyret et al. (2011) and Champenois et al. (2012) presented PS mean velocity maps all along the Longitudinal Valley in eastern Taiwan showing a clear velocity discontinuity localized in a narrow band (0.1–1 km) and shallow interseismic creep behavior of up to 3 cm/yr velocity offset along the LOS direction with C-band ERS and L-band ALOS images, respectively (Fig. 2-5e). Besides tectonic activity, Tung et al. (2016) revealed dramatic change from serve subsidence to uplift in surface deformation due to ground water level variation in two years period from 2011 to 2013

in Taipei Basin with 18 high resolution X-band COSMO-SkyMed SAR images (Fig. 2-5b). Besides, similar land subsidence rate of up to 10 cm/yr between 1996 to 1999 and slowed down gradually from 2005 to 2008 due to artificial water pumping in Choushui River Fluvial Plain of the western central Taiwan also have been published by Tung and Hu (2012) and Lu et al. (2015) (Fig. 2-5c and 2-5d).
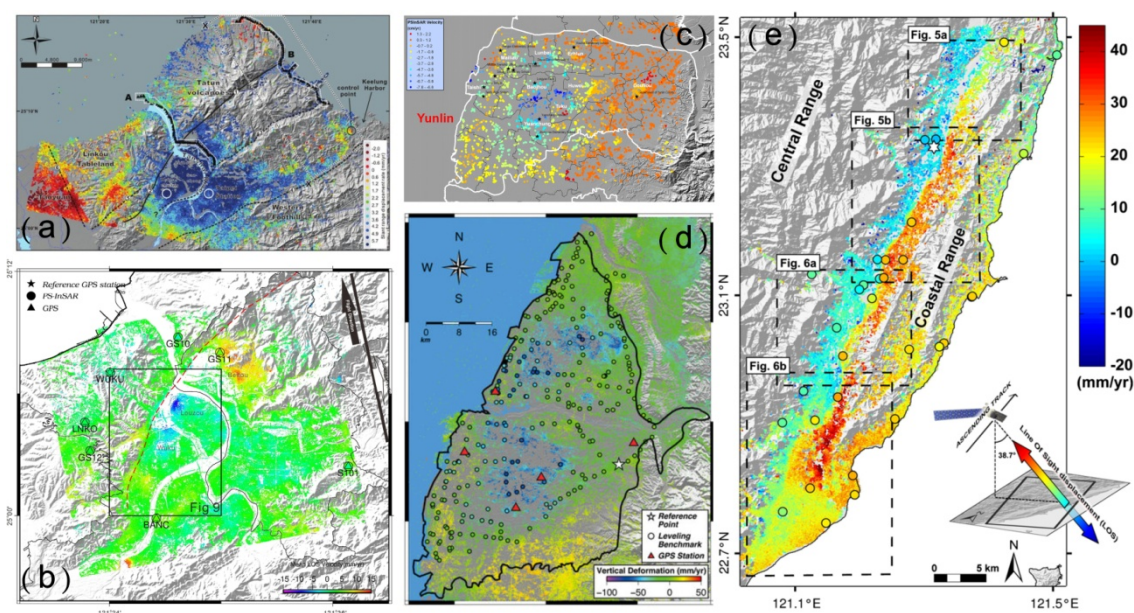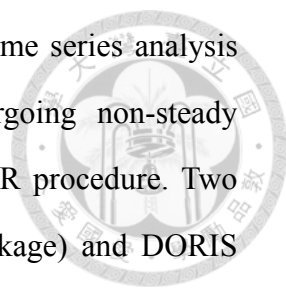
Figure 2-5. Applications of PSInSAR for surface deformation in Taiwan : (a) Slant range displacement rate of the processed PSs in northern Taiwan area (Chang et al., 2010); (b) Slant range displacement rate of PS points in the Taipei Basin (Tung et al., 2016); (c) Average rate of along LOS of PS points in Yunlin area (Tung and Hu, 2012); (d) Vertical deformation of precise leveling and PSI in central Taiwan between 2005 and 2008 (Lu et al., 2015); (e) Map of PS mean LOS velocities on the southern part of Longitudinal Valley between January 2007 and February 2010 derived from PALSAR dataset (Champenois et al., 2012).

2. 3. 1 Stanford Method for Persistent Scatterers (StaMPS)

Stanford Method for Persistent Scatterers / Multi-Temporal InSAR (StaMPS /

20

MTI) is the most common and mature software package for PS time series analysis even in terrains devoid of man-made structures and/or undergoing non-steady deformation (Hooper et al., 2012). Before processing the PSInSAR procedure. Two open source software ROI-PAC (Repeat Orbit Interferogram Package) and DORIS (Doppler Orbitography and Radiopositioning Integrated by Satellites) will be used for producing SLC image from RAW data and then generating interferogram. The algorithm of PSInSAR is established on tracking PS points movements in time series. Thus, the selections of PS points are quite important. In StaMPS technique, the *Amplitude Dispersion Index* $\left(D_A\right)$ and *spatial coherence* methods were both used for PS candidates selection. After error estimation, three-dimensional phase unwrapping, low-pass filter in space than high-pass filter in time were applied for eliminating atmospheric effects and noises to get surface deformation.

Since 2013, we processed ERS1/2, Envisat and ALOS SAR images to analyze surface deformation in whole Taiwan by using StaMPS software. Moreover, we combine PSInSAR result, precise leveling data and GPS measurements to evaluate the deformation behavior and velocity of 33 active faults in Taiwan (Fig 2-6). However, due to the lifetime termination of satellite and limitation of SAR image size, long term surface deformation with island scaled is not easy to achieve from fragment scenes. For the purpose of continuous ground displacements at the scale of the whole Taiwan Island performing, new generation of wide scene ScanSAR image of open access Sentinel-1 images processing via ISCE software package will be used in the future (Fig. 2-7).

21
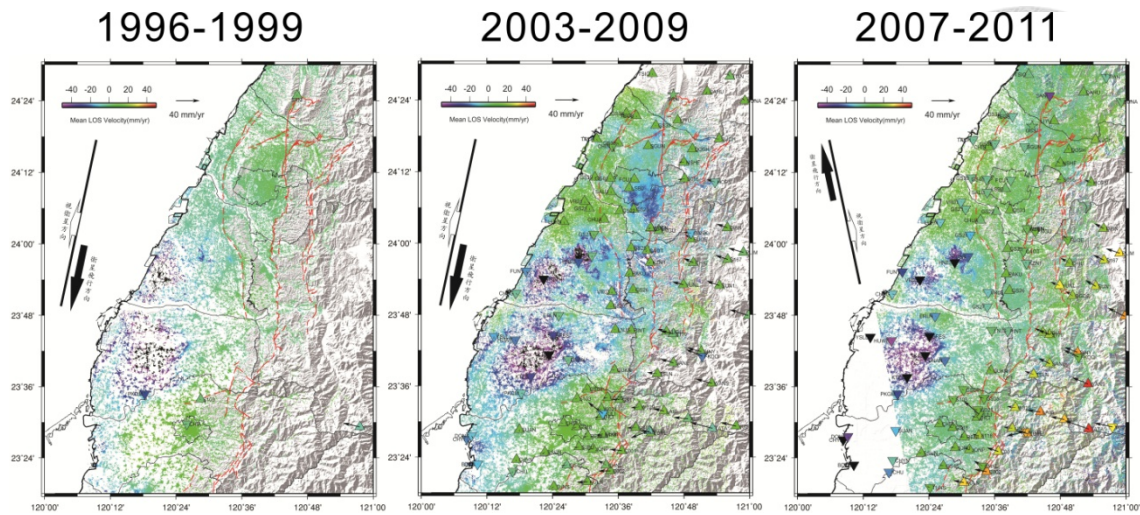
Figure 2-6. Slant range displacement rate in different time periods of ERS, Envisat and ALOS images in western Taiwan overlapped on the hill-shaded background. Shortening in slant range (rate in positive with warm colors) represents land uplift and elongation (rate in negative with cold colors) represents land subsidence in slant range direction.

22
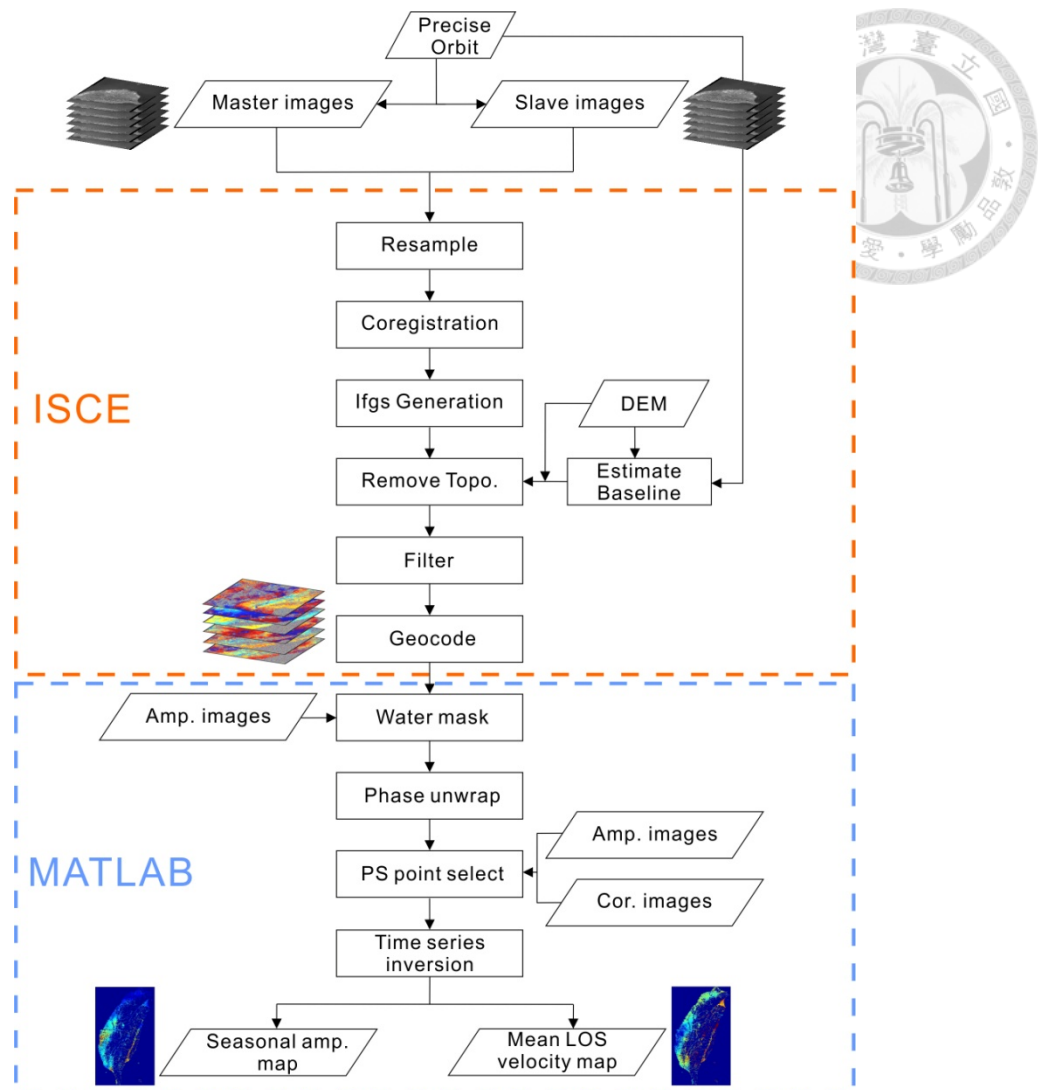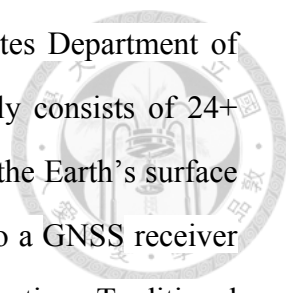
Figure 2-7. Workflow of PSInSAR processing.

2. 4 GNSS Precise Point Positioning

The **G**lobal Navigation Satellite System (GNSS) refers to a constellation of global satellite-based navigation and positioning system from space that transmit positioning and timing data to GNSS receivers. Examples of GNSS include Europe's Galileo, Russia's Global'naya Navigatsionnaya Sputnikovaya Sistema (GLONASS) and China's BeiDou Navigation Satellite System. Besides, the USA's

NAVSTAR Global Positioning System owned by the United States Department of Defense (DoD) is a global navigation satellite system that nominally consists of 24+ satellites orbiting at an altitude of approximately 20,200 km above the Earth's surface provides geolocation and time information by microwave signals to a GNSS receiver anywhere on the Earth rely on four to ten GNSS satellites at the same time. Traditional GNSS relative positioning is the most accurate and commonly technique in geodetic surveying. This technique uses simultaneous observations from two or more receivers of which at least one of them with known coordinates. The positions of the rest stations can be determined by using differenced carrier phase observations with regard to the concept of baseline or network estimation.

Zumberge et al. (1997) first introduced a positioning technique called **P**recise **p**oint **p**ositioning (PPP) in which un-differenced observations at only a single receiver is processed to determine coordinates when precise satellite orbits and clocks are provided (Fig. 2-8). This technique improved efficiency and has been proved at the centimeter and subdecimeter level positioning accuracy in measuring static and moving receiver, respectively (Zumberge et al., 1997;Kouba and Héroux, 2001). Moreover, this technique can avoid spurious effects due to the motion of the reference station(s) required in traditional GNSS relative positioning approach, in case these stations are affected by the same motion, such as earthquake. Several software packages capable of PPP processing have been developed, including the GIPSY-OASIS (GOA II, GNSS-Inferred Positioning System and Orbit Analysis Simulation Software) developed at the JPL, the Bernese GPS (BSW) developed at the Astronomical Institute at the University of Bern (AIUB), and the P3 developed at the University of Calgary.
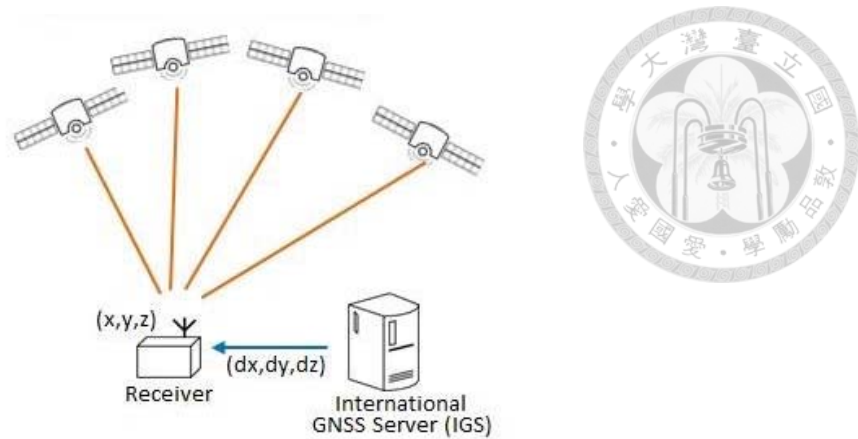
Figure 2-8. Precise point positioning (PPP).

Recent years, the PPP technique has been widely used in crustal deformation monitoring (Azua et al., 2002;Savage et al., 2004;D'Agostino et al., 2005;Hammond and Thatcher, 2005;Calais et al., 2006). In Taiwan, PPP technique has applied in estimating the zenith tropospheric delay (ZTD) proving GPS as an alternative meteorological sensor (Chiang et al., 2009). Sea level variation observed by GPS buoys in Anping, Tainan showing the potential to measure the sea surface variations with cm-level accuracy (Kuo et al., 2012). Also ground motion caused by moderate magnitude Rusesuei earthquake occurred in 2013 as well as presented by Hung et al. (2017).

2. 4. 1 GIPSY-OASIS

The GIPSY-OASIS package (GNSS-Inferred Positioning System and Orbit Analysis Simulation Software) is developed by the Caltech Jet Propulsion Laboratory (JPL), and maintained by the Near Earth Tracking Applications and Systems groups (Web F.H. and Zumberge J.F., 1995). The GIPSY-OASIS II (GOA II) package consist of extremely versatile software that can be used for GNSS positioning and satellite orbit analysis. It can provide centimeter-level GNSS positioning accuracy over short to intercontinental baselines by estimating position solutions from modeling most of the

terms in the GNSS observation such as tides, ocean loading, crustal plate motion and tropospheric delay to minimize the misfit between observations and models.

The main programs "gd2p.pl" (GNSS data 2 Position, Fig. 2-9) is the preferred black box for both static point positioning and kinematic point positioning for a single receiver. After checking the correctness of the following metadata including receiver types, antenna types and radomes and eccentricities of the antenna reference point (ARP) with respect to a station mark, the precise final, non-fiducial daily products of orbit positions and clock offset from JPL archive were used to reduce satellite orbit and clock offsets in the data procedures. Besides, Vienna Mapping Function (VMF1) and antenna calibration provided from NOAA's National Geodetic Survey were used to reduce atmosphere delay and phase center modeling. On the other hand, ocean tide effects were reduced according to FES2004 ocean loading model. Finally, GIPSY post-processing program "stacov2env" were executed to generate ascii East North Up (ENV) time series file for individual sites with multiple flavors of time stamps.
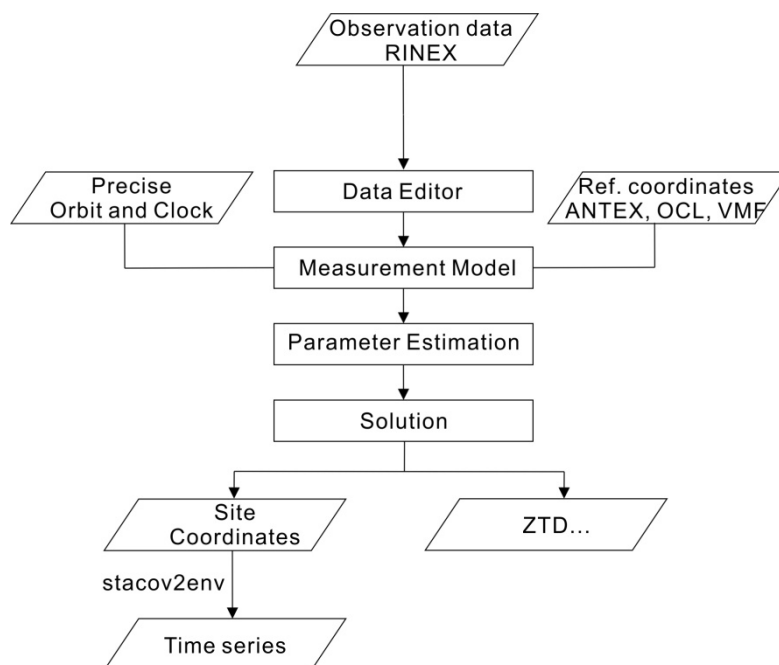
Figure 2-9. Typical GIPSY workflow for GNSS positioning using program gd2p.

2. 5 Taiwan Geodetic Model

Taiwan Geodetic Model, TGM (Fig. 2-10) is a research platform to offer a fast service for earth sciences research gathered by IES, Academia Sinica. This platform is a distributed federation of datacenters established to securely archive space-based geodetic data and metadata, providing access to continuous GNSS station data and extended products such as velocities, strain rate and coseismic deformation map for the geosciences research communities. Furthermore, once an earthquake with M > 6.0 occurred inland, the geodetic observations of coseismic displacements from GNSS stations and SAR images will be represented and downloadable in few days after the earthquake for further investigations. Here we show an example for providing coseismic deformation map with available GPS and SAR data after 2018 Mw 6.4 Hualien earthquake (Fig. 2-11).
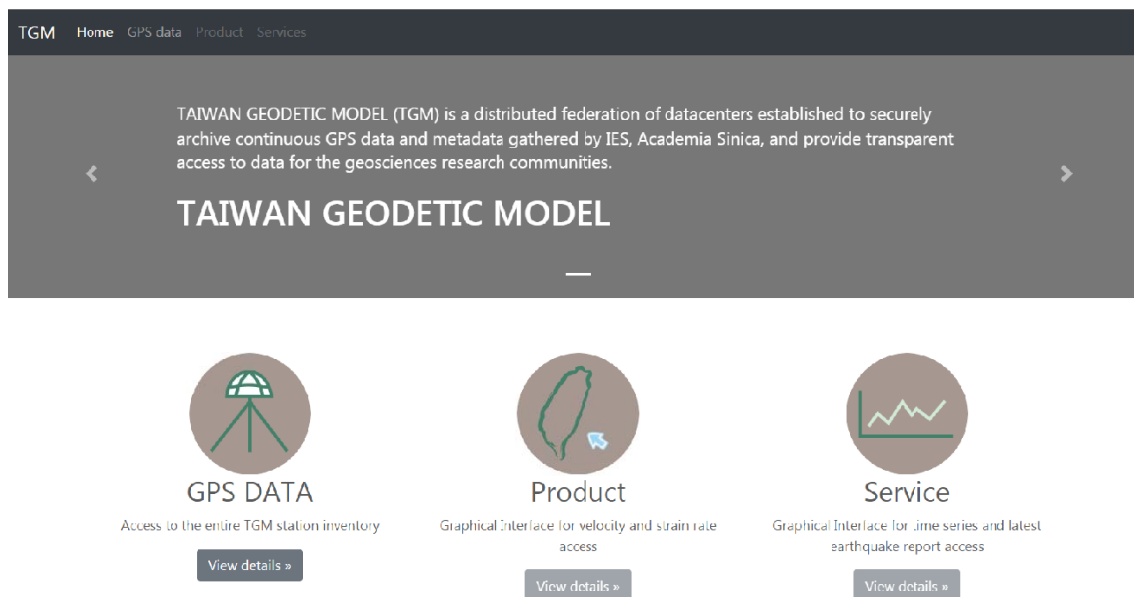
Figure 2-10. The platform homepage of Taiwan Geodetic Model, TGM (http://gdbweb.earth.sinica.edu.tw/TGM/index.php).

27
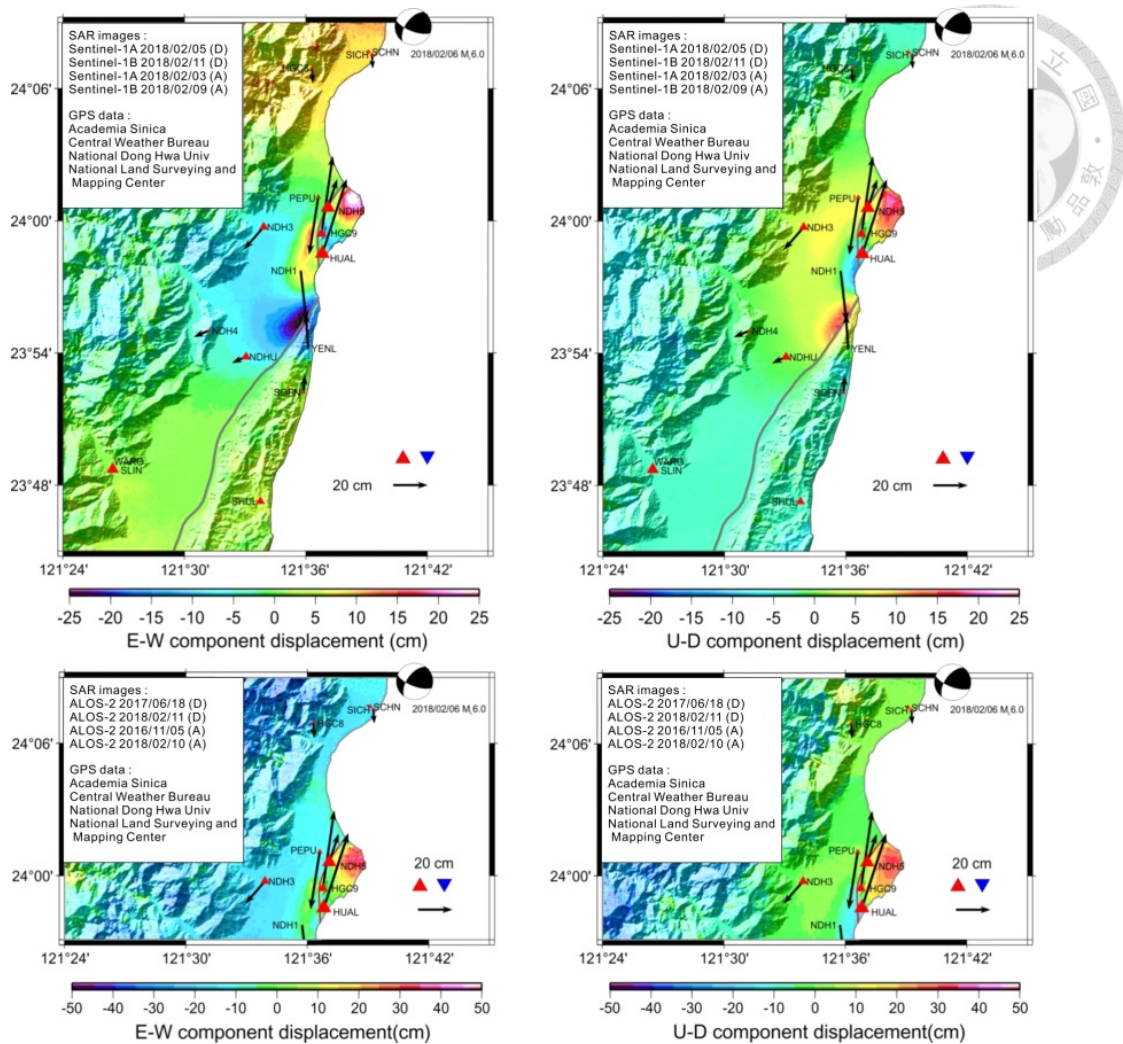
Figure 2-11. 2.5 dimension (quasi-3D) coseismic deformation across the main deformation area observed after 2018 Mw 6.4 Hualien earthquake. Warm color represents eastward surface rupture and uplift; cool color represents westward movement and blue color represents subsidence. Black arrows represent the GPS horizontal displacements and solid triangles indicate the vertical movements of GNSS stations.

In Taiwan, island-wide GNSS network contain more than 450 continuous GNSS station was established and exchange data every month from several agencies including the Institute of Earth Sciences, Academia Sinica (IESAS), Central Weather Bureau (CWB), Central Geological Survey (CGS), Ministry of Interior (MOI), Water

28

Resources Agency (WRA) and other universities since 1991. By setting up this automatic GPS processing system, the correct coordinates of more than 450 continuous GNSS stations in whole Taiwan could be produced automatically with an optimal strategy daily by using GIPSY software (Fig 2-12). Also, time series file for individual sites will be generated after removing outliers and jumps due to station relocation. The each component of the GPS time series were defined to equation (2-1) using the least-square method as modified from Nikolaidis et al. (2001) :

$$y(t_i) = a + bt_i + c\cos(2\pi t_i) + d\sin(2\pi t_i) + e\cos(4\pi t_i) + f\sin(4\pi t_i)$$
$$+ \sum_{j=1}^{n_g} g_j \cdot H(t_i - T_{gj}) + \sum_{j=1}^{n_k} k_j \cdot H(t_i - T_{kj}) \cdot e^{-\frac{t_i - T_{kj}}{\tau_j}} + v_i \qquad (2-1)$$

where N are the daily solution epochs in units of years and the first term involves the site position a at the first epoch and the linear rate b during inter-seismic period; c and d describe the amplitude of annual and semi-annual motions; The fourth term corrects for any number (n_g) of offsets (including coseismic displacements and antenna changes) with magnitudes g_j at epochs T_{gj}; The post-seismic represent as exponential decay with magnitude, k_j, at the selected earthquake epochs T_{kj}; the last term is measurement error v_i. Moreover, H is the Heaviside step function and τis relaxation time (Fig. 2-13).

29
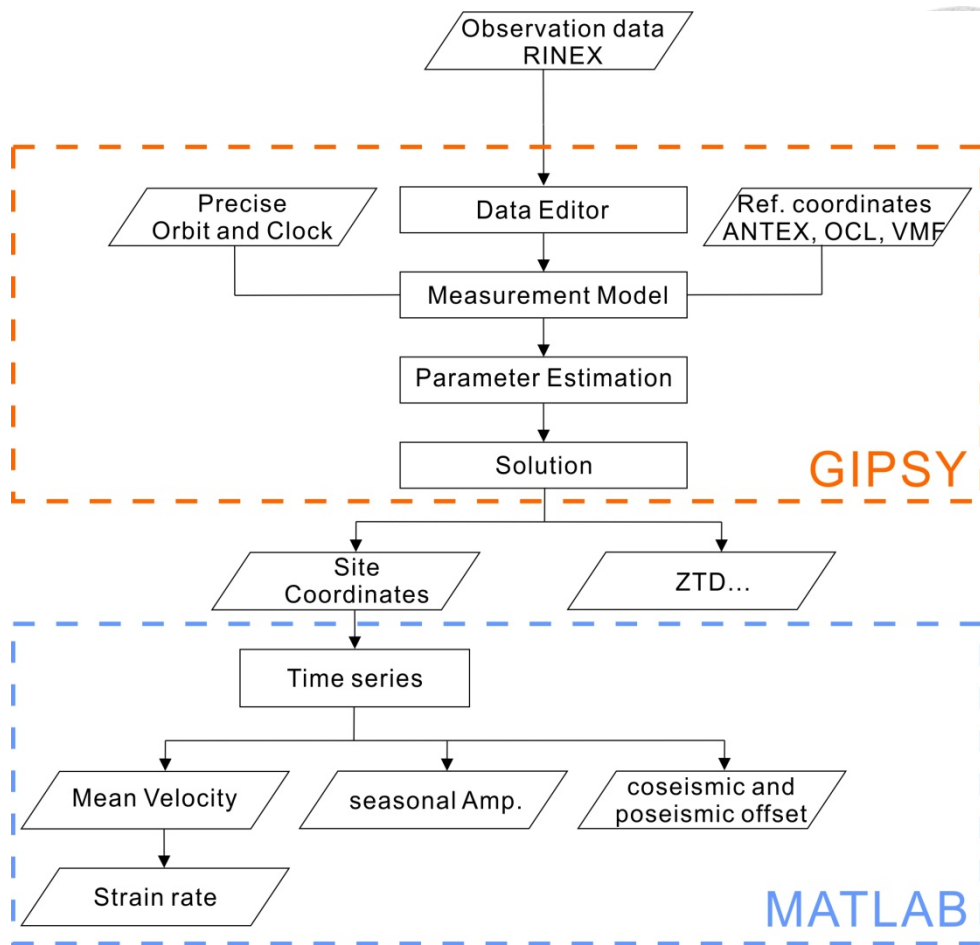
Figure 2-12. Automatic GPS processing workflow.
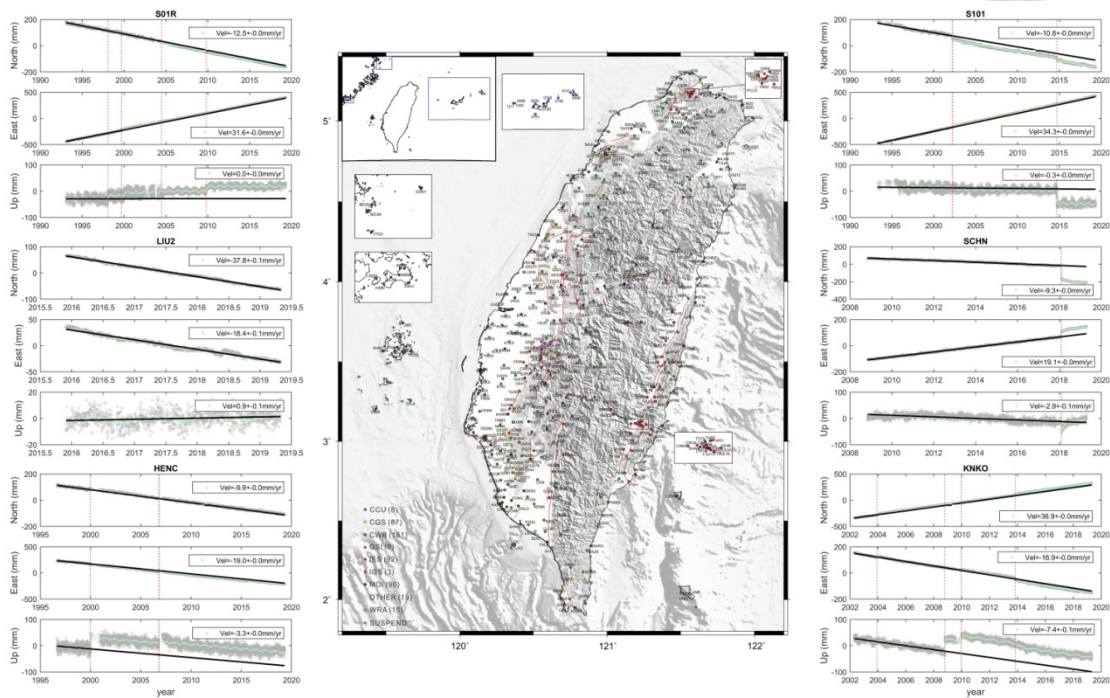
Figure 2-13. GPS position time series of the continuous GPS stations S01R, LIU2, HENC, S101, SCHN and KNKO in the north, east and up components, respectively. The grey circles are initial solutions and red lines represent timings of offsets (including coseismic displacements and antenna changes antenna change).

After removing coseismic offsets, post-seismic effects, periodic motion and noise outliers with equation (2-1), the statistics analysis and time series of stations with continuous data more than one year will be released monthly. Moreover, users can set the specific time periods for time series plots and velocity calculations. Inspecting relative velocity field and relative time series are also available by appointing any reference GPS station. For crustal deformation analysis, after inspecting in detail, the yearly velocity field and overall strain in Taiwan will be published online routinely from both continuous GPS (Fig. 2-14) and Sentinel-1 differential SAR result (Fig 2-15).

31
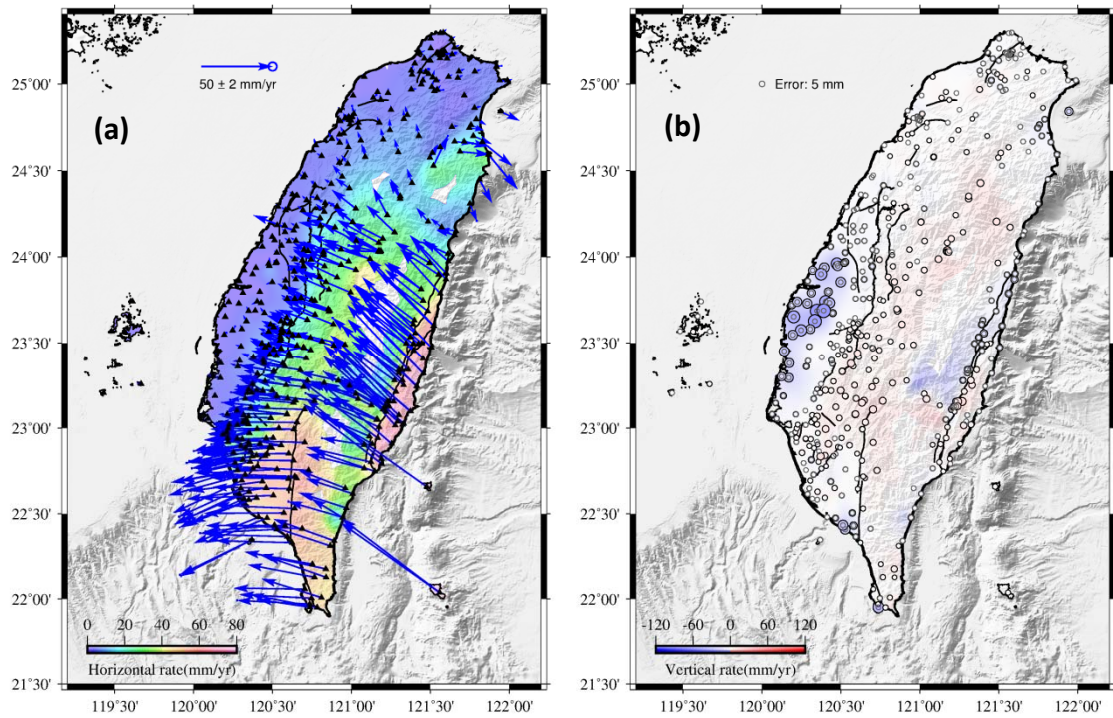
Figure 2-14. GPS (a) horizontal and (b) vertical velocities field of Taiwan with respect to station S01R since 1992.
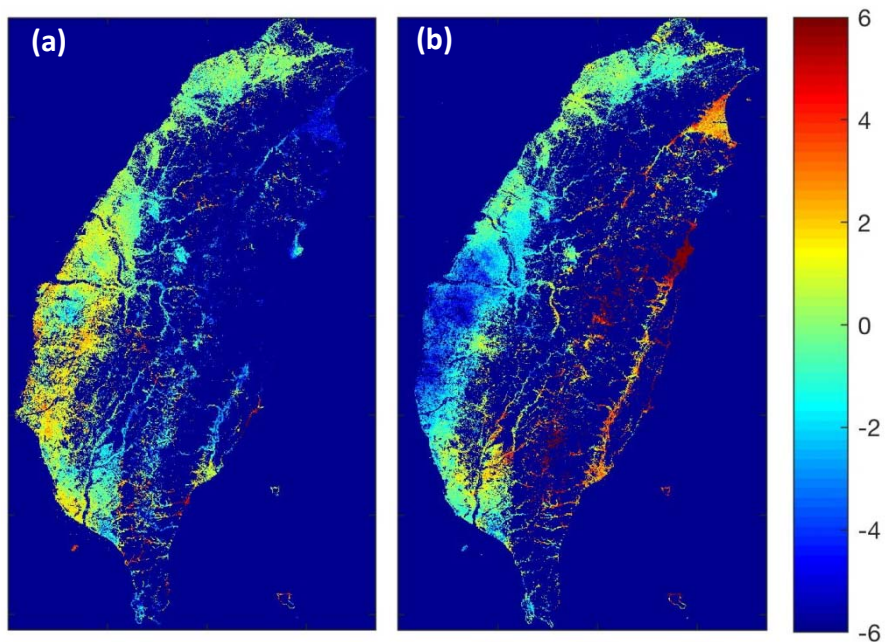
Figure 2-15. LOS velocities field from (a) Sentinel-1 descending mode of track 105 and (b) ascending mode of track 69. Color bar from blue to red represent velocity change from -6 to 6 cm/yr since 2015.

32

Chapter 3

Transient deformation induced by groundwater change in Taipei metropolitan area revealed by high resolution X-bandSAR interferometry

This chapter has been originally published in Tectonophysics as the following citation. Please see the whole content in Appendix I.

Tung, H., Chen, H.-Y., Hu, J.-C., Chen, H., Yang, K.-H. and Ching, K.-E., 2016. Short-term fluctuation of surface deformation in Taipei metropolitan area revealed by high resolution X-band SAR interferometry. *Tectonophysics*, 692, 265-277, doi: 10.1016/j.tecto.2016.03.030.

Located at the northern part of Taiwan, Taipei is the most densely populated city and the center of politic, economic, and culture of this island. North of the Taipei basin, the active Tatun volcano group with the eruptive potential to devastate the entire Taipei is only 15 km away from the capital Taipei. Furthermore, there are several active faults lie in and around the Taipei basin. Therefore, it is not only an interesting scientific topic but also a strong social impact to better understanding of the geological hazard processes and hazard mitigation in the metropolitan Taipei city.

Chen et al. (2007) proposed that the variations in subsidence and the recovery of surface deformation within the Taipei Basin can be divided into three major periods: (1) 1975-1989: land subsidence mainly ascribed to the compaction of the water-depleted aquifers gradually decreased after the government put a stop on the use of groundwater during the early 1970s; (2) 1989-2000: land subsidence switched to slight uplift throughout a large part of the basin caused by elastic rebound of the aquifers; and (3) after 2000: surface deformation decrease with no significant subsidence or uplift in 2003 from the leveling data of 406 benchmarks (Fig. 3-1). He also declaimed land subsidence come from surface soil compaction and tectonic load from the Shanchiao Fault are about 2-3.5 mm/yr and 0.9-1.75 mm/yr, respectively. Thus, the intermediate component of the impact of the aquifer deformation change is main mechanism to control the land elevation change (Fig. 3-2). On the other hand, Chang et al. (2010) suggested that the significant subsidence occurred at the border of the Taipei Basin and a relatively slight uplift rebound in the central basin, and displacements along the Shanchiao, Chinshan, and Kanchiao Faults are large enough to be observed. After that, Huang et al. (2016) also suggested that part of surface deformation from SAR interferometry should be related to the groundwater recharge and withdrawal.

34
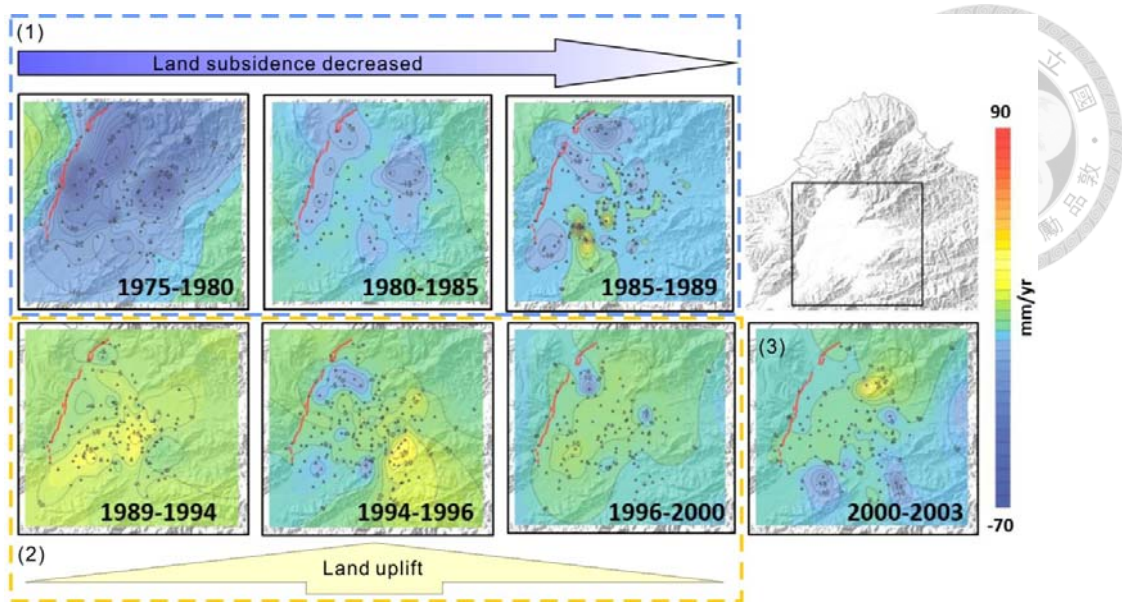
Figure 3-1. Contour maps of the surface deformation in the Taipei basin from 1975 to 2003. Contour interval is 5 mm/yr (modify from Chen et al. 2007).
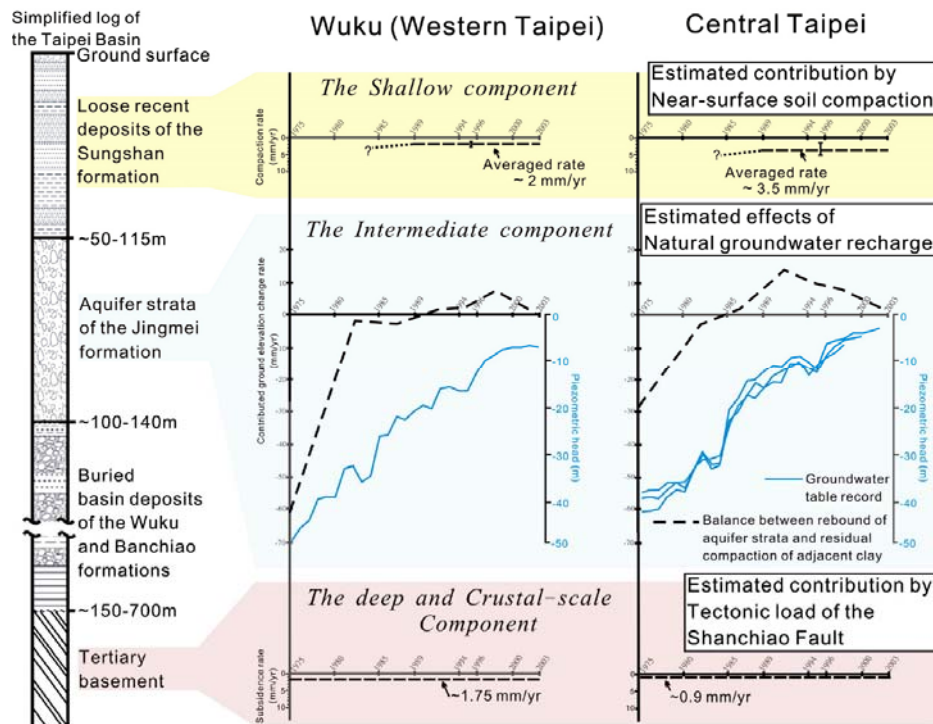
Figure 3-2. Mechanisms of three depth-related component responsible for land elevation change in the Taipei Basin (Chen et al., 2007)

In this study, we use 18 high resolution X-band SAR images from the new

35

generation COSMO-SkyMed (CSK) constellation for associating with leveling and GPS data to monitor surface deformation in Taipei area. The higher resolution of stripmap mode of CSK SAR images (3m x 3m) m, which is one order of magnitude better than the previous available satellite SAR data, lead to an increase of the density of the measurable targets relative to those retrieved from medium resolution datasets (C- and L-band). Besides, the more frequent revisit of the same area provides massive datasets to avoid the baseline limitation and diminish temporal decorrelation. According to these advantages, a delicate deformation velocity map has been performed. The most land subsidence area (cold colors) is located in Luzou and Wukou area in the whole dataset from Sep 2011 to July 2013 (Fig. 3-3).
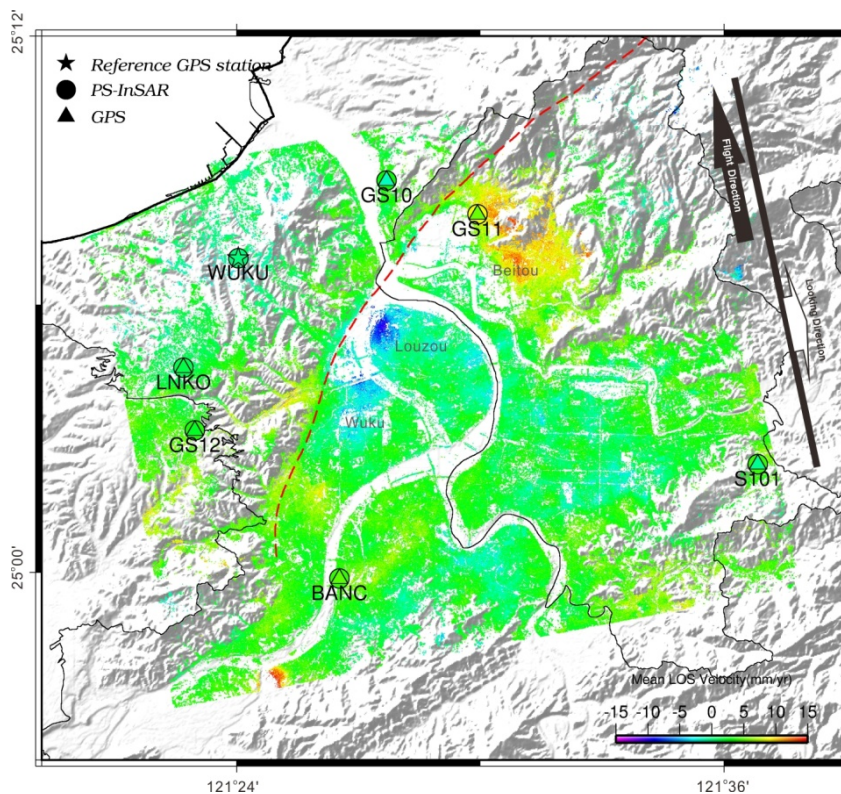
Figure 3-3. LOS velocity in the Taipei Basin overlapped on the hill-shaded background. Red dashed lines mark the active Shanchiao Fault. Colored triangles represent transferred GPS velocity to LOS direction and colored circles represent average velocities of PS points within 100 meters of the GPS station.

36

Surprisingly, whenever the whole dataset was separated into two sub-datasets to fit the survey period of precise leveling from I. 2011/9–2012/9 and II. 2012/9–2013/7, significant opposite surface deformation behaviors revealed in the Taipei basin was observed. In the Taipei basin, the variation of LOS rate can reach to 10 cm/yr (-5 cm/yr in period I and 5 cm/yr in period II). The PSInSAR result shows good agreement with continuous GPS and independent precise leveling survey data (Fig. 3-4). The correlation between the PSInSAR-derived deformation with groundwater level in the buffer intervals indicate the elevation change in the Taipei Basin in these two period was caused by pumping behavior for construction of Airport MRT Taipei Station (Fig. 3-5, Wu, 2017).
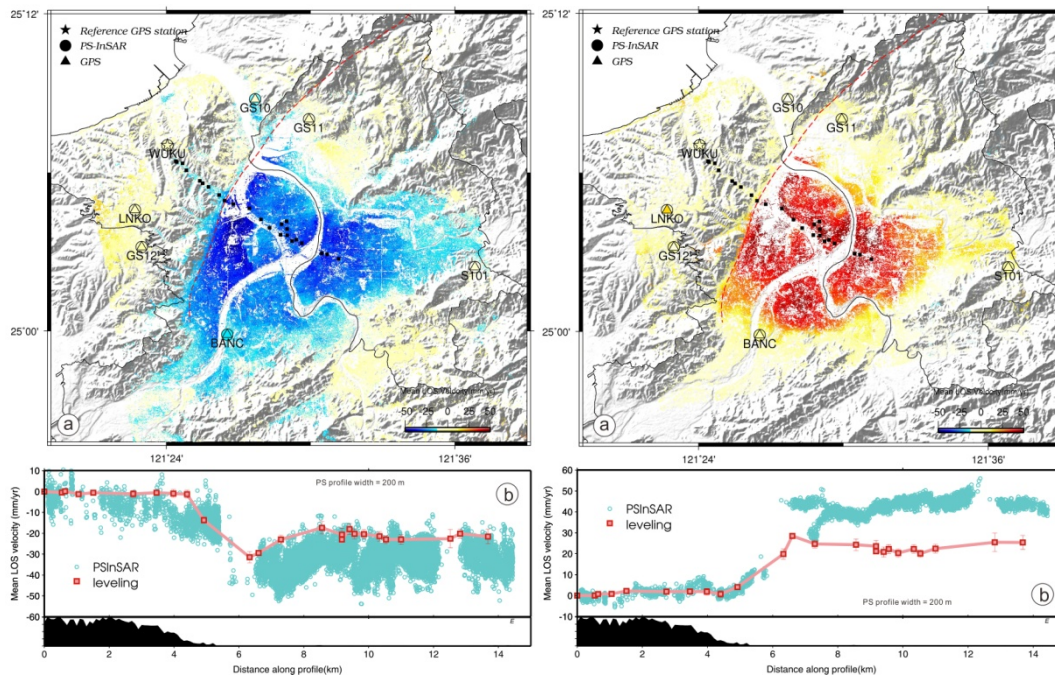
Figure 3-4. (a) Slant range displacement rate of time span 2011/9–2012/9 and 2012/9–2013/7. Black rectangles are the locations of benchmarks in leveling route. (b) Comparison between the leveling data and PSInSAR result along the central of the Taipei Basin.

37
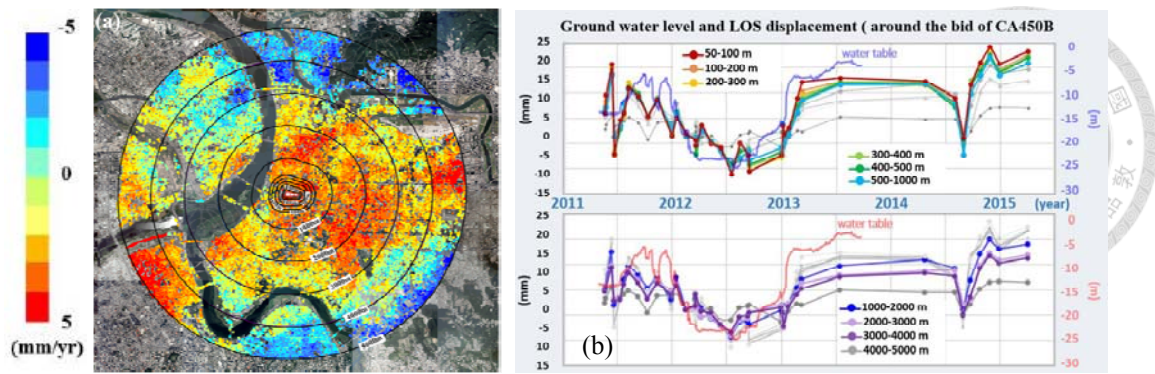
Figure 3-5. (a) Distribution of PSInSAR deformation in the buffer intervals. (b) Time series of LOS deformation during the bids of CA450B pumping.

We also characterize the storativity by using the correlation of surface deformation from time series of PSInSAR and groundwater level change within the metropolitan Taipei City. The storativity is roughly constant with values between 0.5×10^{-4} and 1.6×10^{-3} in Jingmei Formation, which is in good agreement with values from water pumping test in Jingmei Formation. Also, the storativity-simulated groundwater level show similar time series with the observed groundwater level data at the groundwater wells (Lee et al., 2018). The reliability of PSInSAR-derived deformation provides us a regional groundwater level map which conquer the limitation from sparse locations of groundwater wells (Fig. 3-6, Lin, 2018).
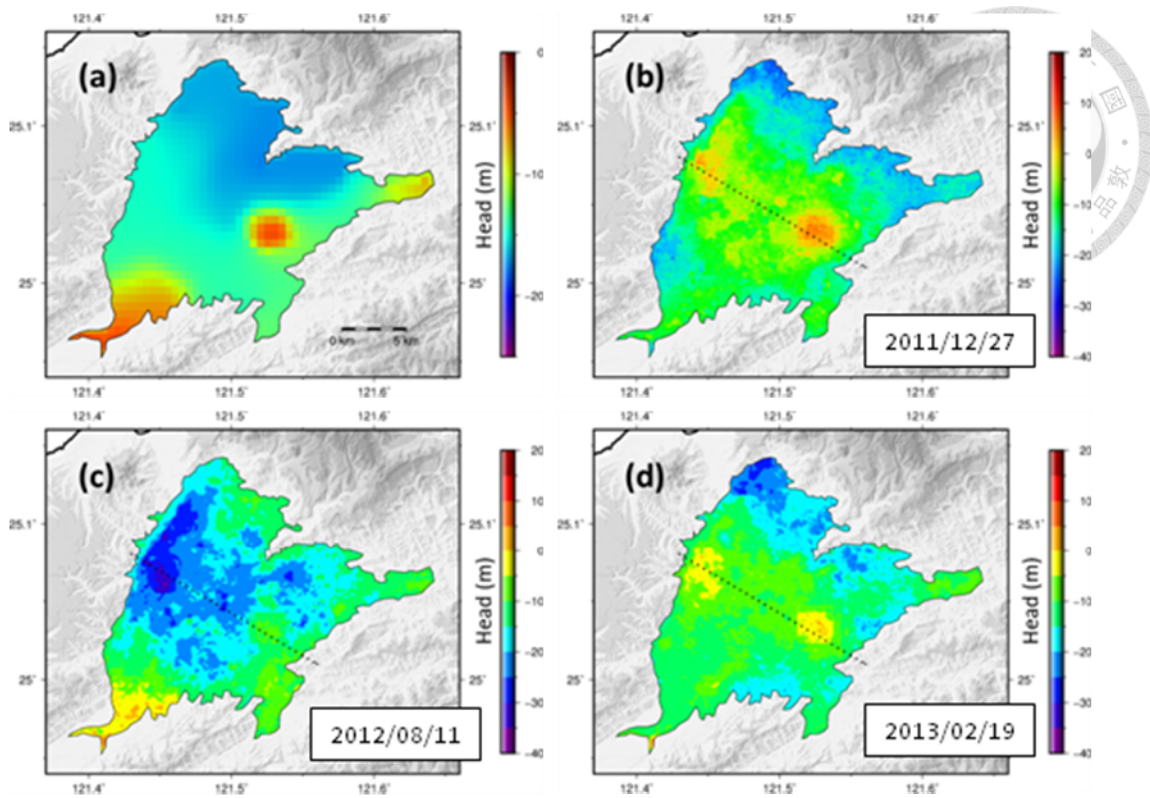
Figure 3-6. Simulated groundwater level map (a) in March 2012, (b) on 2011/12/27, (c) 2012/8/11 and (d) 2013/2/19 (Lee et al., 2018).

According to cross-correlation and correlation coefficient calculation from the groundwater level observation wells by Chang (2015) and Wu (2017), there is almost no time delay effect between PSInSAR-derived deformation and groundwater level change. Approximate seventy percent of total pieces of data show positive correlation. Moreover, strong to very strong positive correlation value (> 0.6) could be observed in the confined aquifer in the central Taipei Basin (Fig. 3-7, Lin, 2018). It seen that the relationship between surface deformation and groundwater level is mainly dominated by Jingmei formation. The estimated storativity indicated that one meter groundwater level change induce about 9 and 16 millimeter surface deformation change in Luzou and Wukou area respectively, which is about eight times faster the long-term tectonic deformation rate in this area. Thus, to access the activity of the Shanchiao Fault, it is important to discriminate tectonic movement from anthropogenic or seasonal effect in

39

the Taipei Basin to better understand the geohazards and mitigation in the Taipei metropolitan area.
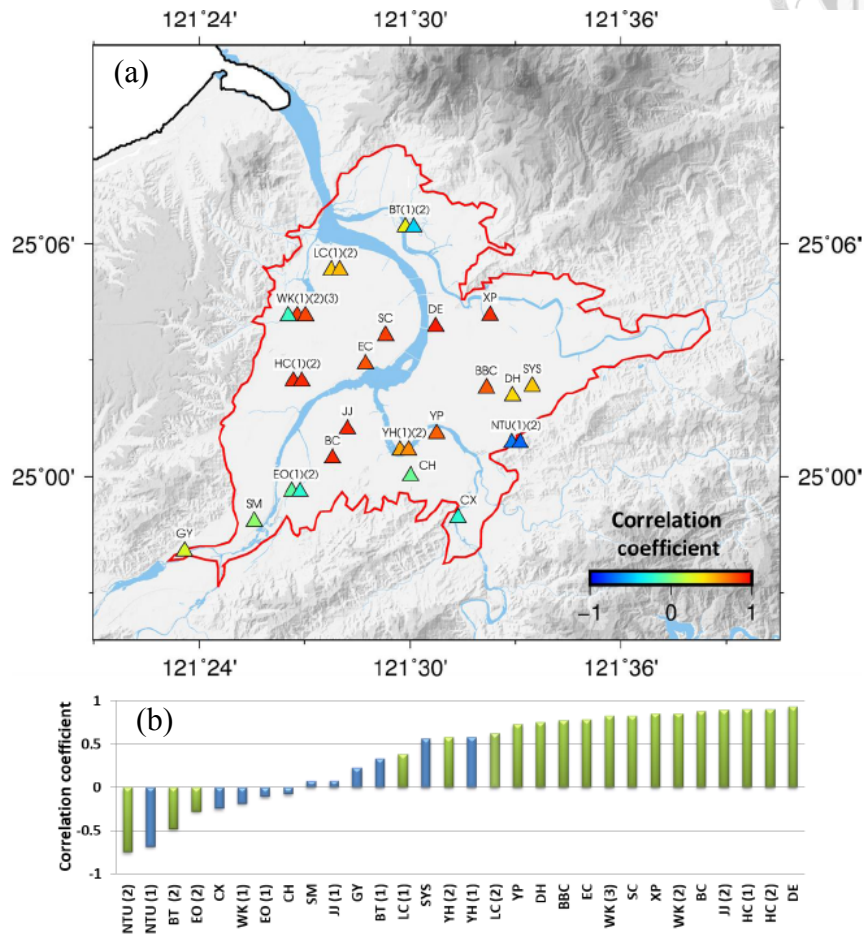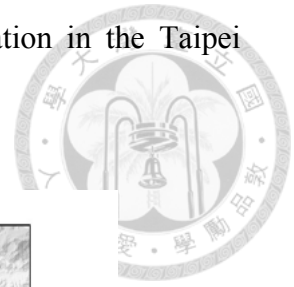
Figure 3-7. (a) The correlation coefficients between PSInSAR-derived deformation and groundwater level change of groundwater wells. (b) The histogram of the correlation coefficients; the blue bars represent unconfined aquifer while green bars are located at confined aquifer (Lee et al., 2018).
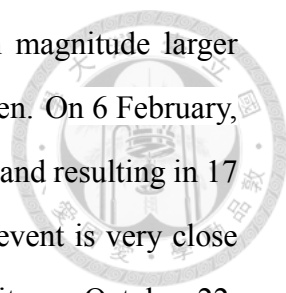
Chapter 4

Triggered slip on multifaults after the 2018 Mw 6.4 Hualien earthquake by continuous GPS and InSAR measurements

This chapter has been originally published in Terrestrial Atmospheric and Oceanic Sciences as the following citation. Please see the whole content in Appendix II.

Tung, H., H.-Y. Chen, Y.-J. Hsu, J.-C. Hu, Y.-H. Chang, and Y.-T. Kuo, 2019: Triggered slip on multifaults after the 2018 Mw 6.4 Hualien earthquake by continuous GPS and InSAR measurements. Terr. Atmos. Ocean. Sci., 30, 285-300, doi: 10.3319/TAO.2019.04.03.01

Starting from 4 February 2018, at least 16 earthquakes with magnitude larger than 4.5 occurred at depths between 3 to 15 km in offshore Hualien. On 6 February, a Mw 6.4 earthquake with a shallow focal depth of 6.3 km occurred and resulting in 17 deaths and 285 injured. The epicenter of mainshock 0206 Hualien event is very close to the historical earthquake events occurred off shore of Hualien city on October 22, 1951 which the earthquake sequences propagated towards south in three month resulting in triggering of big earthquake in Chihshang, Yuli and Taitung (Chen et al., 2008). These Hualien-Taitung earthquake sequences remind people of deeply concerns about the possibility of a large earthquake sequences are getting to start along the Longitudinal Valley. (Fig. 4-1). The extremely large ground shaking (PGA > 400 gals) caused severe building damage, including four ones that had partially collapsed in the city of Hualien. The focal mechanism solution determined from the Broadband Array in Taiwan for Seismology (BATS) and the U.S. Geological Survey (USGS) both considered a NE-striking and NW-dipping nodal plane as the seismogenic fault plane. The other alternative nodal plane is close to a EW-striking south-dipping reverse fault with dextral slip component. However, according to field investigations, the major surface rupture was identified along the Milun fault (Huang et al., 2019, Lin et al., 2019), which favors a NE-striking and east-dipping strike-slip fault with reverse component fault based on geological data.

42
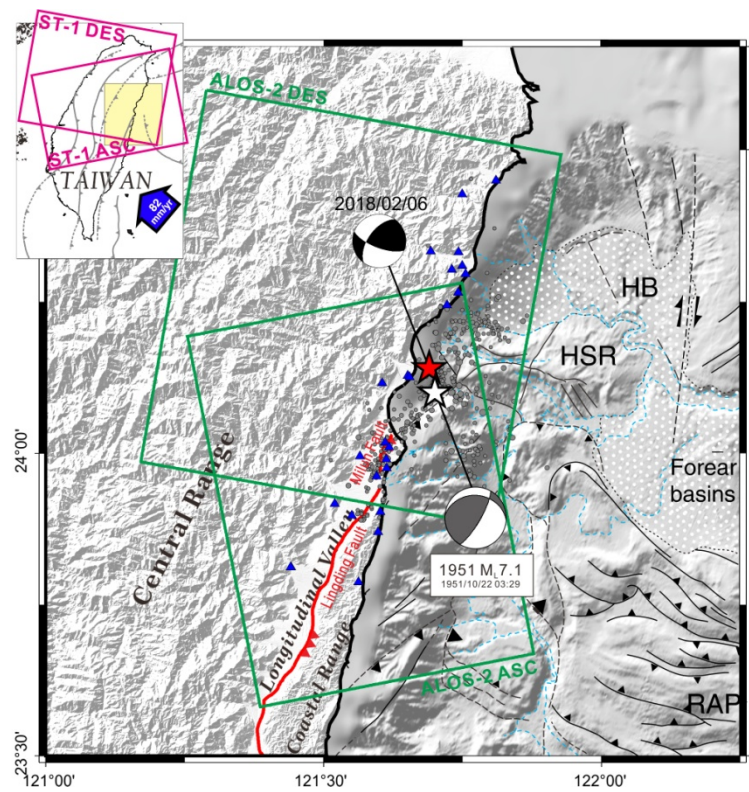
Figure 4-1. Locations for continuous GPS stations (blue triangles), SAR coverage (rectangle) and focal mechanism of the 0206 Hualien earthquakes in Taiwan. Gray circles are the aftershocks occurred within two weeks after the 0206 Hualien event (modified from Tung et al., 2019).

In order to realize the contradiction between the possible west-dipping moment tensor solutions and the east-dipping surface structures caused by this event, continuous GPS (cGPS) data from the Taiwan cGPS array and 12 cGPS sites operated by the NDHU were used to estimate the instantaneous surface ground motion around the epicenter as well as along the Milun and Lingding fault systems. In addition, DInSAR technique from ALOS-2 and Sentinel-1 radar images were applied to fulfill the regional movements and fault ruptures associated with the mainshock. In order to directly compare the coseismic deformation pattern with cGPS data around the Milun and Lingding faults, we combined ascending and descending interferograms to obtain E-W and vertical displacement components (Fig. 4-2) by following equations:
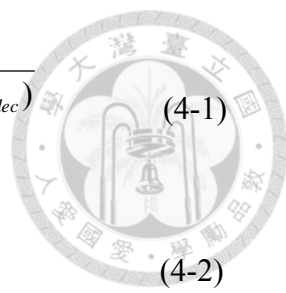
$$E_{component} = \frac{LOS^{(des)} \cdot \cos(\theta_{asc}) - LOS^{(asc)} \cdot \cos(\theta_{des})}{\cos(\alpha_{des}) \cdot \sin(\theta_{des}) \cdot \cos(\theta_{asc}) + \cos(\alpha_{asc}) \cdot \sin(\theta_{asc}) \cdot \cos(\theta_{dec})} \tag{4-1}$$

$$U_{component} = \frac{LOS^{(asc)} + E_{component} \cdot \cos(\alpha_{asc}) \cdot \sin(\theta_{asc})}{\cos(\theta_{asc})} \tag{4-2}$$

Where θ is the incidence angle and α is intersection angle between the trace of satellite (Heading Angle) and the north; *asc* represents ascending orbit while *des* represents descending orbit (details in Table 1 of Appendix II).
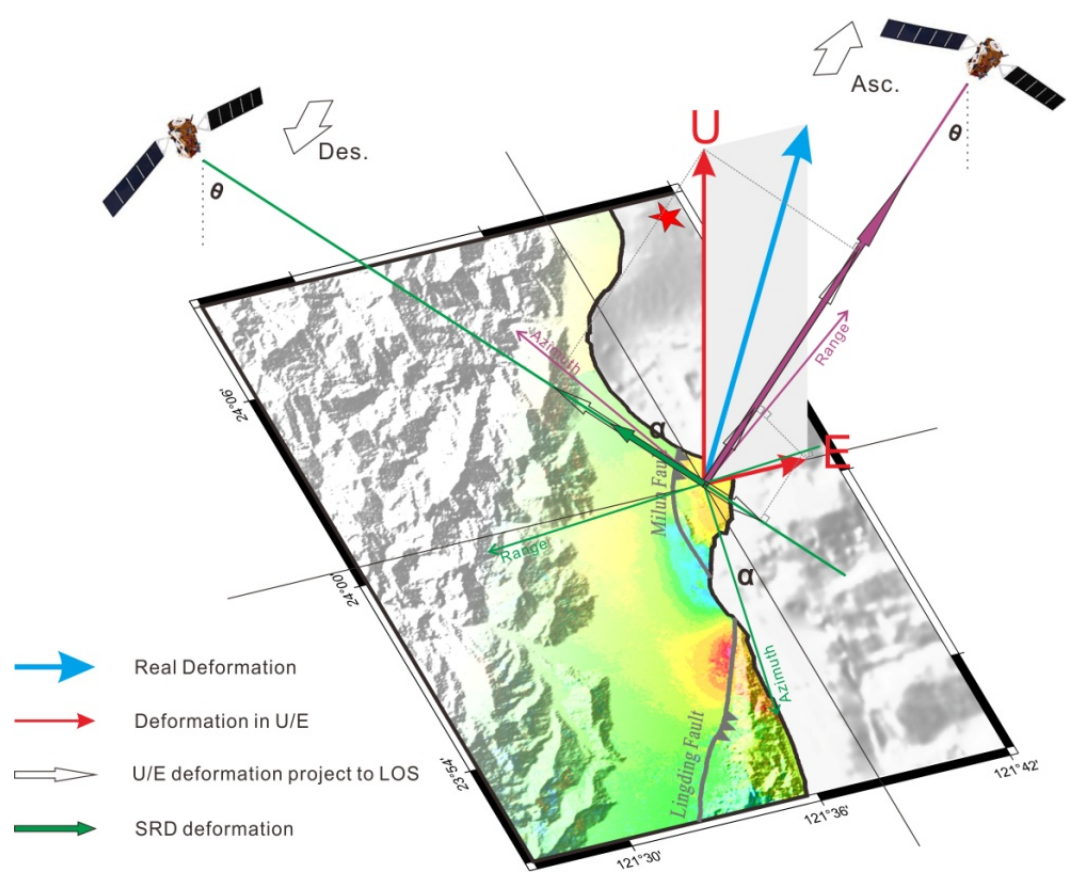
Figure 4-2. Geometrical relationship of the LOS, observed deformation, horizontal and vertical deformation on geodetic measurements and the projection of the vertical and horizontal components onto LOS direction.

44

Overall, the main deformation area of this event concentrated in the Milun fault and the north part of the Lingding fault (Fig. 4-3). The GPS stations and DInSAR results indicate the Milun fault moves as a left-lateral fault with reverse component dipping to the east during this event. However, the coseismic motions of the DInSAR result and GPS stations near the Linding fault are inconsistent with the kinematic behavior of the Lingding fault considered as a NS-striking east-dipping strike-slip fault with thrust component from geological investigations (Chen et al., 2007) and geodetic measurements during the interseismic period (Chen, 1974, Yu and Liu, 1989, (Yu and Kuo, 2001). Thus an unknown west-dipping fault with left-lateral strike-slip component could be triggered during this M_w 6.4 Hualien event. The detailed coseismic displacement has been presented in Tung et al. (2019).
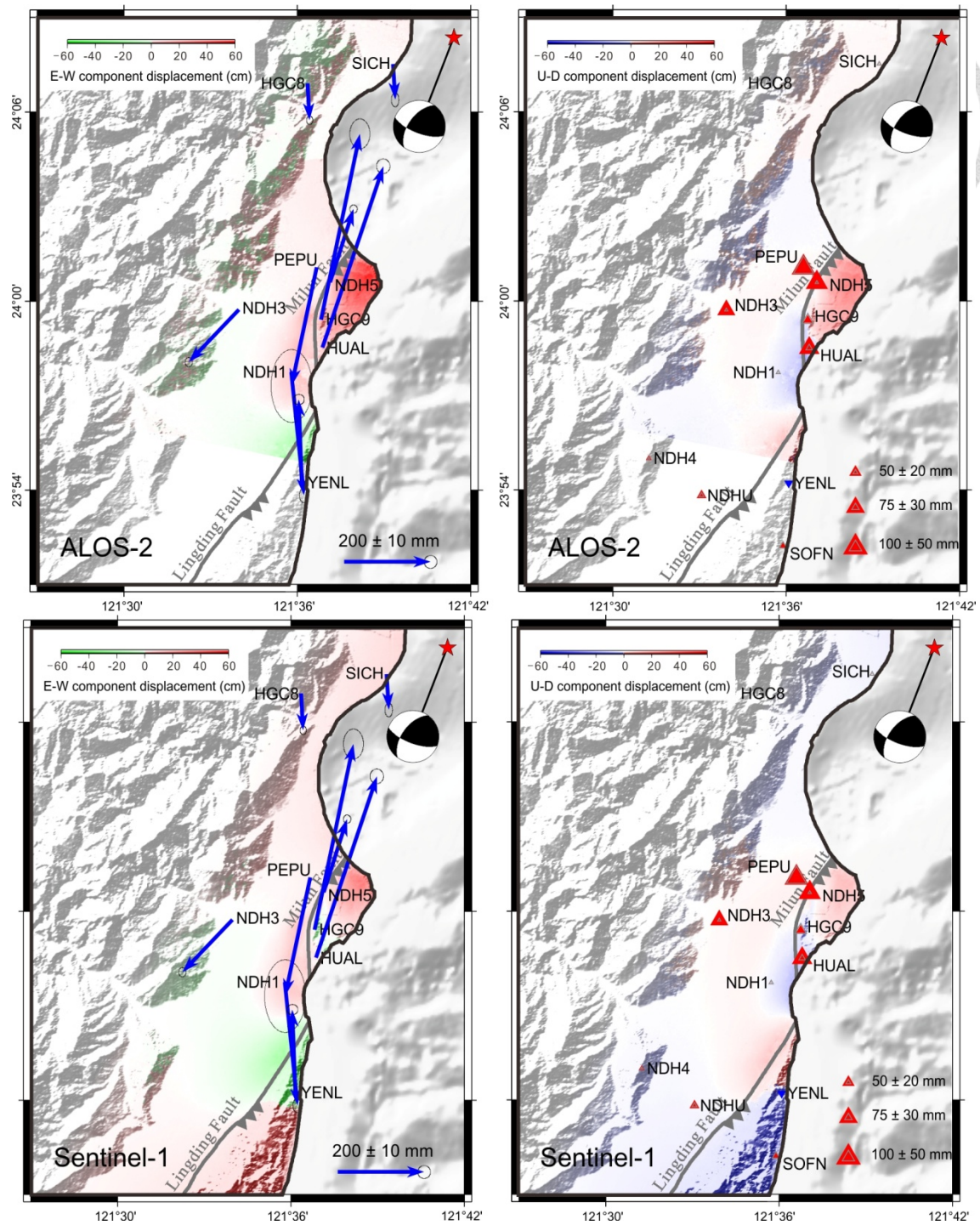
Figure 4-3. Coseismic displacements of cGPS stations and E-W and vertical component of DInSAR results. Red color represents eastward surface rupture and uplift; green color represents westward movement and blue color represents subsidence. Blue arrows represent the GPS horizontal displacements and solid triangles indicate the vertical movements of cGPS stations.

For the source model based on coseismic deformation based on InSAR and GPS, Yang et al. (2018) carried out a 3-faults model with main fault plane of this event composed by the NE-striking seismogenic fault dipping to the west based on the focal mechanism solution from USGS, the Milun fault dipping to the east and the west-dipping fault dipping to the west according to field investigation (Fig. 4-4). After searching in an elastic, homogeneous, and isotropic half-space using the large size of 5 x 5 km, the detailed fault geometry and forward model reliability have been presented in Yang et al. (2018). The estimated fault model can explain more than 98% and 93.4-97.3% of the GPS and InSAR observations with model misfit of 0.9 and 0.9-1.6 cm, respectively, which suggests a high reliability of the estimated faulting model. Also, the forward predicted ALOS-2 and Sentinel-1 InSAR data have a good consistency with the observed results, and the residual in the east of the Milun fault should mainly result from some small shallow folds that have been triggered in the 2018 Hualien earthquake.
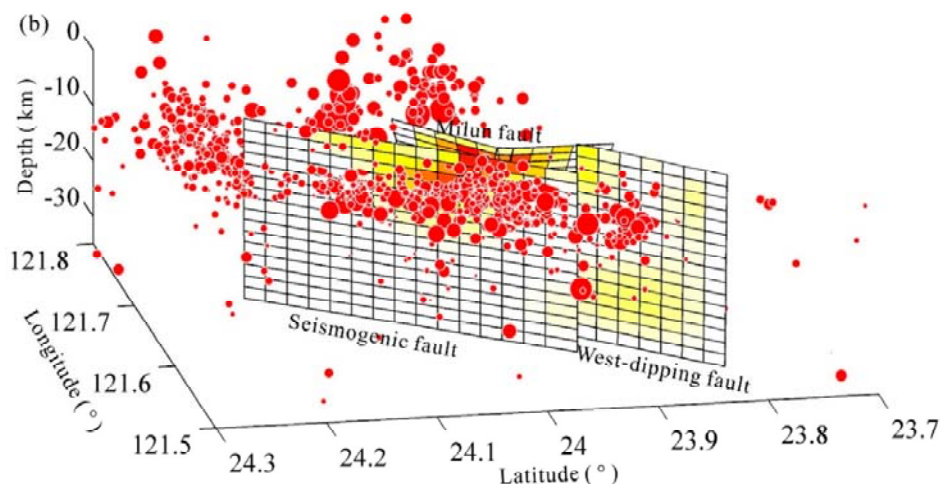
Figure 4-4. Faulting models respectively inferred by DInSAR observations, and the red dots are the aftershocks of this event (Yang et al., 2018).

Except this fault geometry model, (Lee et al., 2018) also suggested that the initial rupture started from a N-S striking and west-dipping fault and propagated southward

with a high rupture speed, then the rupture then jumped to the shallower east-dipping Milun fault, and jumped again to the east-dipping Lingding fault by using joint inversion of teleseismic and GPS data (Fig. 4-5). On the other hand, (Huang and Huang, 2018) use the other nodal plane of the seismogenic fault to construct the fault model of this event suggesting that the earthquake initiated from a SE-NW and south dipping fault and slip transferred into the main NE-SW strike and west-dipping fault (Fig. 4-6). The seismic slip eventually triggered the east dipping Milun fault to slip at shallower depth and caused most of the damage by applied joint inversion of seismic, GPS, InSAR and leveling data. They consider the main west-dipping main fault belongs to a different fault system that is different from the east-dipping Longitudinal Valley fault system (LVF). The west-dipping fault and easting-dipping LVF could be very close in the shallow depth. but close in space at the shallowest part, which is in agreement with our conclusion.
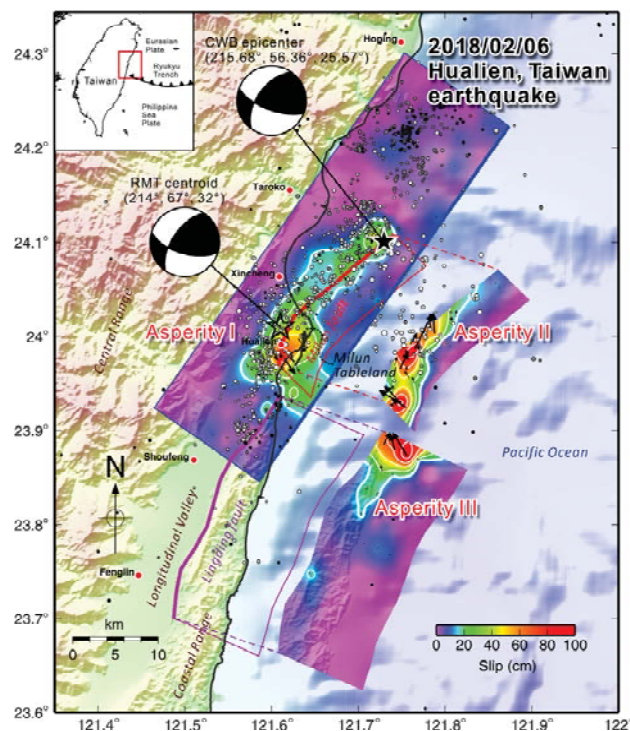
Figure 4-5. Slip distribution on fault models based on joint inversion of GPS and teleseismic data produced by Lee et al. (2018).

48
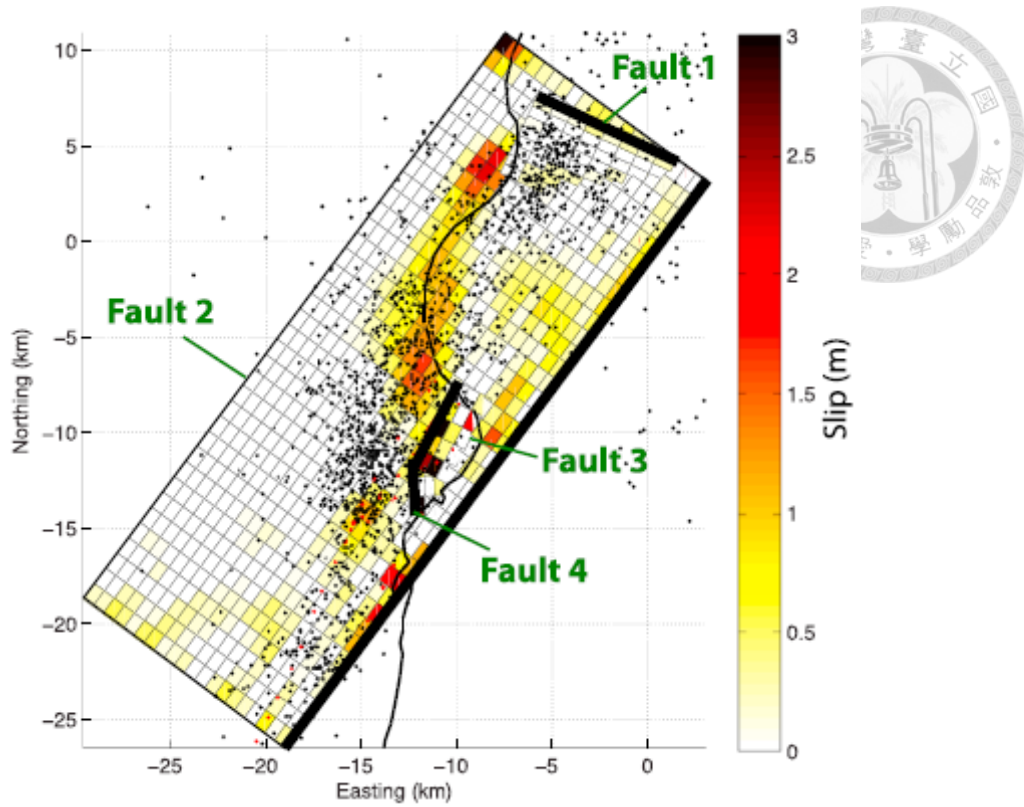
Figure 4-6. Slip distribution on fault models based on the joint inversion of GPS, InSAR and seismic data produced by (Huang and Huang, 2018).

Chapter 5

Coseismic displacements and ground motion recorded by high-rate GPS on Feb. 06, 2016 Meinong earthquake, Taiwan

To realize the movement behaviors and precise displacements caused by M_w 6.4 Meinong earthquake (occurred at about 35 km ESE of the Tainan city with a focal depth of 16.7 km on Feb. 6, 2016), GPS and DInSAR techniques have been utilized to in this event. Daily solution and kinematic positioning by GPS algorithms can determine the co-seismic displacements and ground motions, and the surface deformation information by DInSAR technique can fulfills the regional movement. Combining the results from GPS and DInSAR for the coseismic displacement estimations, the major movement is concentrated within four fault systems, which are Hsin-Hwa fault, Zuo-Jhen fault, Long-Cheun fault and Mei-Ling fault in southwestern Taiwan. The largest coseismic displacement of 64 mm and 63 mm in the horizontal and vertical components occurred at 15 km northwest of the epicenter.

50

5. 1 Introduction
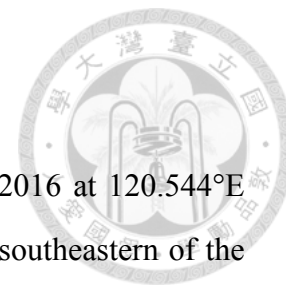
The M_w 6.4 Meinong earthquake occurred on February 6, 2016 at 120.544°E 22.922°N at a depth of 14.6 km, which is located at about 35 km southeastern of the Tainan City, the fourth big city in Taiwan (Fig. 5-1). However Based on the CWB intensity scale, the PGA larger than 400 gals were measured in Hsin-Hwa district, Tainan, where the major ruptures and collapsed building were observed from field investigation. This earthquake is the first inland earthquake with magnitude larger than 6 in Taiwan during 2016 causing severe building damage and 117 deaths and was the deadliest earthquake in Taiwan since the 1999 Chichi earthquake. According to the focal mechanism of this event reported by the USGS, the possible seismogenic fault is a nearly E-W-striking and gently north-dipping thrust fault with a minor sinistral strike-slip component. Which is quite similar with the Jia-Shian earthquake occurred six years ago in 2010 (Huang et al., 2013). The preliminary aftershock catalog by the CWB shows three groups of aftershocks (colored circles in Fig. 5-1) and the spatial distribution of aftershocks has no relation to current known geological structures (Huang et al., 2016;Wen et al., 2017). Thus, to clarify the spatial relationship between the mainshock and the surface deformation is the main intention of this research.

Over the past decade, high-rate GPS positioning have been used for measuring coseismic displacement and ground motion since GPS receiver and data-processing methodologies have been improved. Several large earthquakes were successfully recorded, which proves that high-rate GPS positioning has been developed to obtain epoch-by-epoch positions for earthquake measurements and is capable of recording ground motions for large-magnitude events (Bock et al. (2004) and Larson et al. (2003) for the 2002 Mw 7.9 Denali earthquake, Ohta et al. (2006) for the 2004 Mw 9.3 Sumatra-Andaman earthquake, Shi et al. (2010) and Yin et al. (2010) for the 2008 Mw 8.0 Wenchuan earthquake, and Sato et al. (2011), Yue and Lay (2011) and Hung and

Rau (2013) for the 2011 Mw 9.1 Tohoku-Oki earthquake).

To better characterize surface deformation and movement behavior, we use continuous GPS data from 40 continuously operating reference station (CORS) from the Taiwan cGPS array to estimate the coseismic displacement around the epicenter (Fig. 5-1). In addition, DInSAR technique from ALOS-2 satellite images is used to infer regional coseismic deformation for this earthquake. Furthermore, high-rate GPS data (1-second sampling rate) are applied to estimated the peak ground displacement (PGD) and ground acceleration adjacent to the hypocenter for assessing the potential seismic damage for providing an alternative measurement of earthquake happened in this study.
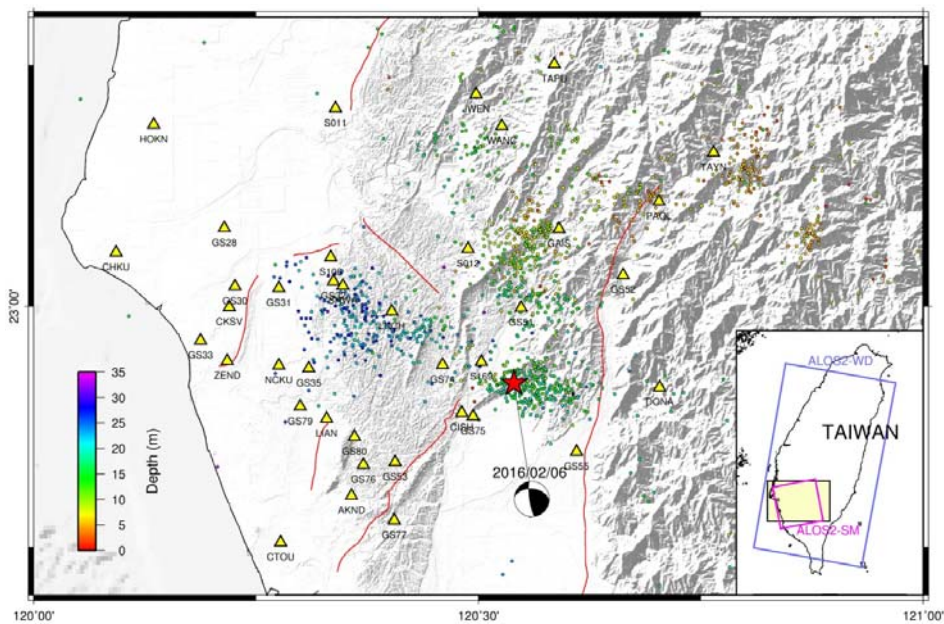
Figure 5-1. Locations for continuous GPS stations (yellow triangles), SAR coverage (blue and pink rectangle), focal mechanism of the 2016 Meinong earthquakes and aftershocks (colored dots) in Taiwan. The red lines are major active faults. WD represents ScanSAR mode while SM represents Stripmap mode image.

5. 2 Data acquisition and processing

To study the instantaneous surface ground motion and permanent displacement caused by the earthquake, we use GPS observations and SAR images to acquire the precise positioning coordinates and the differential movements for the area around the epicenter. GPS data provide a nice temporal resolution for the rupture process where as SAR images offer a better spatial coverage of deformation pattern.

5. 2. 1 GPS observations and data procedures

In order to precisely determine the coseismic displacement and surface ground motion of the Meinong earthquake, we collected cGPS data from 40 stations around the hypocenter with time span from 1st to 8th February with sampling rate of 30-seconds to estimate daily coordinated. Furthermore, 1-second sampling rate data of cGPS are used to both estimate the instantaneous positioning and PGD for assessing the potential seismic damage (detail in discussion).

We utilize the GIPSY-OASIS software to estimate the coordinates in precise point positioning mode for daily positioning and kinematic positioning. The data processing procedure for the GIPSY-OASIS in this study is listed below.

(1) Employ the IGS final orbit and clock information to reduce the effects of the errors.
(2) Utilize the antenna calibration table from provided from NOAA's National Geodetic Survey.
(3) Form the ionosphere-free linear combination of carrier phase observation to mitigate the first order ionospheric bias.
(4) Use the VMF1 (wet and dry based on Vienna) tropospheric mapping function and estimate the residual tropospheric delays.

(5) Apply the ocean loading according to FES2004.

5. 2. 2 DInSAR observations and data procedures

After the Meinong earthquake, ALOS-2 lunched by Japan Aerospace Exploration Agency (JAXA) passed over the Taiwan area for emergency purpose on February 14 and 18 with ScanSAR mode and Stripmap mode, respectively. We use four SAR acquisitions to generate one ScanSAR descending interferogram (2016/01/31 - 2016/02/14) and one Stripmap ascending interferogram (2015/11/26 - 2016/02/18). These two interferograms were formed by using ROI_PAC software developed by the JPL/Caltech (Rosen et al., 2004) and one-arc-second resolution Shuttle Radar Topography Mission (SRTM) digital elevation model is used to remove topography phase component during interferograms processing. Finally, Snaphu version 1.4.2 (Chen and Zebker, 2000) is applied to process the phase unwrapping.

5. 3 Analyses and Results

Both GPS observations and SAR images can estimate the coseismic displacements in different temporal scale. First, we use GPS data with 30-seconds sampling rate for processing static solutions and data with 1-second sampling rate for kinematic positioning to figure out the daily and high-rate solutions. On the other hand, we use two phases of ALOS-2 images to evaluate the regional surface deformation over a week after the mainshock.

5. 3. 1 cGPS result

In order to decrease the sidereal bias for kinematic GPS positioning, sidereal

54

filtering is employed by using two or more data from the other days prior to or post the calculated day. The concept of sidereal filter has two step : (1) apply low-pass filter on estimated epoch-by-epoch positions of day I, which assuming no ground movement on it to remove high-frequency noise which is irrelevant to the satellite-receiver geometry; (2) subtract the filtered day I from the estimated positions with sidereal period (23h 56m 4s) shift (Nikolaidis et al., 2001;Bock et al., 2004). After removing the sidereal bias, the kinematic positioning can provides the coseismic displacements and surface ground motions of the earthquake.

In this study, after removing sidereal biases from the 40 cGPS stations, the standard deviation of GPS waveform reduce efficiency. For example, standard deviation reduces from 18.6 to 8.2 in the E-W component, from 10.4 to 7.5 in N-S component and from 53.0 to 25.2 in vertical component at GPS station CTOU due to the elimination of repeating vibrations between around 19:20:00 and 20:00:00 in both E-W and vertical component (Fig. 5-2) which might related to the environment condition of the station. For the all 40 CORS stations, average standard deviation reduce from 13.3 to 12.2 in E-W component; 11.5 to 9.6 in N-S component and 35.4 to 27.6 in vertical component.
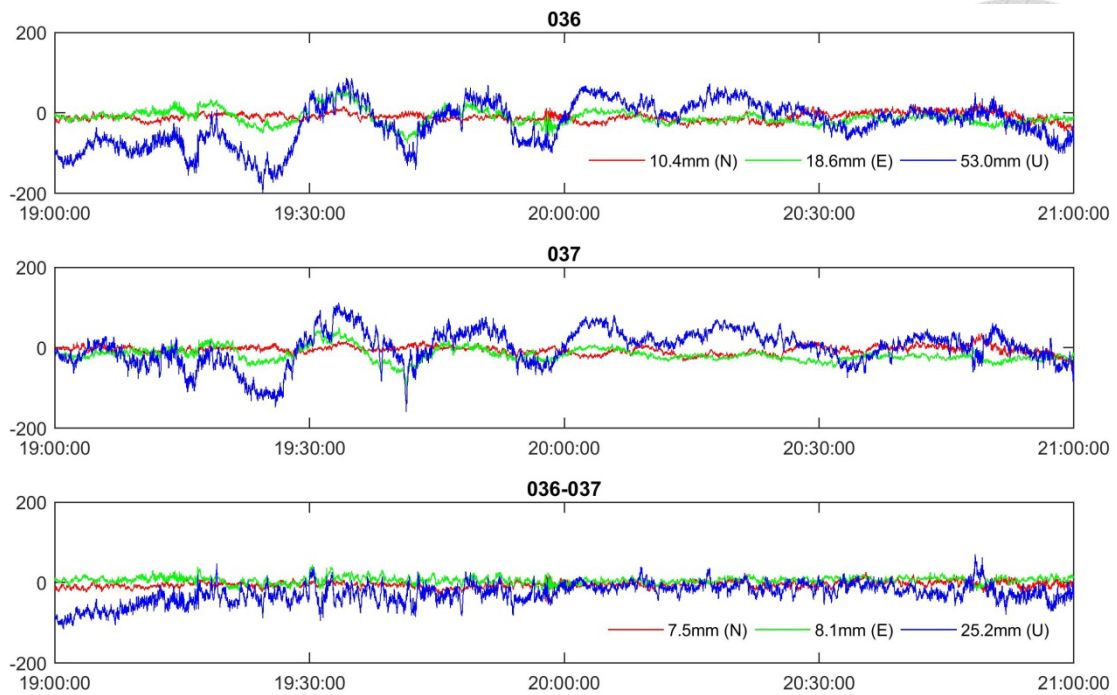
Figure 5-2. Records of 1 Hz GPS data at station, CTOU, during the 2016 Meinong earthquake. A filter algorithm was applied to remove the sidereal repeat noises. The records of the following day (Day 37) of the earthquake were used for comparison to obtain the filtered data.

From the different sampling rate and processing strategy, 2 coseismic displacement fields from GPS data are collected from (1) positions difference between the averages of 1-hz solutions 10 minutes prior to and post the mainshock; (2) difference between the averages daily coordinates 5 days prior to and 2 days post to the mainshock with 30-seconds sampling rate. According to Fig. 5-3, horizontal displacement reveals a southwestern motion near the hypocenter and a fan-shape distribution with vectors toward the west. GPS station GS32 near the town of Hsinhwa shows maximum horizontal displacement of 64.4 mm in the direction of southwest. However, it has been proved that this large displacement caused by rupture of dam. For the vertical displacement, subsidence pattern exhibits at the eastern side the epicenter in the Central Range and uplift pattern at the western side of the epicenter in the Western Foothills. The peak uplift is ~10 cm at station LNCH west of Lungchuan Ridge. There

56

is no obvious differences between the daily solution and kinematic high-rate positioning result since no prominent afterslip displacement have been found in a few days after the earthquake.
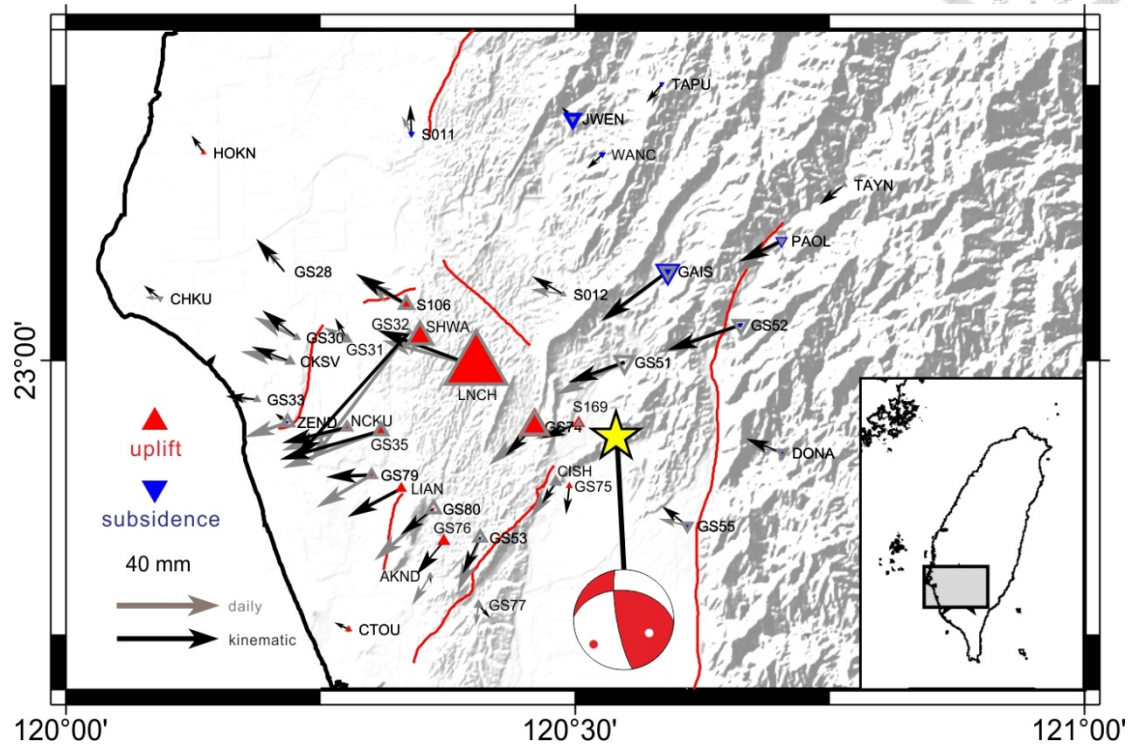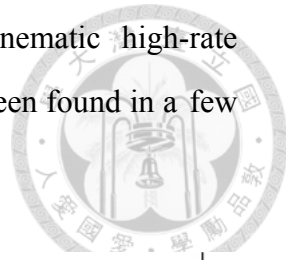
Figure 5-3. Coseismic displacements in Meinong earthquake. The symbol arrows present the horizontal displacement (black for kinematic and grey for daily solutions) and the symbol triangles show the vertical movement (red and blue for kinematic and grey for daily solutions). The epicenter denotes in the yellow star.

5. 3. 2 DInSAR result

According to the result from DInSAR technique, the main deformation area occurs far west the epicenter but located around southwest of Zuo-Jhen fault, southeast of Hsin-Hwa fault, east of Houchiali fault, and northwest of Chishan fault. Both ascending and descending interferograms show range decrease with almost 100 mm to the south of the station LNCH with a N-S trending round-shape deformation area.

57

Range increase presents to the east of the epicenter, especially in the descending interferogram. Moreover, a reverse range pattern (increase in ascending and decrease in descending) can be observed near Guanmiao area and Hsinhwa, which indicates pure horizontal movement in this area.
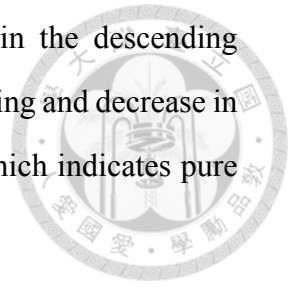
By combining ascending and descending interferograms, a 2.5 dimension (E-W direction component and Vertical component) coseismic deformation can be performed in figure 5-4b and d. Compare with GPS daily solution from chapter 3.1, the most uplift area is located in the western part of the epicenter between Tainan City and Lungchuan with uplift of about 10 centimeters. The reverse range pattern revealed in interferograms here can be example by the horizontal displacement with pure eastward movement in Guanmiao area and Hsinhwa. Besides, there is no significant discontinuities deformation across all the active faults such as Houchiali fault, Chishan fault, Zuo-Jhen fault and Hsin-Hwa fault in this area which indicates these faults were not triggered by this event. On the other hand, the deformation is concentrated in Kutingken Formation, which implies the active tectonic in Kutingken Formation is the main control factor during this event.
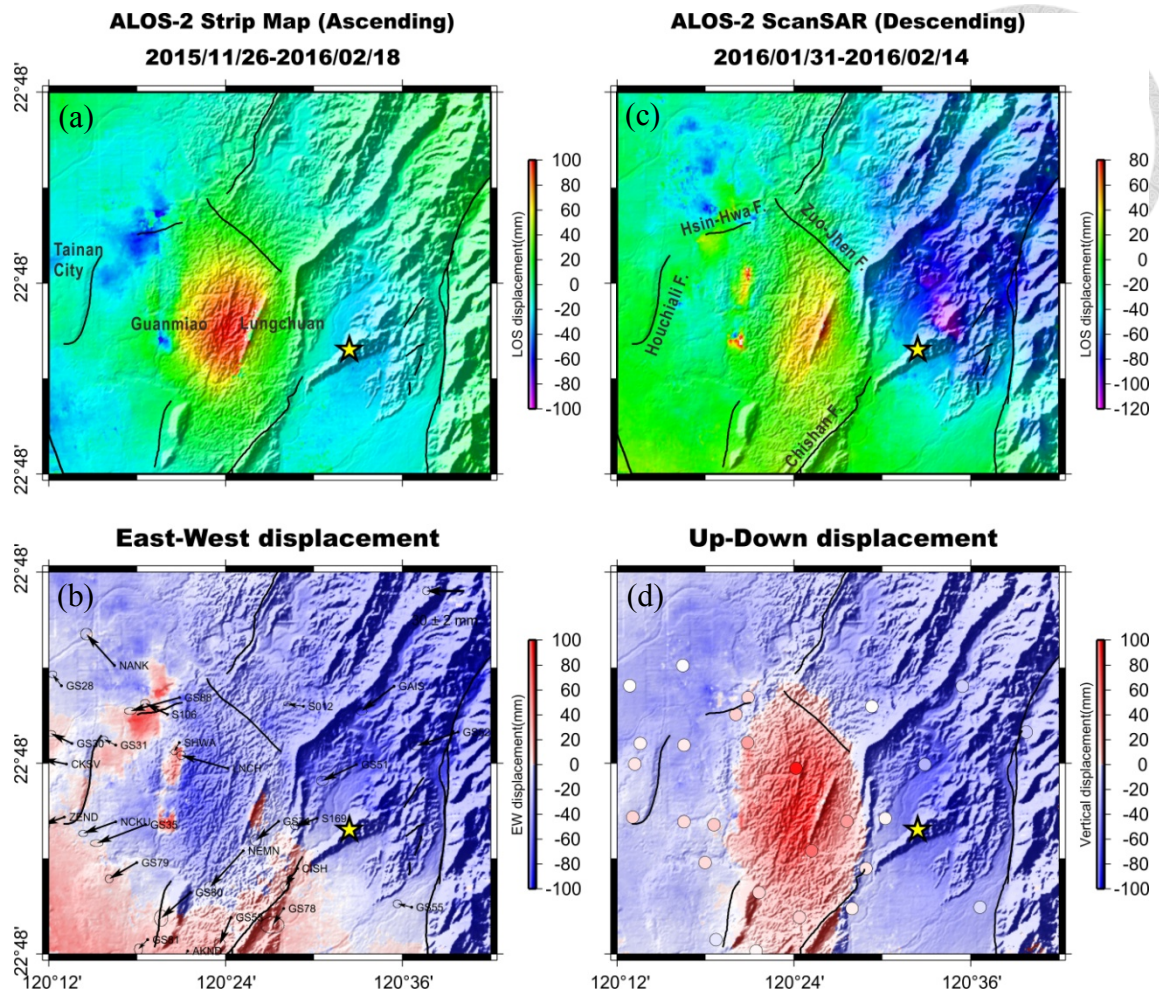
Figure 5-4. (a)(c) DInSAR results acquire from ALOS-2 satellite. (a)(b) denotes the Strip mode ascending pair and (c)(d) shows the ScanSAR mode descending pair. (b)(d) 2.5 dimension coseismic displacements converted from ascending and descending interferograms (red color represents eastward and uplift; blue color represents westward and subsidence). The symbol arrows present the GPS horizontal displacement and the symbol circles show the vertical movement. The epicenter denotes in the yellow star.

5. 3. 3 Finite source inversion model

Huang et al. (2016) propose a two-fault model, the geometry of main fault at $15-20$ km depth determined by seismic and GPS data and the other shallower fault at

59

5 – 10 km in the upper crust decided from residual of forward InSAR displacement on the main fault, to describe the Meinong deformation. After the geometry of the two fault were determined, all data sets (seismic waveforms, GPS, and InSAR) were used to constrain slip distribution on both faults. After comparing InSAR observation and model prediction, additional movement of the fault-and-fold system in Guanmiao and Lungchuan (black arrows in Fig. 5-5e and j) may have been induced during the main shock producing sharp and localized surface deformation where can be observed from field investigation (details of model procedures in (Huang et al., 2016).
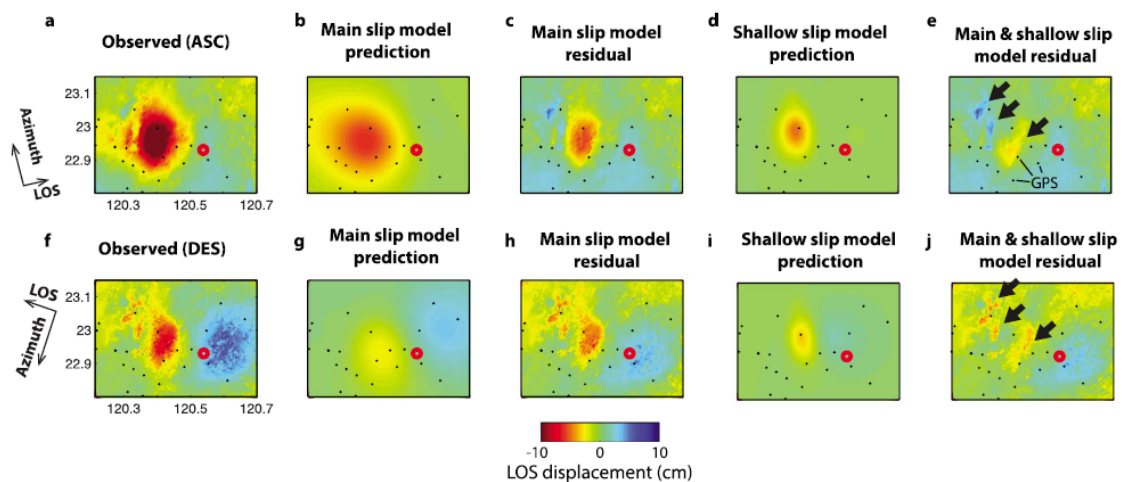
Figure 5-5. Observed Sentinel-1A ascending and descending InSAR data and model fitting from the main and shallower faults. The red circle and black dots are the earthquake epicenter and GPS stations (Huang et al., 2016).

5. 4 Discussion

High-rate GPS positioning techniques have been developed to obtain epoch-by-epoch positions and these solutions are capable of recording seismic motion, which is called "GPS Seismology." In this study, we analyze the kinematic positioning

result after sidereal filtering of 40 CORS with 1-second sampling rate to estimate the peak ground displacement and peak ground acceleration nearby the hypocenter.
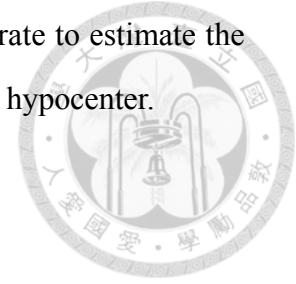
5. 4. 1 Peak ground displacement

Following the study of magnitude scaling properties of peak ground displacement (Melgar et al., 2015), Equation (5-1) is used to determine peak ground displacement, where N(t), E(t) and U(t) are the north, east and vertical displacement in each epoch, respectively. Figure 5-6 shows GPS waveforms and calculated PGD value in time series. After calculating the 40 CORS near the epicenter, almost all stations represent larger vibration in E-W component. The maximum peak ground motion value is recorded at GPS station GS31, which is located at northeast of Houchiali Fault. In addition, most GPS stations with large PGD value are concentrated in Hsinhwa area, south of Hsin-Hua Fault, where is also the locations of damage buildings (green triangles in Fig. 5-7).

$$PGD = \max\left(\sqrt{N(t)^2 + E(t)^2 + U(t)^2}\right)$$

(5-1)
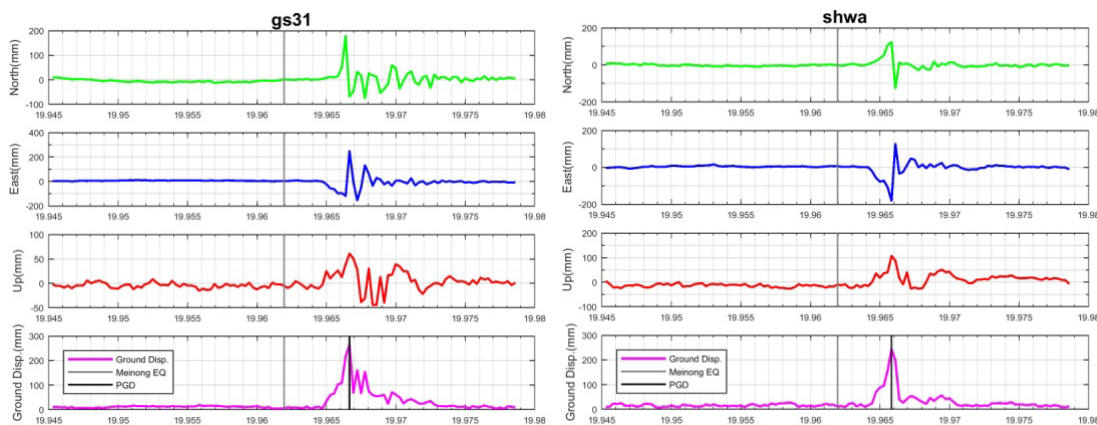
Figure 5-6. Time-series of cGPS stations GS31 and SHWA. Gray line represents occurring time of the main shocks of the Meinong events; black line indicates the arrival time of PGD.

61
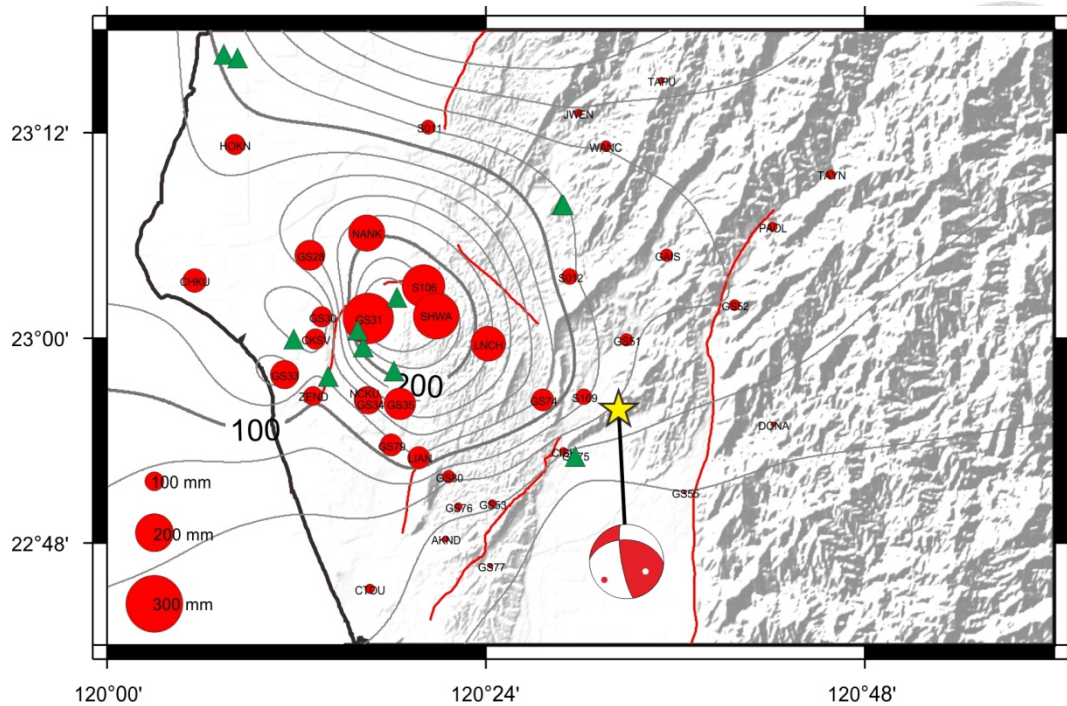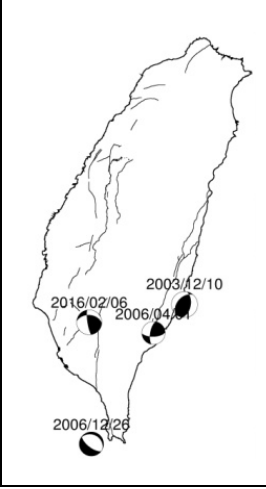
Figure 5-7. Peak ground displacement estimation for near epicenter CORS. The red circles present the peak ground displacement of each station. The green triangles indicate collapsed houses during this event. The epicenter denotes in the yellow star.

After using the regression equation (5-2) to calculate the moment magnitude by using the scaling property between PGD and the hypocentral distance (R), we computed a geodetic moment magnitude of the Meinong Earthquake as 6.3, which is slightly larger than the centroid moment-tensor solution derived from inversion of BATS waveforms. (Mw 6.1). On the other hand, three more moderate magnitude events occurred around the Taiwan area were calculated by the same equation. Most of the Mw are close to but slightly smaller than Mw provided by seismometer (Fig. 5-8).

$$\log(\text{PGD}) = A + B \cdot \text{Mw} + C \cdot \text{Mw} \cdot \log(R) \quad \text{where} \quad \begin{aligned} A &= -4.434 \pm 0.141 \\ B &= 1.047 \pm 0.022 \\ C &= -0.138 \pm 0.003 \end{aligned} \quad (5\text{-}2)$$

Table 5-1. Comparison the M_W values derived from seismometer and GPS

		IES BATS CMT Solution	High-rate GPS PGD scaling	No. of GPS Sites Used
	2016/02/05	$M_W = 6.1$ (misfit = 0.705)	$M_W = 6.3$ (STD = 0.41)	40
	2006/12/26	$M_W = 6.7$ (misfit = 0.651)	$M_W = 6.8$ (STD = 0.19)	15
	2006/04/01	$M_W = 6.1$ (misfit = 0.496)	$M_W = 6.0$ (STD = 0.10)	5
	2003/12/10	$M_W = 6.5$ (misfit = 0.553)	$M_W = 6.4$ (STD = 0.26)	12

5. 4. 2 Peak ground acceleration

Peak ground acceleration (PGA) is equal to the maximum ground acceleration that occurred during earthquake shaking at a location. These values represent intensity of shaking behavior, which provides the index of seismic capability for building constructions. In this study, we differentiated surface displacement twice to get the PGA value of each GPS station by using sampling rate of 1 Hz, 5 Hz, 10 Hz and 50 Hz, respectively (Fig. 5-8). Then we compare the results with seismograms to find the suitable frequency for analyzing PGA values from high-rate GPS records.

According to Wu et al. (2016) and Hsu et al. (2016), the maximum intensity of the Meinong Earthquake reached 7 (PGA > 400 Gal) as recorded by P-alert seismic network, the MEMS accelerometers designed for Earthquake Early Warning and near-real-time shake maps using P-wave information. In this study, we only analyzed horizontal component and ignore the vertical component due to its the vast uncertainty. The result in figure 5-8 shows four different PGA value in different directions (NS and EW). After differentiated twice from GPS displacement results, the PGA values from 1-Hz and 5-Hz data show significant stand out value during shake, however it may

63

underestimate due to its insufficient frequency. On the other hand, 50-Hz data represents huge value and more the background noise when differentiating. Thus, 10-Hz GPS record is more suitable for analyzing PGA values. Figure 5-9 shows the 10-Hz GPS PGA values superposed on GPA shake map collected from P-alter system and NCREE (National Center for Research on Earthquake Engineering) real-time strong-motion networks. The coincidence also represent 10 Hz GPS data is proper frequency for shake map producing.
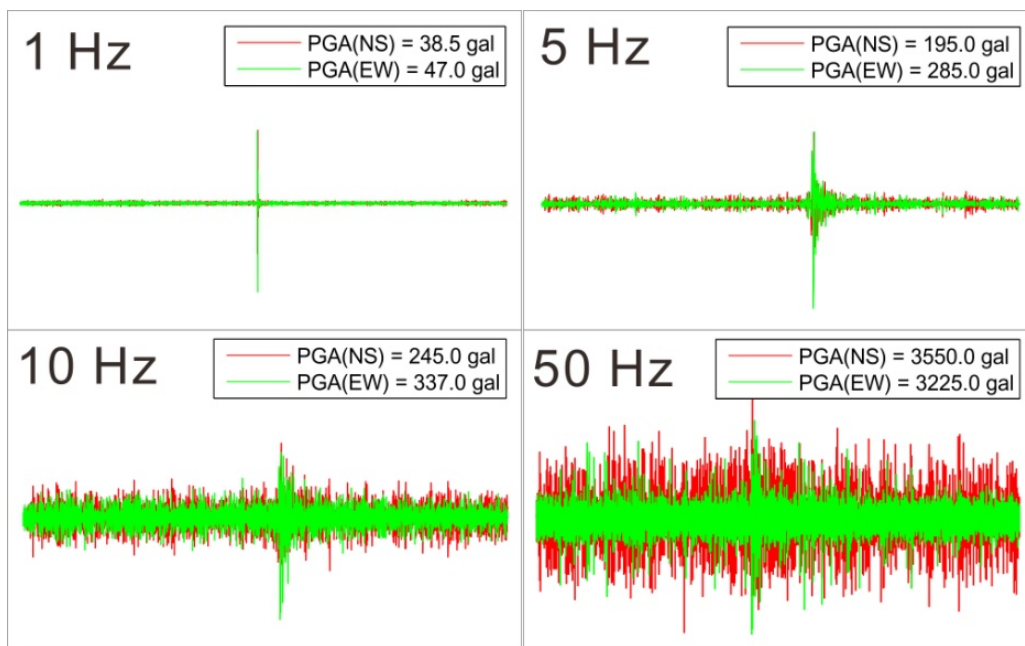
Figure 5-8. The PGA value of SHWA GPS stations by using sampling rate of 1Hz, 5Hz, 10Hz and 50Hz, respectively. The PGA values are shown in each subplot.
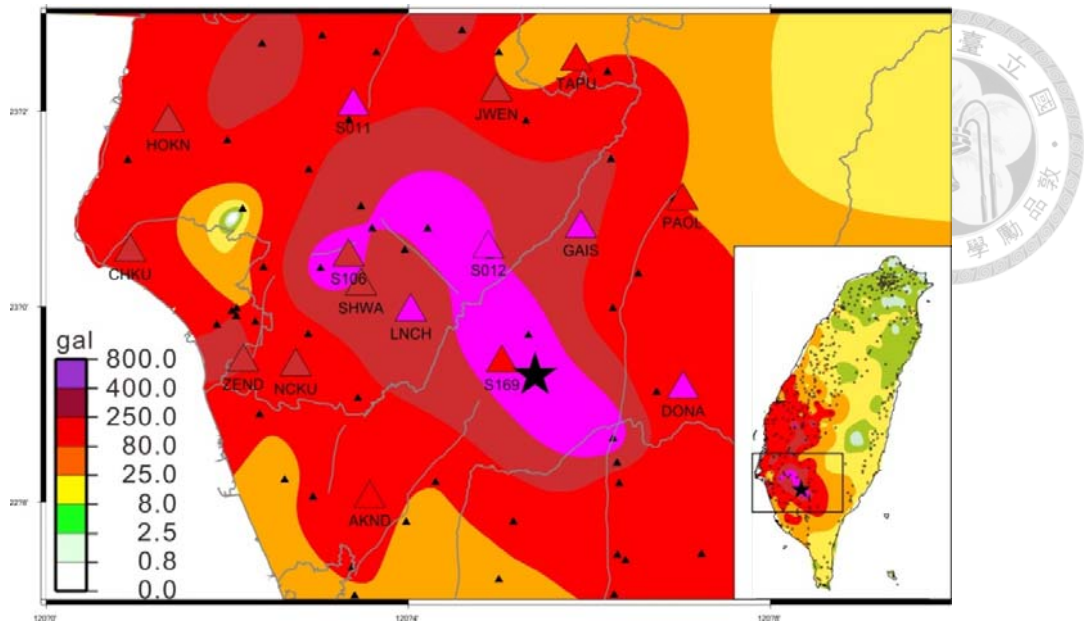
Figure 5-9. The PGA value of GPS stations by using sampling rate 10Hz (colored triangles) superposed on ground shake map produced by Palter and NCREE's on-site warning system (NEEWS) (black triangles).

5. 5 Summary

According to the GPS daily solution and DInSAR deformation map, the most uplift area is located in Longci area. The peak uplift is ~10 cm at station LNCH west of Lungchuan. For the 1 Hz high-rate GPS data, vertical accuracy increased after using the sidereal filter. The first movement time shows the earthquake occurred and then propagated to the N-W direction, which presents the same behavior with slip distribution on fault plane. The maximum PGD value revealed at station GS31 east of the Tainan city, where numbers of building collapsed. Relationship between PGD and distance between station and hypocenter result in a geodetic moment equivalent to a Mw5.9 earthquake .

For the ground motion estimation, the largest peak ground displacement (PGD)

of 260 mm occurred at station GS31 30 km northwest of the epicenter while its coseismic displacement is only 20 mm, we analyzed 40 CORS to estimate the magnitude scaling properties from peak ground displacement (Melgar et al., 2015). We calculated moment magnitude of about 6.3, which is slightly higher than that *Mw* 6.1 reported by the BATS (Broadband Array in Taiwan for Seismology). In this study we investigated some other earthquakes and they all show similar behavior. In order to compute the ground acceleration, we differentiated surface displacement twice to get the PGA value of each GPS station by using sampling rate of 1Hz, 5Hz, 10Hz and 50Hz to compare with seismometers to find the suitable frequency for estimating PGA values from high-rate GPS record. We only use the horizontal component because the vertical component has large uncertainty. The result shows PGA values from 1-Hz and 5-Hz GPS are smaller than PGA value calculated from seismometers, 50-Hz GPS data reveals huge value and more the background noise when differentiating from displacement to acceleration. Therefore, 10-Hz GPS record is the most suitable frequency for analyzing seismic acceleration, which shows almost the same value which seismometer record.

Chapter 6

Conclusion and Future Work

6. 1 Conclusions
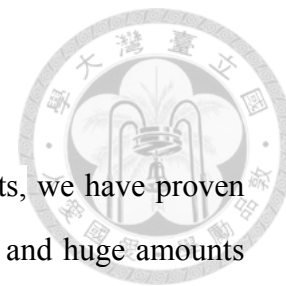
In this era with massive satellite-based geodetic measurements, we have proven that we have abilities to digest and preliminary analysis the latest and huge amounts continuous GPS and SAR data, providing a research platform to offer a fast service enable specialist and non-specialist scientists to study processing causing Earth deformation. We also applied continuous GPS data and SAR images on Taipei tableland to monitor groundwater withdraw induced land deformation and coseismic deformation caused by two medium earthquake occurred in Meinong and Hualien, respectively. The conclusions are listed in the followings:

In chapter 3. The transient deformation of PSInSAR result suggested that the severe land subsidence in the Taipei Basin is highly related to confined aquifer deformation of Jingmei and Wuku Formations. Thus the distribution and thickness of Jingmei and Wuku Formations is an important issue for study groundwater induced deformation in the Taipei Basin. The calculated storativity is roughly constant with values between 0.5×10^{-4} and 1.6×10^{-3} in Jingmei Formation and 0.8×10^{-4} and 1.4×10^{-3} in Wuku Formation. The high correlation indicated that one meter groundwater level change will induce 5 to 16 millimeter surface deformation change, which is about eight times faster than long-term tectonic deformation rate in this area. Thus, to access the activity of the Shanchiao Fault, it is important to discriminate tectonic movement from anthropogenic or seasonal effect in the Taipei Basin to better understand the geohazards and mitigation in the Taipei metropolitan area.

In chapter 4. Significant coseismic deformation reveled by SAR interferograms and GPS on the Milun fault and northern Lingding fault implies that the Milun fault and an unknown west-dipping fault close to the Lingding fault were triggered

69

during the 2018 Hualien event occurred. Also the arrival time of the PGD based on high-rate GPS waveforms indicate a long delay compared to a typical wave propagation velocity, suggesting the same conclusion.
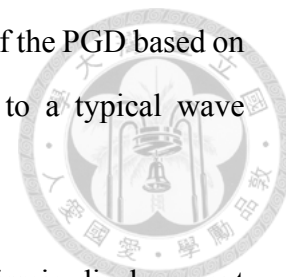
In chapter 5. Combining the results from GPS and DInSAR coseismic displacement estimations of the 2016 Meinong earthquake, the most uplift area is located between Tainan City and Lungchuan with uplift of 10 centimeter, and a fan-shape distribution with vectors toward the west except in local area like Guanmiao and Hsinhwa with eastward movement. Moreover, the major movement show highly related with the Kutingken Formation, implies the active tectonic in Kutingken Formation is the main control factor during this event. Continuous GPS stations with large PGD values are located in the south of Hsin-Hua fault and east of Houchiali fault, where is consistent with the locations of damage buildings. Thus, the immediate results of geodetic observations can provide reliable information of earthquake hazard assessment.

Several SAR processing software packages exist but most of them are quite difficult to handle by a novice. With plenty experience on SAR images processing, a list of existing SAR processing software I have used can be seen in Table 6-1. Although proprietary-and-commercial packages, such as: GAMMA (GAMMA Remote Sensing and Consulting AG) from Switzerland and ENVI SARscape, take advantages of regular and frequent updates, and enable the assimilation of data acquired by the last launched SAR systems. The free-of-charge and open-source programs could enable a real expansion of the use of these techniques by anyone which is interested in SAR processing.

70

Table 6-1. Free-of-charge INSAR software packages (in August 2019)

Name	Institute	SAR processor	Supported SAR satellite sensors	Release
ROI_PAC	Caltech/JPL	DInSAR	JERS, RADARSAT, ERS, ENVISAT, ALOS-1	3.0.1 (2009)
DORIS	TUDelft	DInSAR	JERS, RADARSAT, ERS, ENVISAT, ALOS-1	4.02 (2012)
ISCE	Caltech/JPL	DInSAR	ERS, ENVISAT, RADARSAT, KOMPSAT5,ALOS, ALOS2, COSMO_SKYMED, RISAT1, Sentinel1, TERRASARX, UAVSAR	2.2.0 (2018)
StaMPS/MTI	Stanford	PSInSAR	ERS, ENVISAT, RADARSAT, ALOS-1, TerraSAR-X, COSMO-SkyMed	4.1-beta (2018)
SNAP	ESA	DInSAR	Sentinel	7.0.0 (2019)
GMTSAR		DInSAR. PSInSAR	ERS, Envisat, Radarsat-2, ALOS-1, ALOS-2, TerraSAR-X, COSMOS-SkyMed, Sentinel-1A	5.7 (2019)

6. 2 Future Directions

1. Since the GIPSY-OASIS support by JPL will be phased out and replaced with

    a more capable, modern software package, GIPSYX, soon in the future. Also,

the International GNSS Service (IGS) adopted a new reference frame, called IGS14, on 29 January 2017. The priority of our next step is to reprocess all the GPS data back to the beginning with this new software package in the latest IGS14 frame.
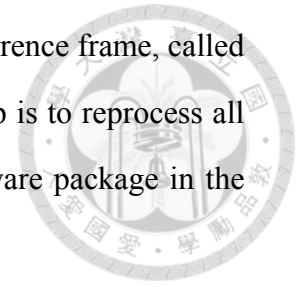
2. Taiwan Earthquake Model (TEM) evaluates earthquake hazard and risk models by constructing a complete and updated seismogenic structure database for Taiwan to assess future seismic hazards. Geodetic Strain rate analysis can be consider as a proxy for earthquake potential gives the probability of all possible major earthquake ruptures throughout the region and over a specified time span. Thus, the strain rate analysis geodetic measurements such as GPS and PSInSAR results are the next task of our work makes TEM more complete.

3. InSAR and GPS are both sensible to tropospheric and ionospheric delay of the electromagnetic signal during its way through atmosphere, which affect the quality of the ground displacement. Thus, apply independent atmospheric corrections from GPS and weather model on our routing InSAR products will help generate more reliable time series and deformation map to characterize seismic hazard and damage assessment in Taiwan.

4. Previous studies has shown that L-Band ALOS data give better spatial density while measuring mountainous Taiwan. ALOS-2 is the follow-on JAXA L-SAR satellite mission of ALOS launched in 2014. The PALSAR-2 radar is a significant upgrade from the previous one, allowing ScanSAR mode with shooting area of 250 kilometers. Thus, apply PALSAR-2 images on our routing InSAR products will help monitor vegetation area more meticulous.

References

Amelung, F., S. Jonsson, H. Zebker and P. Segall (2000). "Widespread uplift and 'trapdoor' faulting on Galapagos volcanoes observed with radar interferometry." *Nature* **407**(6807): 993-996. doi: 10.1038/35039604.

Angelier, J., J.-C. Lee, H.-T. Chu, J.-C. Hu, C.-Y. Lu, Y.-C. Chan, L. Tin-Jai, Y. Font, B. t. Deffontaines and T. Yi-Ben (2001). "Le séisme de Chichi (1999) et sa place dans l'orogène de Taiwan." *Comptes Rendus de l'Académie des Sciences - Series IIA - Earth and Planetary Science* **333**(1): 5-21. doi: https://doi.org/10.1016/S1251-8050(01)01563-4.

Azua, B. M., C. DeMets and T. Masterlark (2002). "Strong interseismic coupling, fault afterslip, and viscoelastic flow before and after the Oct. 9, 1995 Colima-Jalisco earthquake: Continuous GPS measurements from Colima, Mexico." *Geophysical Research Letters* **29**(8). doi: 10.1029/2002gl014702.

Bawden, G. W., W. Thatcher, R. S. Stein, K. W. Hudnut and G. Peltzer (2001). "Tectonic contraction across Los Angeles after removal of groundwater pumping effects." *Nature* **412**(6849): 812-815. doi: 10.1038/35090558.

Beauducel, F., P. Briole and J. L. Froger (2000). "Volcano-wide fringes in ERS synthetic aperture radar interferograms of Etna (1992-1998): Deformation or tropospheric effect?" *Journal of Geophysical Research-Solid Earth* **105**(B7): 16391-16402. doi: 10.1029/2000jb900095.

Bock, Y., L. Prawirodirdjo and T. I. Melbourne (2004). "Detection of arbitrarily large dynamic ground motions with a dense high-rate GPS network." *Geophysical Research Letters* **31**(6). doi: 10.1029/2003gl019150.

Calais, E., J. Y. Han, C. DeMets and J. M. Nocquet (2006). "Deformation of the North American plate interior from a decade of continuous GPS measurements." *Journal of Geophysical Research-Solid Earth* **111**(B6). doi: 10.1029/2005jb004253.

Champenois, J., B. Fruneau, E. Pathier, B. Deffontaines, K. C. Lin and J. C. Hu (2012). "Monitoring of active tectonic deformations in the Longitudinal Valley (Eastern Taiwan) using Persistent Scatterer InSAR method with ALOS PALSAR data." *Earth and*

Planetary Science Letters **337**: 144-155. doi: 10.1016/j.epsl.2012.05.025.

Chang, C. P., J. Y. Yen, A. Hooper, F. M. Chou, Y. A. Chen, C. S. Hou, W. C. Hung and M. S. Lin (2010). "Monitoring of Surface Deformation in Northern Taiwan Using DInSAR and PSInSAR Techniques." *Terrestrial Atmospheric and Oceanic Sciences* **21**(3): 447-461. doi: 10.3319/tao.2009.11.20.01(th).

Cheloni, D., V. De Novellis, M. Albano, A. Antonioli, M. Anzidei, S. Atzori, A. Avallone, C. Bignami, M. Bonano, S. Calcaterra, R. Castaldo, F. Casu, G. Cecere, C. De Luca, R. Devoti, D. Di Bucci, A. Esposito, A. Galvani, P. Gambino, R. Giuliani, R. Lanari, M. Manunta, M. Manzo, M. Mattone, A. Montuori, A. Pepe, S. Pepe, G. Pezzo, G. Pietrantonio, M. Polcari, F. Riguzzi, S. Salvi, V. Sepe, E. Serpelloni, G. Solaro, S. Stramondo, P. Tizzani, C. Tolomei, E. Trasatti, E. Valerio, I. Zinno and C. Doglioni (2017). "Geodetic model of the 2016 Central Italy earthquake sequence inferred from InSAR and GPS data." *Geophysical Research Letters* **44**(13): 6778-6787. doi: 10.1002/2017gl073580.

Chen, C. T., J. C. Hu, C. Y. Lu, J. C. Lee and Y. C. Chan (2007). "Thirty-year land elevation change from subsidence to uplift following the termination of groundwater pumping and its geological implications in the metropolitan Taipei Basin, Northern Taiwan." *Engineering Geology* **95**(1-2): 30-47. doi: 10.1016/j.enggeo.2007.09.001.

Chen, W. S., I. C. Yen, K. P. Fengler, C. M. Rubin, C. C. Yang, H. C. Yang, H. C. Chang, C. W. Lin, W. H. Lin, Y. C. Liu and Y. H. Lin (2007). "Late Holocene paleoearthquake activity in the middle part of the Longitudinal Valley fault, eastern Taiwan." *Earth and Planetary Science Letters* **264**(3-4): 420-437. doi: 10.1016/j.epsl.2007.09.043.

Chiang, K. W., W. C. Peng, Y. H. Yeh and K. H. Chen (2009). "Study of Alternative GPS Network Meteorological Sensors in Taiwan: Case Studies of the Plum Rains and Typhoon Sinlaku." *Sensors* **9**(6): 5001-5021. doi: 10.3390/s90605001.

D'Agostino, N., D. Cheloni, S. Mantenuto, G. Selvaggi, A. Michelini and D. Zuliani (2005). "Strain accumulation in the southern Alps (NE Italy) and deformation at the northeastern boundary of Adria observed by CGPS measurements." *Geophysical Research Letters* **32**(19). doi: 10.1029/2005gl024266.

Feng, G. C., Z. W. Li, X. J. Shan, B. Xu and Y. N. Du (2015). "Source parameters of the

2014 Mw 6.1 South Napa earthquake estimated from the Sentinel 1A, COSMO-SkyMed and GPS data." *Tectonophysics* **655**: 139-146. doi: 10.1016/j.tecto.2015.05.018.

Ferretti, A., F. Novali, R. Bürgmann, G. Hilley and C. Prati (2004). "InSAR permanent scatterer analysis reveals ups and downs in San Francisco Bay Area." **85**(34): 317-324. doi: 10.1029/2004eo340002.

Ferretti, A., C. Prati and F. Rocca (2000). "Nonlinear subsidence rate estimation using permanent scatterers in differential SAR interferometry." *Ieee Transactions on Geoscience and Remote Sensing* **38**(5): 2202-2212. doi: 10.1109/36.868878.

Ferretti, A., C. Prati and F. Rocca (2001). "Permanent scatterers in SAR interferometry." *Ieee Transactions on Geoscience and Remote Sensing* **39**(1): 8-20. doi: 10.1109/36.898661.

Goldstein, R. M., H. Engelhardt, B. Kamb and R. M. Frolich (1993). "SATELLITE RADAR INTERFEROMETRY FOR MONITORING ICE-SHEET MOTION - APPLICATION TO AN ANTARCTIC ICE STREAM." *Science* **262**(5139): 1525-1530. doi: 10.1126/science.262.5139.1525.

Hammond, W. C. and W. Thatcher (2005). "Northwest basin and range tectonic deformation observed with the global positioning system, 1999-2003." *Journal of Geophysical Research-Solid Earth* **110**(B10). doi: 10.1029/2005jb003678.

Hooper, A., D. Bekaert, K. Spaans and M. Arikan (2012). "Recent advances in SAR interferometry time series analysis for measuring crustal deformation." *Tectonophysics* **514**: 1-13. doi: 10.1016/j.tecto.2011.10.013.

Hooper, A., H. Zebker, P. Segall and B. Kampes (2004). "A new method for measuring deformation on volcanoes and other natural terrains using InSAR persistent scatterers." *Geophysical Research Letters* **31**(23). doi: 10.1029/2004gl021737.

Hsu, Y.-J., S.-B. Yu, L.-C. Kuo, Y.-C. Tsai and H.-Y. Chen (2011). "Coseismic deformation of the 2010 Jiashian, Taiwan earthquake and implications for fault activities in southwestern Taiwan." *Tectonophysics* **502**(3): 328-335. doi: https://doi.org/10.1016/j.tecto.2011.02.005.

75

Hsu, Y.-J., S.-B. Yu, M. Simons, L.-C. Kuo and H.-Y. Chen (2009). "Interseismic crustal deformation in the Taiwan plate boundary zone revealed by GPS observations, seismicity, and earthquake focal mechanisms." *Tectonophysics* **479**(1): 4-18. doi: https://doi.org/10.1016/j.tecto.2008.11.016.

Hu, J.-C., L.-W. Cheng, H.-Y. Chen, Y.-M. Wu, J.-C. Lee, Y.-G. Chen, K.-C. Lin, R.-J. Rau, H. Kuochen, H.-H. Chen, S.-B. Yu and J. Angelier (2007). "Coseismic deformation revealed by inversion of strong motion and GPS data: The 2003 Chengkung earthquake in eastern Taiwan." *Geophysical Journal International* **169**(2): 667-674. doi: 10.1111/j.1365-246X.2007.03359.x %J Geophysical Journal International.

Huang, M.-H., D. Dreger, R. Bürgmann, S.-H. Yoo and M. Hashimoto (2013). "Joint inversion of seismic and geodetic data for the source of the 2010 March 4, Mw 6.3 Jia-Shian, SW Taiwan, earthquake." *Geophysical Journal International* **193**(3): 1608-1626. doi: 10.1093/gji/ggt058 %J Geophysical Journal International.

Huang, M.-H., J.-C. Hu, C.-S. Hsieh, K.-E. Ching, R.-J. Rau, E. Pathier, B. Fruneau and B. Deffontaines (2006). "A growing structure near the deformation front in SW Taiwan as deduced from SAR interferometry and geodetic observation." *Geophysical Research Letters* **33**(12). doi: 10.1029/2005gl025613.

Huang, M.-H. and H.-H. Huang (2018). "The Complexity of the 2018 Mw 6.4 Hualien Earthquake in East Taiwan." **45**(24): 13,249-213,257. doi: 10.1029/2018gl080821.

Huang, M.-H., H. Tung, E. J. Fielding, H.-H. Huang, C. Liang, C. Huang and J.-C. Hu (2016). "Multiple fault slip triggered above the 2016 Mw 6.4 MeiNong earthquake in Taiwan." **43**(14): 7459-7467. doi: 10.1002/2016gl069351.

Huang, M. H., R. Burgmann and J. C. Hu (2016). "Fifteen years of surface deformation in Western Taiwan: Insight from SAR interferometry." *Tectonophysics* **692**: 252-264. doi: 10.1016/j.tecto.2016.02.021.

Hung, H.-K., R.-J. Rau, E. Benedetti, M. Branzanti, A. Mazzoni, G. Colosimo and M. Crespi (2017). "GPS Seismology for a moderate magnitude earthquake: Lessons learned from the analysis of the 31 October 2013 ML 6.4 Ruisui (Taiwan) earthquake." *2017* **60**(5). doi: 10.4401/ag-7399.

Hung, H. K. and R. J. Rau (2013). "Surface waves of the 2011 Tohoku earthquake: Observations of Taiwan's dense high-rate GPS network." *Journal of Geophysical Research-Solid Earth* **118**(1): 332-345. doi: 10.1029/2012jb009689.

Hung, W.-C., C. Hwang, C.-P. Chang, J.-Y. Yen, C.-H. Liu and W.-H. Yang (2010). "Monitoring severe aquifer-system compaction and land subsidence in Taiwan using multiple sensors: Yunlin, the southern Choushui River Alluvial Fan." *Environmental Earth Sciences* **59**(7): 1535-1548. doi: 10.1007/s12665-009-0139-9.

Kouba, J. and P. J. G. S. Héroux (2001). "Precise Point Positioning Using IGS Orbit and Clock Products." **5**(2): 12-28. doi: 10.1007/pl00012883.

Kuo, C. Y., K. W. Chiu, K. W. Chiang, K. C. Cheng, L. C. Lin, H. Z. Tseng, F. Y. Chu, W. H. Lan and H. T. Lin (2012). "High-Frequency Sea Level Variations Observed by GPS Buoys Using Precise Point Positioning Technique." *Terrestrial Atmospheric and Oceanic Sciences* **23**(2): 209-218. doi: 10.3319/TAO.2011.10.05.01(Oc).

Larson, K. M., P. Bodin and J. Gomberg (2003). "Using 1-Hz GPS data to measure deformations caused by the Denali fault earthquake." *Science* **300**(5624): 1421-1424. doi: 10.1126/science.1084531.

Lee, S. J., T. C. Lin, T. Y. Liu and T. P. Wong (2018). "Fault-to-Fault Jumping Rupture of the 2018 Mw 6.4 Hualien Earthquake in Eastern Taiwan." *Seismological Research Letters* **90**(1): 30-39. doi: 10.1785/0220180182 %J Seismological Research Letters.

Lin, K.-C., J.-C. Hu, K.-E. Ching, J. Angelier, R.-J. Rau, S.-B. Yu, C.-H. Tsai, T.-C. Shin and M.-H. Huang (2010). "GPS crustal deformation, strain rate, and seismic activity after the 1999 Chi-Chi earthquake in Taiwan." **115**(B7). doi: 10.1029/2009jb006417.

Lu, C. H., C. F. Ni, C. P. Chang, J. Y. Yen and W. C. Hung (2015). "Combination with precise leveling and PSInSAR observations to quantify pumping-induced land subsidence in central Taiwan." *Proc. IAHS* **372**: 77-82. doi: 10.5194/piahs-372-77-2015.

Massonnet, D., M. Rossi, C. Carmona, F. Adragna, G. Peltzer, K. Feigl and T. Rabaute (1993). "The displacement field of the Landers earthquake mapped by radar

interferometry." *Nature* **364**(6433): 138-142. doi: 10.1038/364138a0.

Matus Bakon, Daniele Perissin, Milan Lazecky and J. Papco (2014). "Infrastructure Non-linear Deformation Monitoring Via Satellite Radar Interferometry." *Procedia Technology* **16**: 294-300. doi: https://doi.org/10.1016/j.protcy.2014.10.095.

Melgar, D., B. W. Crowell, J. H. Geng, R. M. Allen, Y. Bock, S. Riquelme, E. M. Hill, M. Protti and A. Ganas (2015). "Earthquake magnitude calculation without saturation from the scaling of peak ground displacement." *Geophysical Research Letters* **42**(13): 5197-5205. doi: 10.1002/2015gl064278.

Min-Chien, T., Y. Shui-Beih, S. Tzay-Chyn, K. Kai-Wen, L. Peih-Lin, C. Chien-Hsin and H. Mei-Yi (2015). "Velocity Field Derived from Taiwan Continuous GPS Array (2007 - 2013)." *Terrestrial, Atmospheric & Oceanic Sciences* **26**(5): 527-556. doi: 10.3319/TAO.2015.05.21.01(T).

Nikolaidis, R. M., Y. Bock, P. J. de Jonge, P. Shearer, D. C. Agnew and M. Van Domselaar (2001). "Seismic wave observations with the Global Positioning System." **106**(B10): 21897-21916. doi: 10.1029/2001jb000329.

Ohta, Y., I. Meilano, T. Sagiya, F. Kimata and K. Hirahara (2006). "Large surface wave of the 2004 Sumatra-Andaman earthquake captured by the very long baseline kinematic analysis of 1-Hz GPS data." *Earth Planets and Space* **58**(2): 153-157. doi: 10.1186/bf03353372.

Pathier, E., B. Fruneau, B. Deffontaines, J. Angelier, C. P. Chang, S. B. Yu and C. T. Lee (2003). "Coseismic displacements of the footwall of the Chelungpu fault caused by the 1999, Taiwan, Chi-Chi earthquake from InSAR and GPS data." *Earth and Planetary Science Letters* **212**(1-2): 73-88. doi: 10.1016/s0012-821x(03)00244-9.

Peyret, M., S. Dominguez, R. Cattin, J. Champenois, M. Leroy and A. Zajac (2011). "Present-day interseismic surface deformation along the Longitudinal Valley, eastern Taiwan, from a PS-InSAR analysis of the ERS satellite archives." *Journal of Geophysical Research-Solid Earth* **116**. doi: 10.1029/2010jb007898.

Rivera, A. M. M., F. Amelung, P. Mothes, S. H. Hong, J. M. Nocquet and P. Jarrin (2017). "Ground deformation before the 2015 eruptions of Cotopaxi volcano detected

by InSAR." *Geophysical Research Letters* **44**(13): 6607-6615. doi: 10.1002/2017gl073720.
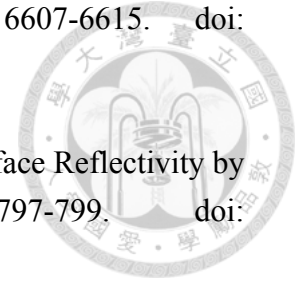
Rogers, A. E. E. and R. P. Ingalls (1969). "Venus: Mapping the Surface Reflectivity by Radar Interferometry." *Science* **165**(3895): 797-799. doi: 10.1126/science.165.3895.797 %J Science.

Rumsey, H. C., G. A. Morris, R. R. Green and R. M. Goldstein (1974). "A radar brightness and altitude image of a portion of Venus." *Icarus* **23**(1): 1-7. doi: 10.1016/0019-1035(74)90099-2.

Sanchez-Gamez, P. and F. J. Navarro (2017). "Glacier surface velocity retrieval using D-InSAR and offset tracking techniques applied to ascending and descending passes of Sentinel-1 data for southern Ellesmere ice caps, Canadian Arctic." *Remote Sensing* **9**(5). doi: 10.3390/rs9050442.

Sato, M., T. Ishikawa, N. Ujihara, S. Yoshida, M. Fujita, M. Mochizuki and A. Asada (2011). "Displacement Above the Hypocenter of the 2011 Tohoku-Oki Earthquake." *Science* **332**(6036): 1395-1395. doi: 10.1126/science.1207401.

Savage, J. C., W. Gan, W. H. Prescott and J. L. Svarc (2004). "Strain accumulation across the Coast Ranges at the latitude of San Francisco, 1994-2000." *Journal of Geophysical Research-Solid Earth* **109**(B3). doi: 10.1029/2003jb002612.

Squarzoni, C., C. Delacourt and P. Allemand (2003). "Nine years of spatial and temporal evolution of the La Valette landslide observed by SAR interferometry." *Engineering Geology* **68**(1): 53-66. doi: https://doi.org/10.1016/S0013-7952(02)00198-9.

Tsukahara, K. and Y. Takada (2018). "Aseismic fold growth in southwestern Taiwan detected by InSAR and GNSS." *Earth Planets and Space* **70**. doi: 10.1186/s40623-018-0816-6.

Tung, H., H. Y. Chen, J. C. Hu, K. E. Ching, H. Chen and K. H. Yang (2016). "Transient deformation induced by groundwater change in Taipei metropolitan area revealed by high resolution X-band SAR interferometry." *Tectonophysics* **692**: 265-277. doi: 10.1016/j.tecto.2016.03.030.

Tung, H. and J. C. Hu (2012). "Assessments of serious anthropogenic land subsidence in Yunlin County of central Taiwan from 1996 to 1999 by Persistent Scatterers InSAR." *Tectonophysics* **578**: 126-135. doi: 10.1016/j.tecto.2012.08.009.

Wen, S., Y. L. Yeh, Y. Z. Chang and C. H. Chen (2017). "The seismogenic process of the 2016 Meinong earthquake, southwest Taiwan." *Terrestrial Atmospheric and Oceanic Sciences* **28**(5): 651-662. doi: 10.3319/tao.2017.02.17.01.

Wright, T. J., B. Parsons, P. C. England and E. J. Fielding (2004). "InSAR observations of low slip rates on the major faults of western Tibet." *Science* **305**(5681): 236-239. doi: 10.1126/science.1096388.

Yang, Y. H., J. C. Hu, H. Tung, M. C. Tsai, Q. Chen, Q. Xu, Y. J. Zhang, J. J. Zhao, G. X. Liu, J. N. Xiong, J. Y. Wang, B. Yu, C. Y. Chiu and Z. Su (2018). "Co-Seismic and Postseismic Fault Models of the 2018 Mw 6.4 Hualien Earthquake Occurred in the Junction of Collision and Subduction Boundaries Offshore Eastern Taiwan." *Remote Sensing* **10**(9). doi: 10.3390/rs10091372.

Yang, Y. H., J. C. Hu, A. Yassaghi, M. C. Tsai, M. Zare, Z. G. Wang, F. Kamranzad, Q. Chen and A. M. Rajabi (2018). "Midcrustal Thrusting and Vertical Deformation Partitioning Constraint by 2017 Mw 7.3 Sarpol Zahab Earthquake in Zagros Mountain Belt, Iran." *Seismological Research Letters* **89**(6): 2204-2213. doi: 10.1785/0220180022 %J Seismological Research Letters.

Yen, J.-Y., K.-S. Chen, C.-P. Chang and W.-M. Boemer (2008). "Evaluation of earthquake potential and surface deformation by Differential Interferometry." *Remote Sensing of Environment* **112**(3): 782-795. doi: 10.1016/j.rse.2007.06.012.

Yu, S.-B., Y.-J. Hsu, L.-C. Kuo, H.-Y. Chen and C.-C. Liu (2003). "GPS measurement of postseismic deformation following the 1999 Chi-Chi, Taiwan, earthquake." **108**(B11). doi: 10.1029/2003jb002396.

Yu, S. B., H. Y. Chen and L. C. Kuo (1997). "Velocity field of GPS stations in the Taiwan area." *Tectonophysics* **274**(1-3): 41-59. doi: 10.1016/s0040-1951(96)00297-1.

Yu, S. B. and L. C. Kuo (2001). "Present-day crustal motion along the Longitudinal Valley Fault, eastern Taiwan." *Tectonophysics* **333**(1-2): 199-217. doi:

10.1016/s0040-1951(00)00275-4.

Yue, H. and T. Lay (2011). "Inversion of high-rate (1 sps) GPS data for rupture process of the 11 March 2011 Tohoku earthquake (Mw 9.1)." **38**(7). doi: 10.1029/2011gl048700.
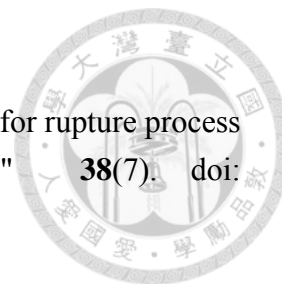
Zebker, H. A. and R. M. Goldstein (1986). "Topographic mapping from interferometric synthetic aperture radar observations." *Journal of Geophysical Research-Solid Earth and Planets* **91**(B5): 4993-4999. doi: 10.1029/JB091iB05p04993.

Zebker, H. A., S. Hensley, P. Shanker and C. Wortham (2010). "Geodetically Accurate InSAR Data Processor." *Ieee Transactions on Geoscience and Remote Sensing* **48**(12): 4309-4321. doi: 10.1109/tgrs.2010.2051333.

Zisk, S. H. (1972). "Lunar Topography: First Radar-Interferometer Measurements of the Alphonsus-Ptolemaeus-Arzachel Region." *Science* **178**(4064): 977-980. doi: 10.1126/science.178.4064.977.

Zumberge, J. F., M. B. Heflin, D. C. Jefferson, M. M. Watkins and F. H. Webb (1997). "Precise point positioning for the efficient and robust analysis of GPS data from large networks." *Journal of Geophysical Research-Solid Earth* **102**(B3): 5005-5017. doi: 10.1029/96jb03860.

Appendix I

Transient deformation induced by groundwater change in Taipei metropolitan area revealed by high resolution X-bandSAR interferometry

Transient deformation induced by groundwater change in Taipei metropolitan area revealed by high resolution X-band SAR interferometry

Hsin Tung [a], Horng-Yue Chen [b], Jyr-Ching Hu [a,*], Kuo-En Ching [c], Hongey Chen [a], Kuo-Hsin Yang [d]

[a] Department of Geosciences, National Taiwan University, No. 1, Sec. 4, Roosevelt Road, Taipei 10671, Taiwan
[b] Institute of Earth Sciences, Academia Sinica, 128 Academia Road, Section 2, Nankang, Taipei 11529, Taiwan
[c] Department of Geomatics, National Cheng Kung University, No. 1, University Road, Tainan City 701, Taiwan
[d] Department of Civil and Construction Engineering, National Taiwan University of Science and Technology, Taipei 10607, Taiwan

ARTICLE INFO

ABSTRACT

We present precise deformation velocity maps for the two year period from September 2011 to July 2013 of the northern Taiwan area, Taipei, by using persistent scatterer interferometry (PSI) technique for processing 18 high resolution X-band synthetic aperture radar (SAR) images archived from COSMO-SkyMed (CSK) constellation. According to the result, the highest subsidence rates are found in Luzou and Wuku area in which the rate is about 15 mm/yr and 10 mm/yr respectively in the whole dataset. However, dramatic change from serve subsidence to uplift in surface deformation was revealed in the Taipei Basin in two different time spans: 2011/09–2012/09 and 2012/09–2013/07. This result shows good agreement with robust continuous GPS measurement and precise leveling survey data across the central Taipei Basin. Moreover, it also represents high correlation with groundwater table. From 8 well data in the Taipei basin, the storativity is roughly constant across most of the aquifer with values between 0.5×10^{-4} and 1.6×10^{-3} in Jingmei Formation and 0.8×10^{-4} and 1.4×10^{-3} in Wuku Formation. This high correlation indicated that one meter groundwater level change could induce about 9 and 16 mm surface deformation change in Luzou and Wuku area respectively, which is about eight times faster the long-term tectonic deformation rate in this area. Thus, to access the activity of the Shanchiao Fault, it is important to discriminate tectonic movement from anthropogenic or seasonal effect in the Taipei Basin to better understand the geohazards and mitigation in the Taipei metropolitan area.

© 2016 Elsevier B.V. All rights reserved.

1. Introduction

Severe land subsidence has been studied in urban areas worldwide with consequences of the exhaustion of groundwater resources, increase of risks of in flooding and damage of infrastructures and buildings (e.g. Abidin et al., 2001; Teatini et al., 2005; Konikow and Kendy, 2005; Galloway and Hoffmann, 2007; Phien-wej et al., 2006; Hu et al., 2006; Chen et al., 2007; Lai et al., 2010; Chaussard et al., 2013, 2014). Based on the recent studies, over pumping of ground water could lead to rapid subsidence at rates of up to several tens of centimeters per year. (e.g., Bell et al., 2008; Tung and Hu, 2012; Chaussard et al., 2013, 2014). Pumping-induced subsidence is primarily due to irreversible compaction of aquitard material composed of fine-grained silt and clay layers, and from minor amount of presumably elastic compaction from compression of coarse-grained conglomerate and sand deposits

in aquifers (Holzer, 1984; Wilson and Gorelick, 1996; Waltham, 2002). Consequently, the elevation changes are proportional to variations of the thickness of the compaction layer and hydraulic head (Wilson and Gorelick, 1996). Thus ground elevation change due to pumping generally reflects the response to piezometric level drop. On the other hand, small amounts of land uplift might occur due to the groundwater recovery from aquifer recharged after long-term massive groundwater extraction (Amelung et al., 1999; Lu and Danskin, 2001; Schmidt and Bürgmann, 2003; Chen et al., 2007). This effect is considered to be originating from relaxation of elastically compressed aquifer materials when pore-pressure regained (Allen and Mayuga, 1969; Waltham, 2002).

In Taiwan, groundwater has been abundantly used as an alternative to surface water in urban area and in the southwestern coastal region where the deficiency of surface water resources was severe due to the high water demand from aquacultural and industrial utilization in Taiwan. Anthropogenic ground subsidence induced by heavy withdrawal of groundwater has been monitored by precise leveling, GPS measurement and SAR interferometry (e.g., Hou et al., 2005; Hwang et al., 2008; Hsieh et al., 2011; Hung et al., 2010, 2011; Wang et al.,

2011; Tung and Hu, 2012). In addition, based on the fifteen years of PSInSAR-derived surface deformation in western Taiwan, Huang et al. (2016) suggested that the seasonal displacement is mainly associated with groundwater recharge and withdrawal.

Taipei City is the political and economic centre of Taiwan (Fig. 1a) with a dense population of about 3 million. Massive groundwater pumping resulted in both dry-ups of wells and severe land subsidence during 1955–1970 (Wu, 1987). Groundwater table was gradually recovered and became approximately stable since late 1990s after a stop on the use of groundwater during the early 1970s (Chia et al., 1999). According to recent study, Chen et al. (2007) proposed that the overall subsidence rate due to the summation of shallow soil compaction, deformation within aquifer, and tectonic subsidence within the Taipei Basin gradually decreased since 1975, and around 1989 the basin switched to slight uplift throughout a large part of the basin based on the contour maps created from the leveling data of 406 benchmarks. The shallow components of soil compaction were estimated in a range of 2–3.5 mm/yr in Wuku and central Taipei Basin. Meanwhile the deep component from tectonic load was estimated in a range of 0.9–1.8 mm/yr. Furthermore, while severe anthropogenic land subsidence has been stopped in the Taipei metropolitan area, concerns on potential earthquakes associated with possible reactivation of the active Shanchiao Fault (Fig. 1b) is a crucial topic for assessment of geohazards in Taipei metropolitan area (Teng et al., 2001; Huang et al., 2007; Shyu et al., 2005).

The previous GPS network from campaign-mode survey, the GPS velocity in the Taipei Basin was insignificant in comparison with western Foothill in south-central Taiwan (Yu et al., 1997). Based on these data, Hu et al. (2002) calculate the strain rate in Taipei area, where the subnetworks NT1–NT4 have shown small extension rates (0.07–0.15 μstrain/year) and small contraction rates (0.03–0.09 μstrain/year). In addition,

the extension deformations in these networks mostly trend east–west to east-northeast (Hu et al., 2002). For the period 1995–2005, 125 campaign-surveyed GPS sites in northern Taiwan had been calculated for accommodation in deformation from collision to subduction (Rau et al., 2008). These results suggested that across Chinshan–Shanchiao Faults, GPS vectors showed a slight clockwise rotation of 30° (from 303° to 332°) with magnitudes of 1.3–4.3 mm/yr from west to east.

Radar interferometry technique has proven to be capable of measuring surface displacement at fine space resolution of tens of meters over wide coverage (e.g., Massonnet and Feigl, 1998; Bürgmann et al., 2000; Pritchard and Simons, 2002; Wright, 2002). However, temporal and spatial decorrelations of radar signal have prevented this technique from more frequent utilization. Besides, the accuracy of InSAR measurements may be largely reduced by atmospheric phase artifacts that are difficult to be removed from SAR interferograms (e.g., Buckley et al., 2003; Ding et al., 2004). Consequently persistent scatterer (PS) technique has been proposed to improve the applicability of radar interferometry when applied to detect long-term ground deformation with tracking the signals of discrete point-wise targets (Ferretti et al., 2000, 2001; Berardino et al., 2002; Mora et al., 2003; Hooper et al., 2004; Kampes and Hanssen, 2004; Liu et al., 2008). According to previous studies, a surface deformation map of northern Taiwan using SAR interferometry technique from 1993 to 2005 has been shown by Chang et al. (2010). They suggested that the significant subsidence occurred at the border of the Taipei Basin and a relatively slight uplift rebound in the central basin, and displacements along the Shanchiao, Chinshan, and Kanchiao Faults are large enough to be observed. However, part of surface deformation from SAR interferometry should be related to the groundwater recharge and withdrawal (Huang et al., 2016). In this paper, we use the high resolution X-band SAR images from COSMO-SkyMed (CSK) constellation with the constraints of leveling and
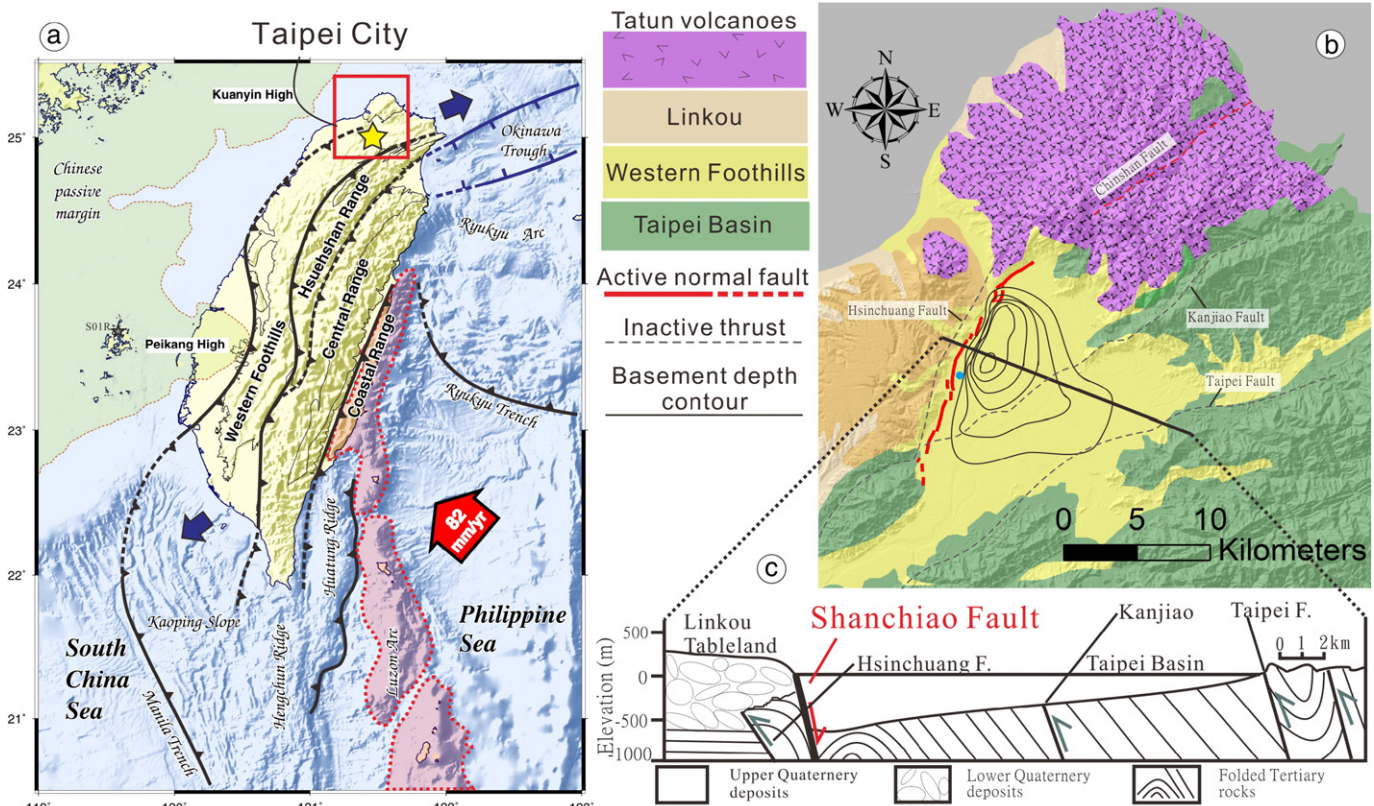
Fig. 1. (a) Tectonic framework of Taiwan. (b) Geological domains of Taipei region. The thin black lines within Taipei Basin indicate the basement depth contour of 100 m interval. (c) Geological cross section of the Taipei Basin (modified from Chen et al., 2007). Blue dot is the location for stratigraphic architecture of late Quaternary deposits in Fig. 2.

continuous GPS data to monitor surface deformation in the Taipei area and characterize the transient surface deformation due to the groundwater recharge and withdrawal.

2. Geological setting and data

2.1. Geological and hydrological background

From the tectonic viewpoint, Taiwan Island is situated at the plate suture of Eurasian and Philippine Sea plate since 5 Ma (e.g., Suppe, 1981; Teng, 1990). According to GPS results, the convergence rate is about 82 mm/yr in the NW direction (Yu et al., 1997; Lin et al., 2010). At present, the collision process is manifested in southern and central Taiwan as demonstrated by the intense crustal shortening and frequent seismicity. In contrast, north-eastern Taiwan underwent post-collisional processes and has been considered to be incorporated in the opening of the southern Ryukyu back-arc system (Teng et al., 2000). Opening of Okinawa Trough and the retreat of Ryukyu trench together with the ongoing collision process in north-western Taiwan results in transtensional and extensional regimes (Hu et al., 1996, 2001, 2002), as revealed by the presence of Quaternary extensional structures (Lee and Wang, 1988; Lu et al., 1995), extensional earthquake focal mechanisms (Kao et al., 1998) and GPS measurement (Yu et al., 1999; Hu et al., 2002; Rau et al., 2008). The Taipei Basin is located at the northern part of Taiwan, surrounded by Tatun Volcano group to the north, the Linku Tableland to the west, and the northwest hills of western Foothills and Hsüehshan Range to the southeast (Fig. 1a and b). The active Shanchiao Fault bounding the western edge of the Taipei Basin is an east-dipping normal fault with a dip angle of about 60°. The average late-Quaternary long-term tectonic subsidence rate was estimated by stratigraphic offset across the fault to be 1.75 mm/yr since 0.4 Ma. This active fault is, and should have an influence on the elevation change in the western Taipei Basin (Chen et al., 2007).

The seismicity in the Taipei Basin is lower than the other area of northern Taiwan (e.g. Kim et al., 2005; Wang et al., 2006; Konstantinou et al., 2007). In addition, with the lock of cluster seismicity and seismic profile in the Taipei Basin, it is difficult to correlate the seismicity with recognized faults. At least there Holocene paleoseismic events with a slip of 1–3 m were proposed at ~8500, ~9200, and ~11,100 years B.P. from analysis of basin sediments retrieved from shallow boreholes in the Taipei Basin (Huang et al., 2007). The dense broadband seismic array was deployed to monitor seismicity in the Taipei Basin since June 2004 (Chen et al., 2010b). During the period of observation, three felt earthquakes ($M_L = 3.8, 3.2$, and 3.7) of normal faulting happened near the eastern part of the basin. The focal depth of ~9 km was proposed to be related to a blind fault under the Taipei Basin (Chen et al., 2010b) and was triggered by the loading of famous Taipei 101 building (Lin, 2005). Recently Chen et al. (2014) interpreted that three felt earthquakes are located in the junction of the shallow border of the lower fault ramp and inverted thrust detachment of active Shanchiao Fault.

The Taipei Basin has been a dammed lake associated with the last eruption of Tatun volcanism which blocked the effluence of the Tanshui River at about 0.2 Ma (Song et al., 2000). After that, global climate change brought marine transgression and made this place to an estuarine deposition at around 6 Ka. According to the deep drill data, the triangular-shaped Taipei Basin is considered as a half-graben filled with deformed Tertiary strata and filled with upper Pleistocene and Holocene sediment since about 0.4 Ma (Wei et al., 1998; Teng et al., 2001), and the deepest basement is close to the active Shanchiao Fault with depth more than 670 m (Fig. 1b). The stratigraphic section cutting through the central Taipei Basin shows that the basin sediment, dominated by gravel, sand, mud and their interbred is formed by late-Quaternary fluvial formation laying on the top of the Miocene sedimentary bedrock. These unconsolidated deposits can be divided into four lithostratigraphic units with two basin-wide marker beds, Jingmei gravel and Banqiao lake mud (Fig. 2). From top to bottom: (1) the Sungshan
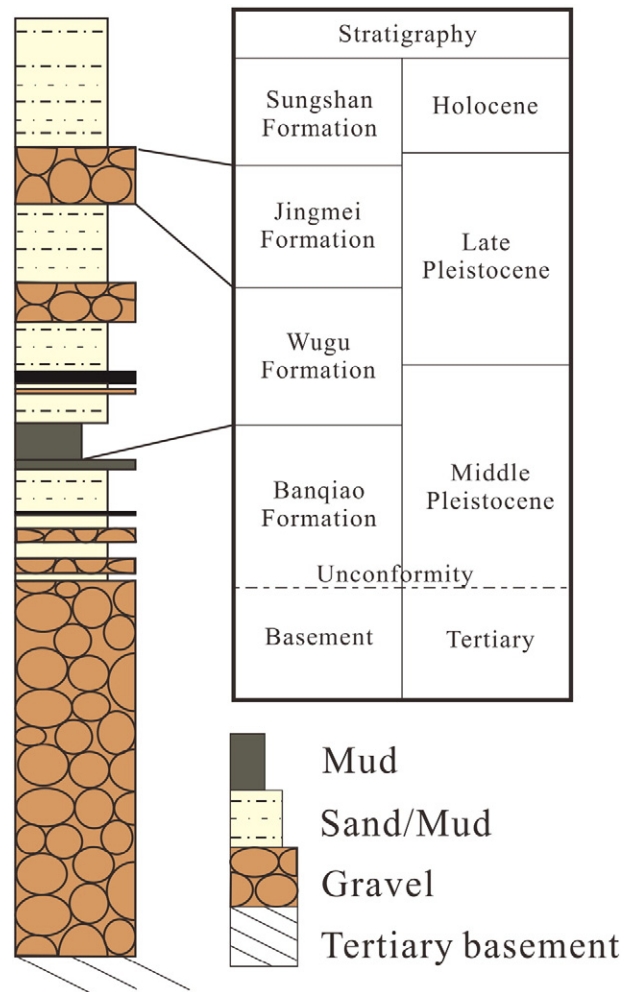
Fig. 2. Stratigraphic architecture of late Quaternary deposits within Taipei Basin (modified from Teng et al., 1999). Location see Fig. 1b (blue dot).

formation, composed of estuary interbedded with sand and mud deposits, is an unconfined aquifer with three aquifers and three aquitards; (2) the Jingmei formation, formed by lateritic alluvial-fan conglomerates is the main aquifer of the Taipei Basin with hydraulic diffusivity around 0.12 to 0.18 m²/s and storage coefficient ranging from 0.001 to 0.004 (Chia et al., 1999); (3) the Wuku formation, consisted of fluvial sand and conglomerates with minor mud and lateritic conglomerates; (4) the Banqiao formation, comprised of fluvial sand, mud and conglomerates, with minor pyroclastic debris and thick mud in the upper section (Teng et al., 1999).

Since the 1950s, serious land subsidence occurred from the extensive pumping from the aquifer in the Taipei Basin due to the demand of accumulated populations. The groundwater level has declined approximately 50 m before 1976 and followed by a rapid recovery starting from the late 1970s. Following up, according to the recent study analyzed from leveling data, Chen et al. (2007) proposed that the post-pumping phenomena indicated the subsidence rate for the Taipei Basin as a whole generally decreased trend from 40–70 mm/yr to 0–30 mm/yr during 1975 to 1989, and then the elevation change of the basin gradually switched to a slight uplift from 10 to 15 mm/yr in central Taipei and Banqiao since about 1989.

2.2. Continuous GPS and precise leveling data

Totally 14 continuous GPS station are calculated for velocity field in study area with respect to continuous WUKU GPS station, which is
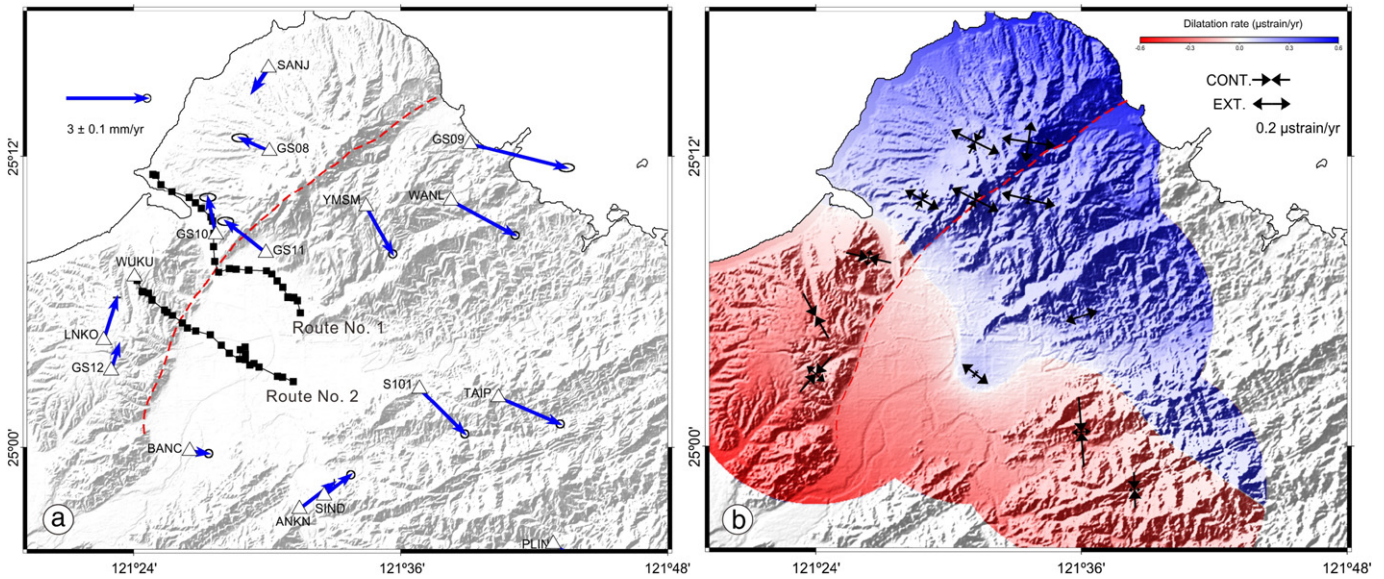
Fig. 3. (a) Continuous GPS velocity field with respect to WUKU located in stable Linko tableland. Red line represents the Shanchiao and Chinshan Faults. Black squares represent the benchmarks of two precise leveling routes. (b) Horizontal principal strain rate and dilatation rate based on continuous GPS data.

located at relative stable Linko tableland on the western Taipei Basin from 2006 to 2015. The GPS velocity ranges from 0.7 mm/yr to 3.7 mm/yr (Fig. 3). From viewpoint of deformation rate, two deformation regimes are observed; a contractional regime in southern part of the Shanchiao Fault and an extensional regime in northern part of the study area. The maximum NW–SE contractional principal strain rate that is about
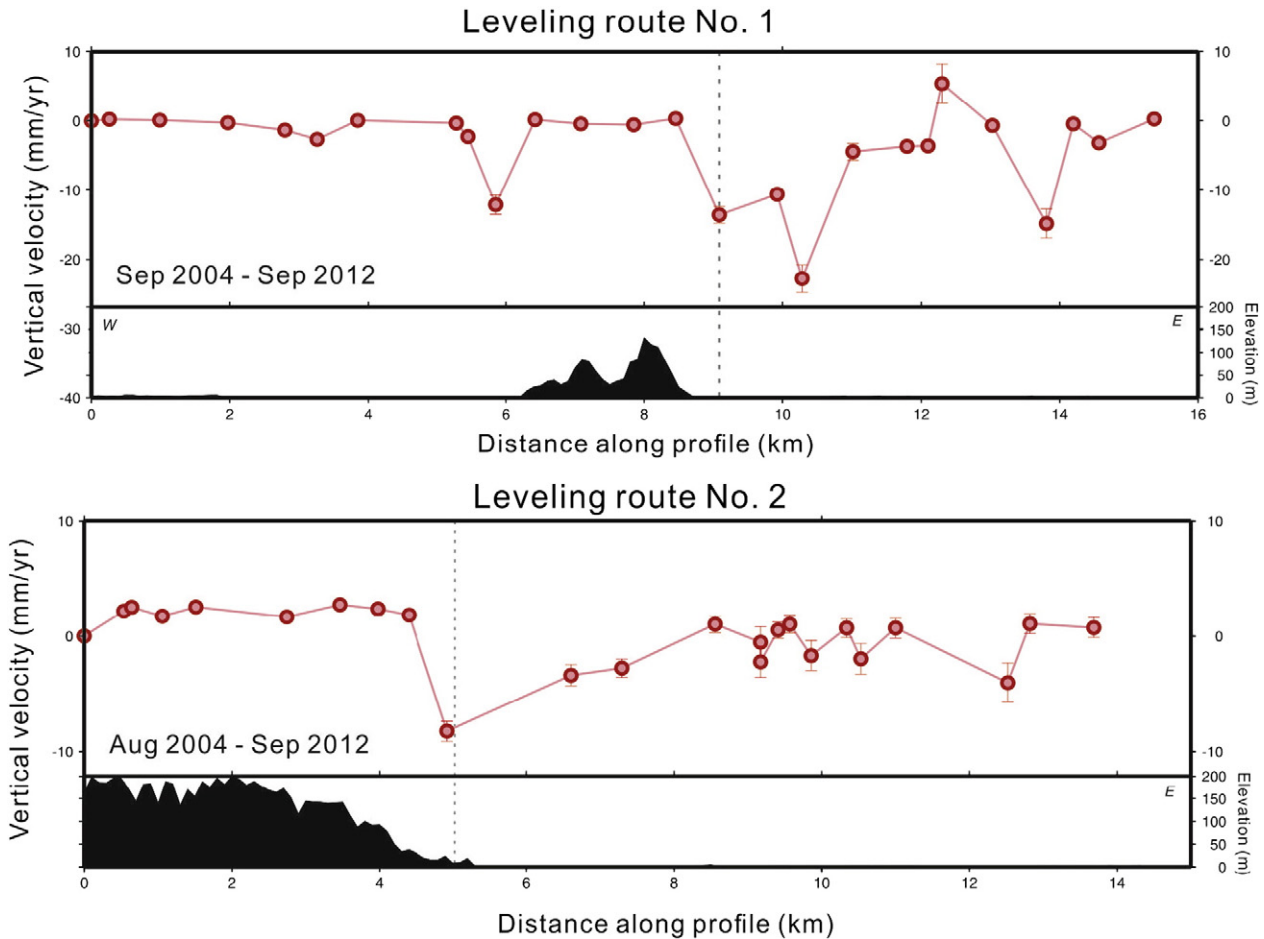
Fig. 4. Vertical velocity profile of two precise leveling routes across the Shanchiao Fault in north (No. 1) and central Taipei area (No. 2). Location of leveling routes is shown in Fig. 3. Red dots represent the vertical velocity and gray dotted line represent the location of the Shanchiao Fault.

0.37 μstrian/yr occurred in the footwall of the Shanchaio fault. The WNW–ESE extensional principal strain rate of about 0.28 μstrian/yr occurred near the Tatung Volcano.

Two precise leveling routes across the Shanchiao Fault are deployed by Central Geological Survey for monitoring the ground deformation. The westernmost benchmark of leveling route is used for reference point (Fig. 4). In general, both leveling routes show no significant elevation change in the footwall of the Shanchiao Fault, except one benchmark on leveling route No. 1 showing a local subsidence rate of 10 mm/yr. Near the Shanchiao Fault, two leveling routes show similar trends of increasing of land subsidence rate. In addition, the subsidence rate mostly decreases westward to central Taipei Basin. The maximum land subsidence rate is about 20 mm/yr and 10 mm/yr observed in routes No. 1 and No. 2, respectively from September 2004 to September 2012.

2.3. Methodology and SAR data acquisition

Interferometric synthetic aperture radar (InSAR) technique has been applied widely in surface displacement measurements since the first coseismic displacement pattern of Landers earthquake published on the cover of Nature (Massonnet et al., 1993). Its advantages of fast and wide cover observations provide an effective tool in geodetic survey (e.g., Massonnet and Feigl, 1998; Bürgmann et al., 2000). An advanced InSAR technique that traces movements of pixels in a bunch of radar images called persistent scatterer SAR interferometry (PSInSAR) technique has been proposed to improve the applicability of image analysis. This technique overcomes the limitations of temporal and atmospheric bias in conventional InSAR technique by computing only on sparsely distributed persistent scatterers (PSs). Through this process, the signals which cannot be obtained from conventional InSAR technique will be retrieved and the accuracy of displacement rate measurements increases from cm to mm scale.

The PSInSAR technique is an advanced technique in comparison with conventional InSAR technique, which addresses the problems of decorrelation for generating a time series of phase changes without atmospheric and DEM residuals effects by computing only on sparsely distributed PSs which are pixels coherent over long time series. This technique has been developed in the late 1990s by A. Ferretti, F. Rocca, and C. Prati of the Technical University of Milan (POLIMI). The first algorithm to find out the PS pixels was brought (Ferretti et al., 2000), and trademarked it as the "Permanent Scatterer technique". After that, similar processing algorithms have since been developed by Crosetto et al. (2003), and Mora et al. (2003). Besides, the Small Baseline subset technique developed by Berardino et al. (2002) and StaMPS (Stanford Method for Persistent Scatterers) developed by Hooper et al. (2004) are also the same idea of the PSInSAR technique with different names. The application of PSInSAR technique in the study of active faults and land subsidence in Taiwan has proven to be capable of measuring ground deformation at fine space resolution over wide coverage (Chang et al., 2010; Peyret et al., 2011; Champenois et al., 2012; Tung and Hu, 2012; Wu et al., 2013)

The stripmap mode of CSK SAR images provides spatial resolution of 3 m × 3 m, which is one order of magnitude better than the previous available satellite SAR data. The higher resolution leads to an increase of the density of the measurable targets relatively to those retrieved from medium resolution datasets (C- and L-band). On the other hand, the sensitivity of displacements is increased with shorter wavelengths (~3 cm), which enhance the capability of detecting very slow displacements rates. Furthermore, the more frequent revisit of the same Area of Interest (AOI) of the present X-band missions provides massive datasets to avoid the baseline limitation and temporal decorrelation, which improve the temporal resolution of deformation in time series.

Totally 18 ascending COSMO_Skymed constellation (Constellation of Small Satellites for Mediterranean basin observation) images were used for processing interferograms from September 2011 to July 2013. Most

of the interferograms have an absolute normal baselines smaller than 500 m (Fig. 5). Raw radar images were focused using ROI_PAC software developed by the JPL/Caltech; Interferograms were formed using Doris software (Kampes and Usai, 1999). The PSI was processed with StaMPS/MTI (Stanford Method for Persistent Scatterers/Multi Temporal InSAR). The topography phase component was removed by using SRTM DEM (3 arcsec in resolution) during interferogram processing. The details of images' information are shown in Fig. 5.

3. Result and analysis

In this study, 18 radar images were used to form 17 PSI interferograms. The Taipei Basin is a metropolis with dense artificial structure, giving a good condition for processing PSs. Within the 750 km² of the study area, roughly 1035,000 stable targets were available (Fig. 6). The density is 1380 points/km², which is almost 1000 times denser than other geodesy survey like leveling and GPS.

Continuous GPS data calculated by using GIPSY/OASIS software to estimate the precise coordinates and 3D-velocities and then convert the direction of motion to radar LOS (line-of-sight) component with incident angle of 23° (Fig. 6). In order to understand the deformation pattern in and around the Taipei Basin, the null-reference PS velocity is set in the vicinity of the continuous WUKU GPS station, which is located at relative stable Linko tableland on the western Taipei Basin illustrated in Fig. 6. After referencing to a relative stable WUKU station, the contribution of deformation in the horizontal direction is reduced. Then the 3D velocity filed of the six continuous GPS stations (LNKO, BANC, GS10, GS11, GS12 and S101) is projected to LOS to compare with the average LOS rate from the PSInSAR. The color shown in triangle is the LOS rate projected from GPS velocity and that in circle is the LOS rate from PSInSAR. The comparison of these two LOS rates are in good agreement.

The most significant signal is slight subsidence on the Luzhou and Wuku area with LOS deformation rate away from satellite 10 mm/yr and 5 mm/yr respectively. The subsidence areas are located close to the Shanchiao Fault. Another conspicuous pattern can be observed on the Beitou spring area, the LOS velocity rate of 10–15 mm/yr, indicating an active uplift occurred in this area. Unfortunately, no geodetic measurements and continuous GPS station were deployed in this area, thus we can't characterize the implication of this uplift so far. Only two continuous GPS stations (GS10 and GS11) showing inconsistent LOS deformation rate with that from PSInSAR, this inconsistence might be attributed by phase unwrapping error due to cross the river. Most of the PS points show consistent deformation rate with continuous
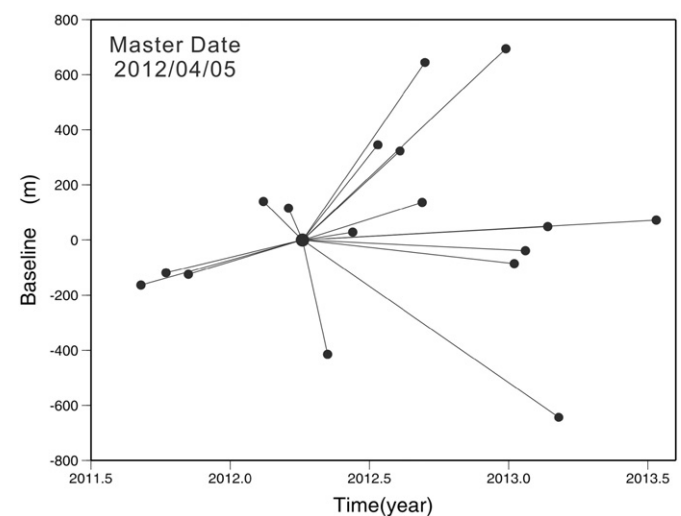
Fig. 5. Radar images and baseline information used in this study. Vertical axes are perpendicular baselines of image pairs relative to the master image on 5 April 2012; horizontal axes are acquisition dates of radar images.
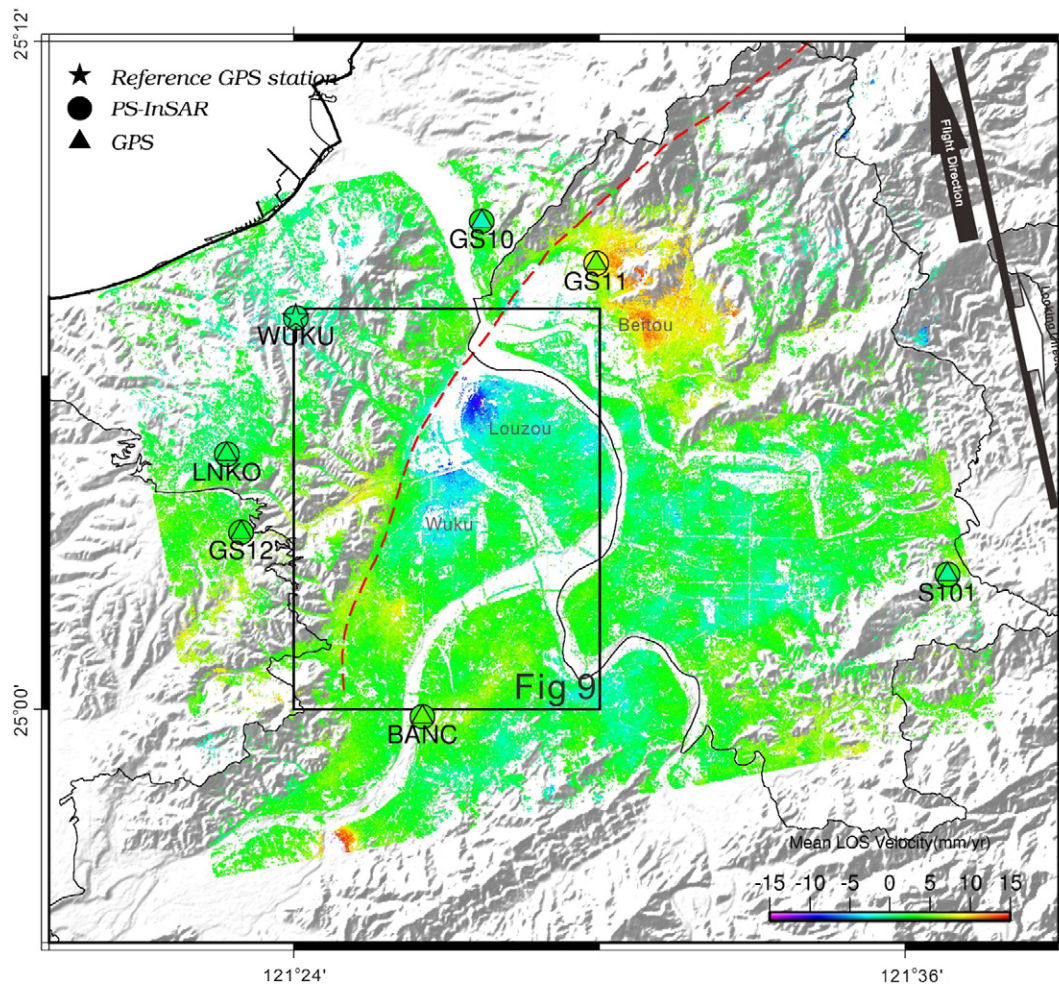
Fig. 6. Slant range displacement rate of the processed PSs in the northern Taiwan area overlapped on the hill-shaded background. Shortening in slant range (rate in positive with warm colors) represents land uplift and elongation (rate in negative with cold colors) represents land subsidence in slant range direction. Red dashed lines mark the active Shanchiao Fault (Lin et al., 2000). Colored triangles represent transferred GPS velocity from 3D to LOS direction and colored circles represent average velocities of PS points within 100 m of the GPS station in LOS direction. Rectangle is the location of Fig. 9.

GPS stations, the velocity differences between average PSs and continuous GPS station are less than 4 mm/yr. The good agreement indicates the reliability of our PSInSAR result.

Different deformation patterns have been revealed from previous studies by using precise leveling and C-band SAR data analysis (e.g., Chen et al., 2007; Chang et al., 2010). The deformation within the Taipei Basin varied from severe subsides to light uplift during 1975 and 2003 (Chen et al., 2007). Based on the study of PSInSAR and precise leveling, relatively subsidence in the Taipei Basin were observed from 2004 to 2007 (Chang et al., 2010). It is interesting to note that the dramatic changes of surface deformation in study area are observed whenever the whole dataset was separated into two sub-datasets to fit the survey period of precise leveling from 2011/9–2012/9 and 2012/9–2013/7 (Figs. 7 and 8). LOS rate from PSInSAR demonstrates that the significant land subsidence occurred in the hanging wall of the Shanchiao Fault related to the continuous GPS station WUKU located on the footwall of the fault in the period of 2011/9–2012/9 (Fig. 7a). The relatively maximum LOS rate can be up to about 5.5 cm/yr in the Taipei Basin. A good consistence shows between LOS rates of PSInSAR and the projection of 3D components of 6 continuous GPS (Fig. 7a). Independent precise leveling carried out in the same period also the similar trends on both hanging wall and footwall of the Shanchiao Fault (Fig. 7b). The maximum subsidence rate related to WUKU station is about 3 cm/yr located on the hanging wall of the Shanchiao Fault.

Surprisingly the deformation patterns on the hanging wall of the Shanchiao Fault switch to trend of uplifting related to WUKU station in the period of 2012/9–2013/7 (Fig. 8a). The relatively maximum LOS rate can be up to about 5 cm/yr in the Taipei Basin. The comparison of LOS rates from PSInSAR and projected continuous GPS rate is in good accordance. Independent precise leveling carried out in the same period also the similar trends on both hanging wall and footwall of the Shanchiao Fault (Fig. 8b). The maximum uplift rate is about 3 cm/yr related to WUKU station. The difference of LOS rate from PSInSAR and uplift rate from precise leveling are resulted from the time period inconsistent between leveling survey (~1 year) and SAR acquisitions (~10 months). We will discuss this change of deformation pattern of two periods in Discussion.

4. Discussion

4.1. Characterizing Shanchiao Fault trace form PSInSAR velocity field

High erosion rate in Taiwan and the cover of alluvium deposits make it difficult to find the active fault trace buried under the ground. Previous study of topographic mapping from LiDAR-derived DEM and real-time kinematics GPS survey had characterized the geomorphology of Shanchiao Fault zone revealed by a series of fault-related scarps arranged in an *en échelon* array (Chen et al., 2006). However the surface
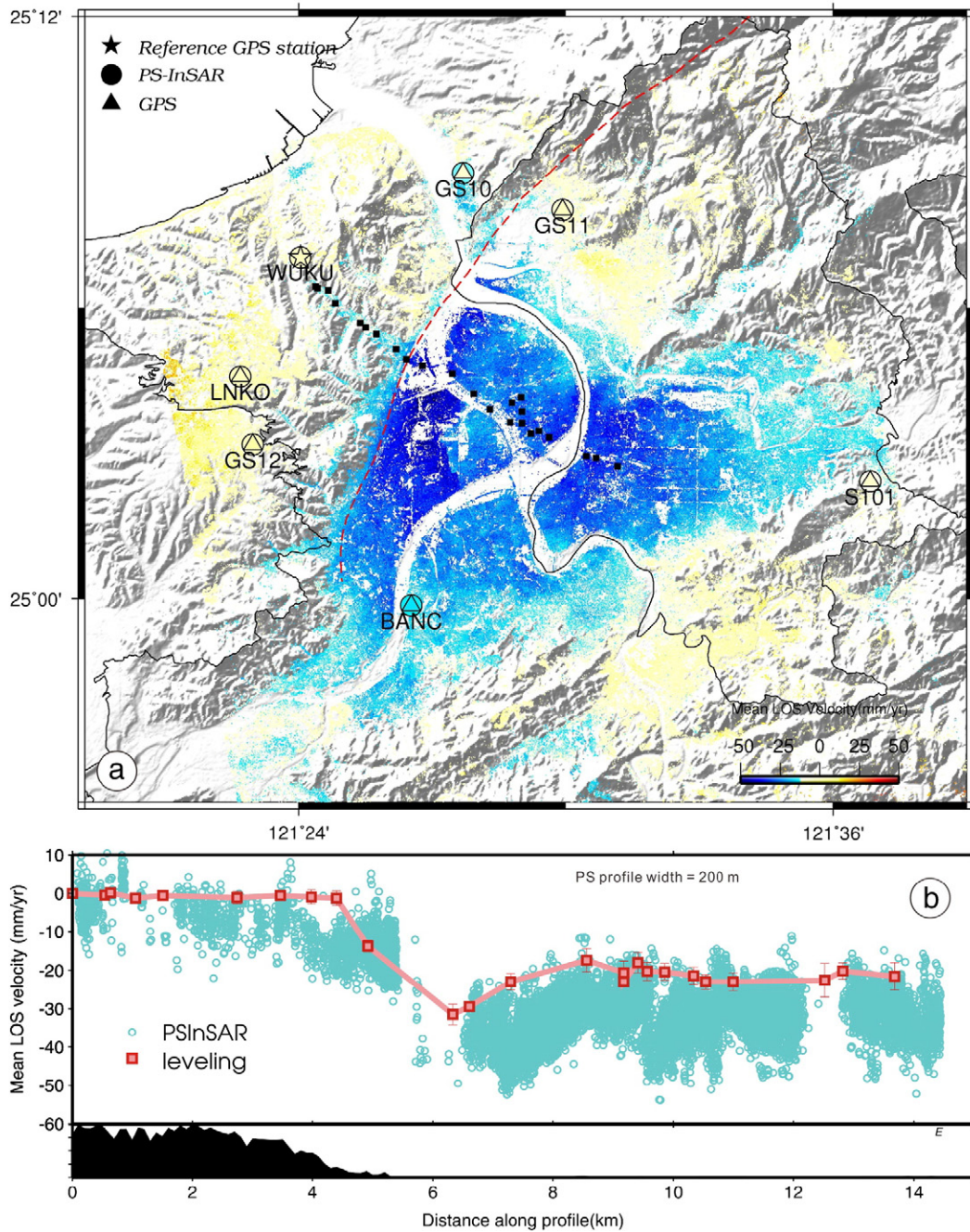
Fig. 7. (a) Slant range displacement rate of time span 2011/9–2012/9. (b) Comparison between the leveling data and PSInSAR result along the central of the Taipei Basin. Black rectangles are the locations of benchmarks in leveling route. Both PS and leveling data are relatively to the westernmost benchmark (WUKU) of the profile.

trace of the main fault seems to be completely erased by the surface force of erosion and sedimentation, only the subtle geomorphic scarps corresponding to the branch fault can be identified based on the correlation between geomorphology and subsurface geology in the Shanchiao Fault zone (Chen et al., 2010a).

In order to represent the various characters of the Shanchiao Fault, four velocity profiles sub-perpendicular to the Shanchiao fault from north to south contain PS points within 50 m have been shown in Fig. 9. The results show a significant velocity drop across the fault in profile 1; the velocity gradient is up to 5 mm/yr. In profile 2, the velocity gradient across the fault decreases to 3–4 mm/yr. Furthermore, there is no obvious velocity change in both profile 3 and profile 4. This result indicates that the Shanchiao Fault shows less activity from north to south, which might be the evidence to form the triangular-shaped half-graben observed by stratigraphy from deep drill data.

The LOS rate from the whole two years dataset of PSInSAR is superimposed on the LiDAR-derived DEM to try mapping the trace of the Shanchiao Fault in Wuku area (Fig. 10, left panel). The black dashed line is the surface trace of the Shanchiao Fault from 1:25,000-scale active fault map published by Central Geological Survey, MOEA (Lin et al., 2000); green line is morphotectonic analysis based on LiDAR-derived DEM made by Chang et al. (2014). Our PSInSAR result suggests that a localized deformation change is located between boreholes SCF-2 and WK-1 shown by navy dashed line. In addition, only slight velocity gradient changes are observed from PSInSAR profile across the Sanchiao Fault proposed by Central Geological Survey, in which Lin et al. (2010) suggested that the main Sanchiao Fault is located between boreholes SCF-1 and SCF-2. Thus surface trace of black dashed line could be the secondary fault of the Shanchiao Fault zone, which is consistent with the previous study based on the correlation between geomorphology
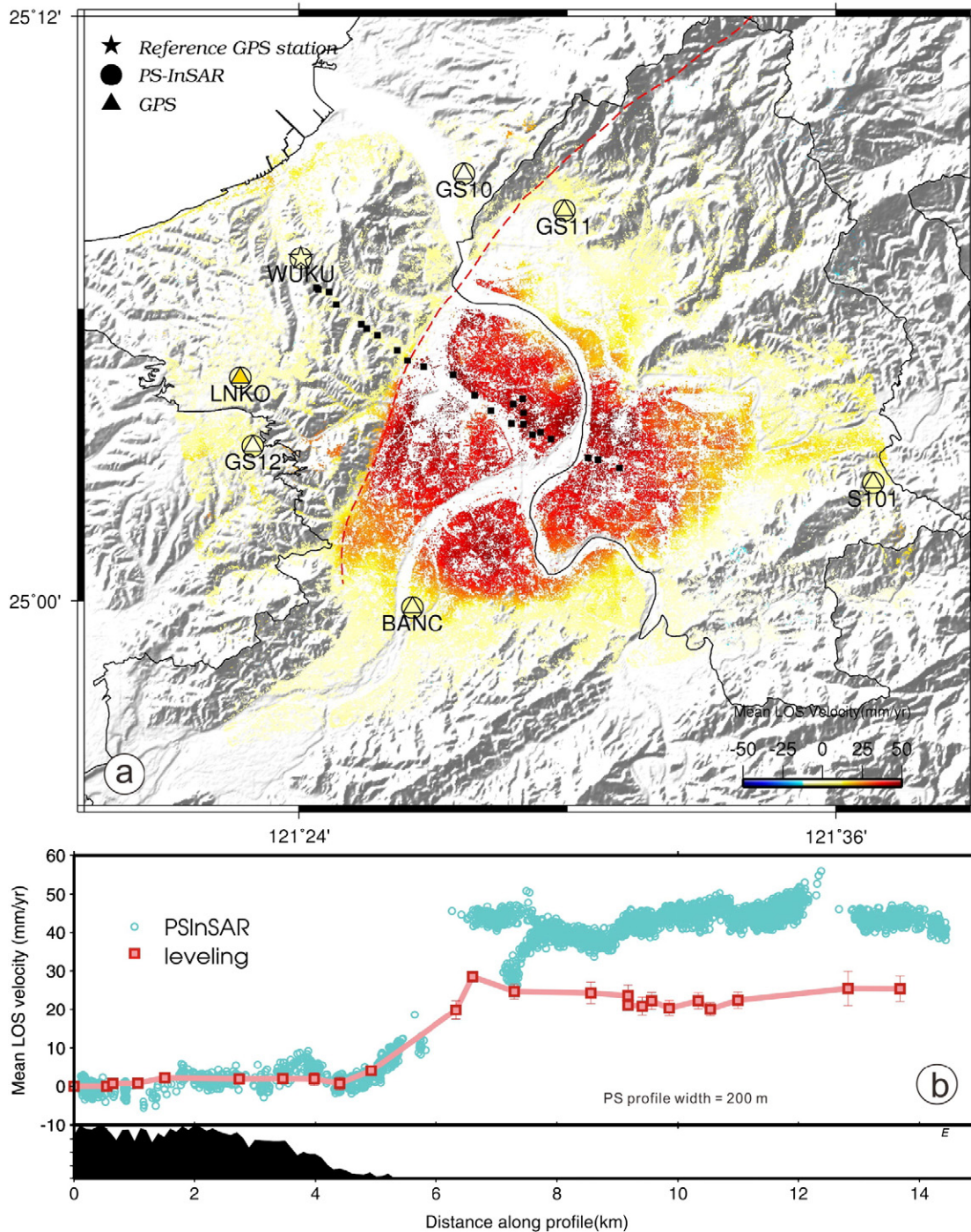
Fig. 8. (a) Slant range displacement rate of time span 2012/9–2013/7. (b) Comparison between the leveling data and PSInSAR result along the central of the Taipei Basin. Black rectangles are the locations of benchmarks in leveling route. Both PS and leveling data are relatively to the westernmost benchmark (WUKU) of the profile.

and subsurface geology of three boreholes in the Shanchiao Fault zone (Fig. 10, right upper panel, Chen et al., 2010a). By contrast, our PSInSAR result proposed that the main Shanchiao Fault is located between the boreholes SCF-2 and WK-1 (Fig. 10, right lower panel), in agreement with the study of Chen et al. (2014), Fig. 10, left panel in pink). Furthermore, our PSInSAR result can improve to map the trace of the Shanchiao Fault and rectify the limited number of borehole locations.

There is a vertical offset of Tertiary strata of more than 700 m across the north and central Shanchiao Fault (Wang et al., 1994, 1995; Teng et al., 2001, see Fig. 1b). This implies that the activity of the north-central segment of the Shanchiao Fault is higher than its southern

segment. Based on average LOS rate of PSInSAR in the Taipei Basin (Fig. 6), Luzhou area shows highest gradient of LOS rate across the Shanchiao Fault, which is consistent with the maximum vertical offset in Tertiary strata in northern segment of the fault. However, spatial distribution of confined aquifers and temporal fluctuation of the groundwater are the major control factors of the ground deformation (Chen et al., 2007). Using two drilling holes data in Wuku and central Taipei, the soil compaction is in a range of 2–3.5 mm/yr and the deep tectonic load is in a range of 0.9–1.8 mm/yr. Our study indicates that one meter groundwater level change could induce about 8 and 16 mm surface deformation change in Luzou and Wuku area respectively, which is
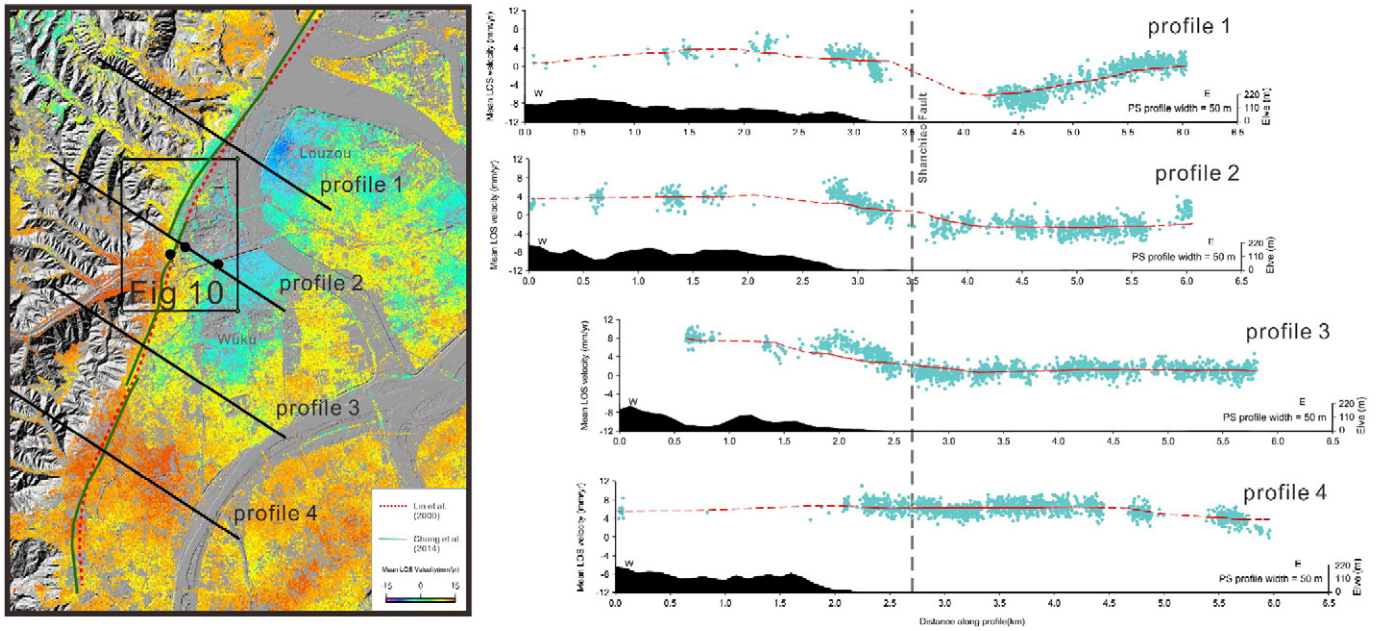
Fig. 9. Four velocity profiles of the Shanchiao Fault within the Taipei Basin. Red dash line represents 1:25,000-scale active fault map published by Central Geological Survey, MOEA; green lines represent morphotectonic analysis based on LiDAR-derived DEM. Rectangle is the location of Fig. 10. Three solid circles are boreholes sites used in Fig. 10.

about eight times faster the long-term tectonic deformation rate in this area. Consequently the aquifer deformation controls the vertical ground deformation, for instance it is difficult to characterize the along-strike deformation gradient without detailed investigation of spatial distribution and thickness of major confined aquifers in the Taipei Basin.

4.2. Extract hydraulic parameter from correlation of PSInSAR and groundwater level

Storativity (S, as well as storage coefficient) is defined as the volume of water taken into or expelled from storage per unit decline in
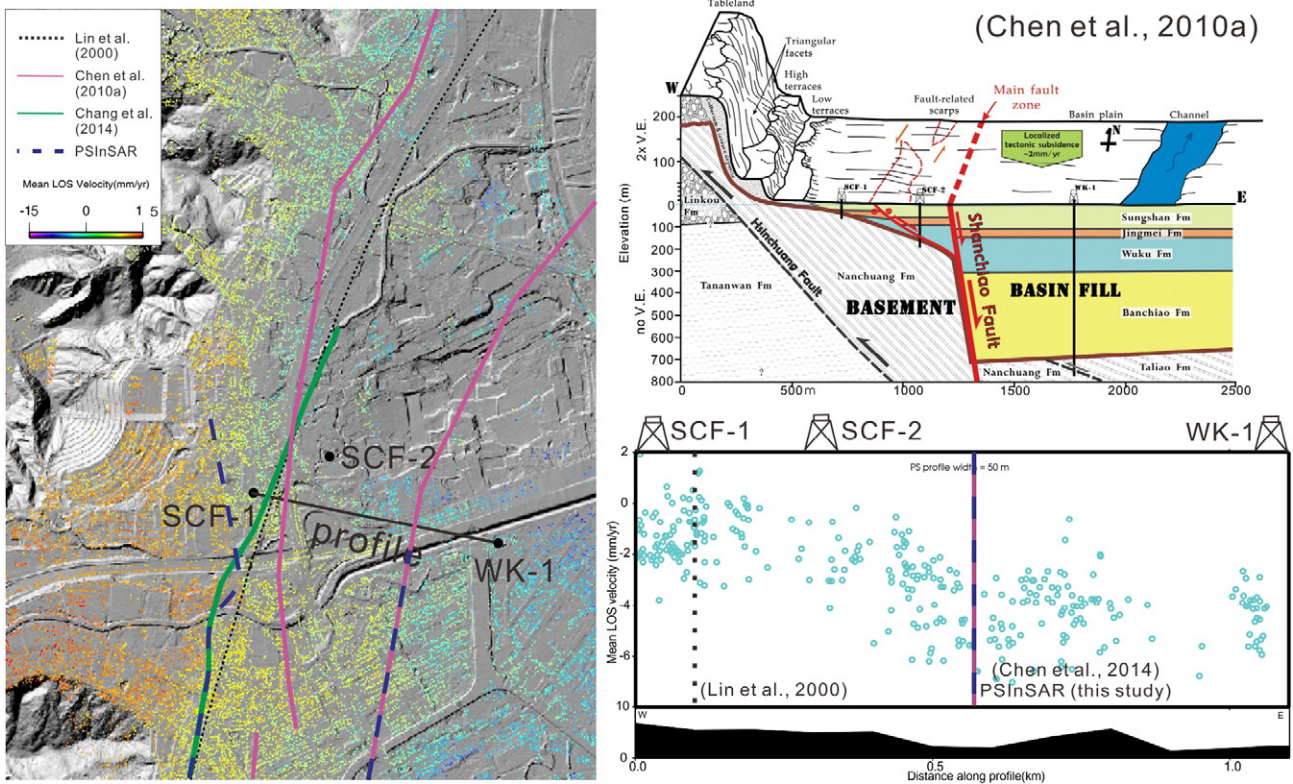
Fig. 10. Comparison of fault properties characterizing. Black dash line represents 1:25,000-scale active fault map published by Central Geological Survey, MOEA; red lines represent fault activity front decided by PSInSAR result. SCF-1 and WK-1 show the locations of two boreholes used in Chen et al. (2010a).

hydraulic head, per unit area of the aquifer. It quantifies the amount of groundwater obtained by vertical aquifer-system compaction and helps to define maximum pumping rate in the elastic range of deformation. In this paper, we use the relationship between hydraulic head changes and surface deformation ($S = d/h$, where d is the vertical ground displacement and h is the hydraulic head change) to characterize the storativity at the seven wells within the metropolitan Taipei City. In the period 2011/9–2012/9, the time series of PSInSAR demonstrate the decline of the LOS displacement from 10 mm to −20 mm (Fig. 11b). By contrast in the period 2012/9–2013/7, the time series of PSInSAR shows an increase of LOS displacement from −20 mm to 10 mm. Water Resources Agency of the Ministry of Economic Affairs of Taiwan installed more than 20 observation wells in the Taipei Basin to monitor the groundwater tables over the years. Here we take Wuku well as an example to demonstrate the relationship between surface

deformation and groundwater level change (Fig. 11). It is worthy to know that the groundwater level shows a similar trend in the period of observation from SAR interferometry only in the Wuku(2) and Wuku(3), which are located at the Jingmei Formation and Wuku Formation, respectively (Fig. 11b). The groundwater level declines from about −6 m to −16 m in Wuku(2) and from −8 m to −18 m in Wuku(3) at the first period and recovers from −16 m to −4 m in Wuku(2) and from −18 m to −5 m in Wuku(3) at the second period. Thus we use the correlation of surface deformation from time series of PSInSAR and groundwater level to calculate the storativity in the Wuku area. The correlation between 18 points from LOS displacement and groundwater level give a storativity of 0.0016 in Jingmei Formation and 0.0014 in Wuku Formation(Fig. 11c), that is 10 m of hydraulic head change can induce about 1.4 to 1.6 cm of surface deformation. According to the stratigraphic, Wuku well is formed by sand and gravel. On the other hand, it
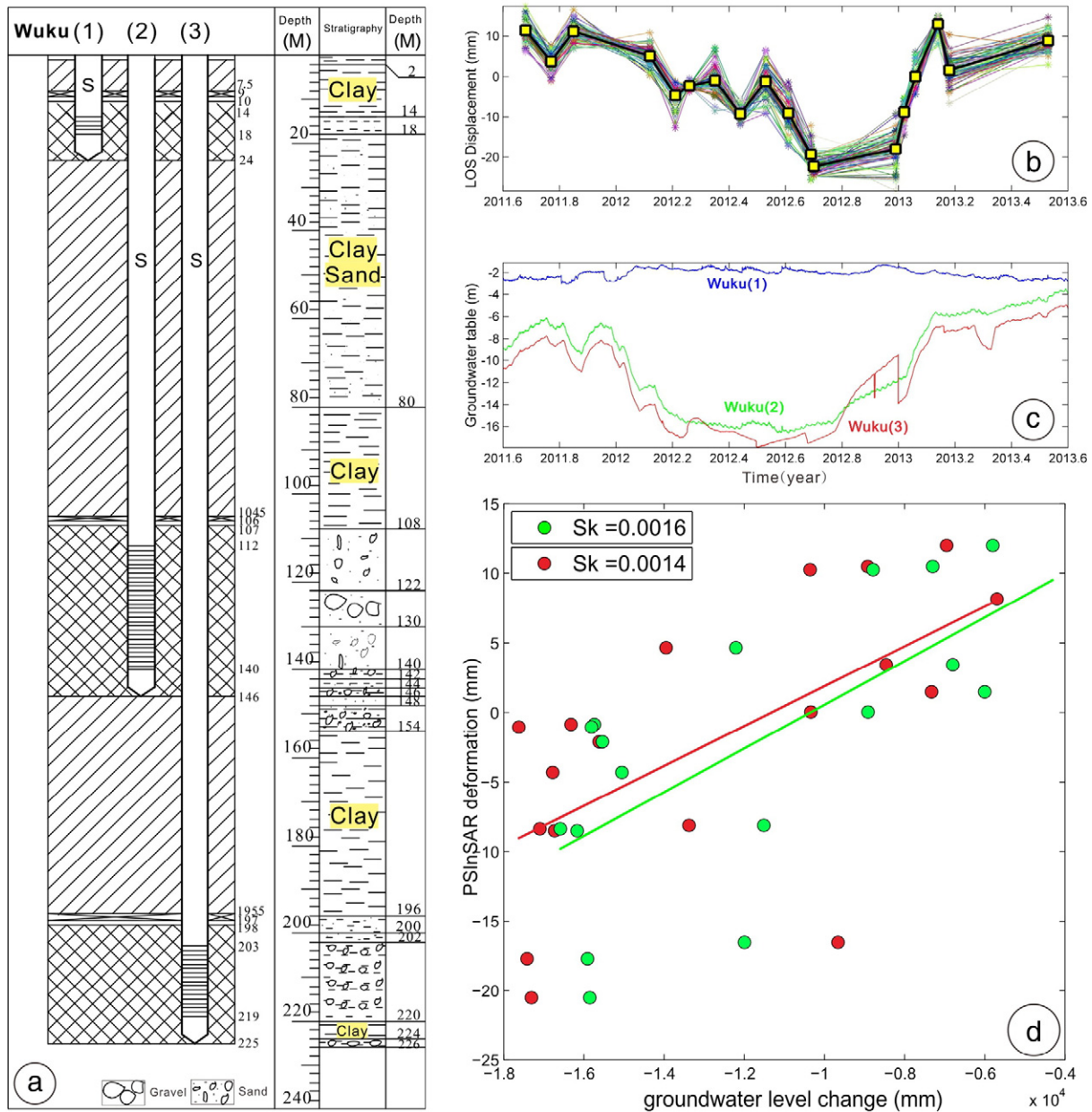
Fig. 11. (a) Stratigraphy of groundwater well Wuku. (b) Time series of average PS points value within 100 m of groundwater well Wuku. (c) Groundwater level change of groundwater well Wuku from September 2011 to July 2013. (d) Storativity calculated from surface deformation of PSInSAR and change of groundwater level. Solid line is the best fitting of linear regression; corresponds to the storativity.

Table 1
Hydrological information and storativities of 9 wells in Taipei basin.

Station name	Depth (m)	Formation	Storativity
Wuku	147.2/268.4	Jingmei/Wuku	0.0016/0.0014
Xinzhuang	107/174	Jingmei/Wuku	0.0010/0.0012
Banqiao	118.5	Jingmei	0.0005
Luzou	126.0	Jingmei	0.0009
Juangjing	79.0	Jingmei	0.0012
Erchong	96.6	Wuku	0.0010
Sanchong	107.4	Wuku	0.0013
Youth Park	85	Jingmei/Wuku	0.0008
Taida	60.0	Jingmei	− 0.0006

contained thick layer clay at the depth of 18 m to 108 m and 154 m to 196 m, which might be the main contribution to the surface deformation observed by PSInSAR.

We also calculate the storativity from the additional 8 wells (Taida, Juangjing, Banqiao, Luzou, Youth Park, Xinzhuang, Erchong and Sanchong) by the above-mentioned method (Table 1) except the Taida well, where the storativity is roughly constant across most of the aquifer with values between 0.5×10^{-4} and 1.6×10^{-3} in Jingmei Formation and 0.8×10^{-4} and 1.4×10^{-3} in Wuku Formation (Table 1). The calculated storativities are in good agreement with values from water pumping test in Jingmei Formation ranging from 1×10^{-3} to 4×10^{-3} (Chia et al., 1999). Besides, the storativity is significantly increased westward. This trend fits well with the deposit depth within the Taipei Basin (Fig. 12). Under the Jingmei formation (Fig. 2), it is worthy to note that the transient deformation induced from groundwater change is basin-wide, which should be related to the distribution of stratigraphy and its hydro-geologic condition. This preliminary result suggested that ground deformation is most likely related to the distribution of Jingmei and Wuku Formations which are the main confined aquifers in the Taipei Basin.

Based on the InSAR-derived surface deformation and groundwater wells in Tainan Tableland, Huang et al. (2016) calculate that the storativity varies from 0.0047 in 1996–2001 to 0.0075 in 2004–2009. Chaussard et al. (2014) suggested that InSAR combined with hydraulic data can characterize the aquifer-system properties at basin scale. In the future, the storativity can be converted to specific storage and values of aquifer compressibility for water resources management in Taiwan.

5. Conclusion

In this paper, we characterize the transient surface deformation in Taipei metropolitan area induced by groundwater change by using high resolution X-band time series analysis form September 2011 to July 2013. Based on 8 well data in the Taipei basin, the calculated storativity is roughly constant with values between 0.5×10^{-4} and 1.6×10^{-3} in Jingmei Formation and 0.8×10^{-4} and 1.4×10^{-3} in Wuku Formation. The transient deformation in LOS of PSInSAR suggested that the severe land subsidence in the Taipei Basin is highly related to confined aquifer deformation of Jingmei and Wuku Formations. Thus the distribution and thickness of Jingmei and Wuku Formations is an important issue for study groundwater induced deformation in the Taipei Basin. In future study, how to discriminate tectonic movement from anthropogenic or seasonal effects is a crucial issue to assess geohazards of seismogenic Shanchiao Fault. We propose a detailed investigation of ground deformation induced by groundwater change by dense continuous GPS network in the Taipei Basin and time series analysis from PSInSAR with the hydro-geological information of major confined aquifers in the Taipei Basin. For instance, with only three continuous GPS stations available in the Taipei Basin (Fig. 3), the deployment of a dense continuous GPS network should be the first concern in a study of the activity of the Shanchiao Fault.

Fig. 12. Storativity calculated in 9 wells within the Taipei Basin. Square and circle represent the location of the well in Jingmei Formation and Wuku Formation, respectively. Circle with square inside represents well located both in Jingmei and Wuku Formations.

Acknowledgments

References

Abidin, H.Z., Djaja, R., Darmawan, D., Hadi, S., Akbar, A., Rajiyowiryono, H., Sudibyo, Y., Meilano, I., Kasuma, M.A., Kahar, J., Subarya, C., 2001. Land subsidence of Jakarta (Indonesia) and its geodetic monitoring system. Nat. Hazards 23, 365–387.

Allen, D.R., Mayuga, M.N., 1969. The Mechanics of Compaction and Rebound, Wilmington Oil Field, Long Beach, California, USA, International Hydrological Decade, Symposium on Land Subsidence, Tokyo, Japan 17–22 Sept.

Amelung, F.D., Galloway, L., Bell, J.W., Zebker, H.A., Laczniak, R.J., 1999. Sensing the ups and downs of Las Vegas: InSAR reveals structural control of land subsidence and aquifer-system deformation. Geology 27 (6), 483–486. http://dx.doi.org/10.1130/0091-7613(1999)027<0483:STUADO>2.3.CO;2.

Bell, J.W., Amelung, F., Ferretti, A., Bianchi, M., Novali, F., 2008. Permanent scatterer InSAR reveals seasonal and long-term aquifer-system response to groundwater pumping and artificial recharge. Water Resour. Res. 44, W02407. http://dx.doi.org/10.1029/2007WR006152.

Berardino, P., Fornaro, G., Lanari, R., Sansosti, E., 2002. A new algorithm for surface deformation monitoring based on small baseline differential SAR interferograms. IEEE Trans. Geosci. Remote Sens. 40 (11), 2375–2383.

Buckley, S.M., Rosen, P.A., Hensley, S., Tapley, B.D., 2003. Land subsidence in Houston, Texas, measured by radar interferometry and constrained by extensometers. J. Geophys. Res. 108 (B11), 2542. http://dx.doi.org/10.1029/2002JB001848.

Bürgmann, R., Rosen, P.A., Fielding, E.J., 2000. Synthetic aperture radar interferometry to measure Earth's surface topography and its deformation. Annu. Rev. Earth Planet. Sci. 28, 169–209.

Champenois, J., Fruneau, B., Pathier, E., Deffontaines, B., Lin, K.-C., Hu, J.-C., 2012. Monitoring of active tectonic deformations in the Longitudinal Valley (eastern Taiwan) using persistent scatterer InSAR method with ALOS PALSAR data. Earth Planet. Sci. Lett. 337-338, 144–155. http://dx.doi.org/10.1016/j.epsl.2012.05.025.

Chang, C.-P., Yen, J.-Y., Hooper, A., Chou, F.-M., Chen, Y.-A., Hou, C.-S., Hung, W.-C., Lin, M.-S., 2010. Monitoring of surface deformation in northern Taiwan using DInSAR and PSInSAR techniques. Terr. Atmos. Ocean. Sci. 21 (3), 447–461. http://dx.doi.org/10.3319/TAO.2009.11.20.01(TH).

Chang, K.-J., Shyu, J.B.H., Chen, R.-F., Chan, Y.-C., Yeh, E.-C., Lai, K.-Y., 2014. Study and investigate characteristics of important active faults: Analyze and interpret near fault high resolution geomorphological data. Project Report, Central Geological Survey, MOEA, p. 327 (in Chinese with English abstract).

Chaussard, E., Amelung, F., Abidin, H., Hong, S.-H., 2013. Sinking cities in Indonesia: ALOS PALSAR detects rapid subsidence due to groundwater and gas extraction. Remote Sens. Environ. 128, 150–161. http://dx.doi.org/10.1016/j.rse.2012.10.015.

Chaussard, E., Bürgmann, R., Shirzaei, M., Fielding, E.J., Baker, B., 2014. Predictability of hydraulic head changes and characterization of aquifer-system and fault properties from InSAR-derived ground deformation. J. Geophys. Res. Solid Earth 119, 6572–6590. http://dx.doi.org/10.1002/2014JB011266.

Chen, C.-T., Lee, J.-C., Hu, J.-C., Chan, Y.-C., Lu, C.-Y., 2006. The active Shanchiao Fault in the Metropolitan Taipei area, northern Taiwan: geomorphic and geodetic analyses. Eos, Trans., AGU, 87–52, Fall Meeting Supplement, Abstract T33D-0543.

Chen, C.-T., Hu, J.-C., Lu, C.-Y., Lee, J.-C., Chan, Y.-C., 2007. Thirty-year land elevation change from subsidence to uplift following the termination of groundwater pumping and its geological implications in the Metropolitan Taipei Basin, northern Taiwan. Eng. Geol. 95, 30–47. http://dx.doi.org/10.1016/j.enggeo.2007.09.001.

Chen, C.-T., Lee, J.-C., Chan, Y.-C., Lu, C.-Y., 2010a. Growth normal faulting at the western edge of the Metropolitan Taipei Basin since the last Glacial Maximum, northern Taiwan. Terr. Atmos. Ocean. Sci. 21 (3), 447–461. http://dx.doi.org/10.3319/TAO.2009.11.20.01(TH).

Chen, C.-T., Lee, J.-C., Chen, Y.-C., Lu, C.-Y., Teng, S.-Y., 2014. Elucidating the geometry of the active Shanchiao fault in the Taipei metropolis, northern Taiwan, and the reactivation relationship with pre-existing orogen structures. Tectonics 33, 2400–2418. http://dx.doi.org/10.1002/2013TC003502.

Chen, K.-C., Huang, B.-S., Huang, W.-G., Wang, J.-H., Kim, K.-H., Lee, S.-J., Lai, Y.-C., Tsao, S., Chen, C.-H., 2010b. A blind normal fault beneath the Taipei Basin in northern Taiwan. Terr. Atmos. Ocean. Sci. 21 (3), 495–502. http://dx.doi.org/10.3319/TAO.2010.01.25.01(TH).

Chia, Y.-P., Chang, M.-H., Liu, W.-I., Lai, T.-C., 1999. Hydrogeologic characterization of Taipei Basin. Cent. Geol. Surv. Spec. Publ. 11, 393–406 (in Chinese with English abstract).

Crosetto, M., Castillo, M., Arbiol, R., 2003. Urban subsidence monitoring using radar interferometry: algorithms and validation. Photogramm. Eng. Remote Sens. 69, 775–783.

Ding, X.-L., Liu, G.-X., Li, Z.-W., Li, Z.-L., Chen, Y.-Q., 2004. Ground subsidencemonitoring in Hong Kong with satellite SAR interferometry. Photogramm. Eng. Remote Sens. 70 (10), 1151–1156.

Ferretti, A., Prati, C., Rocca, F., 2000. Nonlinear subsidence rate estimation using permanent scatterers in differential SAR interferometry. IEEE Trans. Geosci. Remote Sens. 38, 2202–2212.

Ferretti, A., Prati, C., Rocca, F., 2001. Permanent scatterers in SAR interferometry. IEEE Trans. Geosci. Remote Sens. 39 (1), 8–20.

Galloway, D.L., Hoffmann, J., 2007. The application of satellite differential SAR interferometry-derived ground displacements in hydrogeology. Hydrogeol. J. 15, 133–154.

Holzer, T.L., 1984. Ground failure induced by groundwater withdrawal from unconsolidated sediments. Rev. Eng. Geol. 6, 67–105.

Hooper, A., Zebker, H., Segall, P., Kampes, B., 2004. A new method for measuring deformation on volcanoes and other natural terrains using InSAR persistent scatterers. Geophys. Res. Lett. 31 (23), L23611. http://dx.doi.org/10.1029/2004GL021737.

Hou, C.-S., Hu, J.-C., Shen, L.-C., Wang, J.-S., Chen, C.-L., Lai, T.-C., Huang, C., Yang, Y.-R., Chen, R.-F., Chen, Y.-G., Angelier, J., 2005. Estimation of subsidence using GPS measurements, and related hazard: the Pingtung Plain, southwestern Taiwan. Compt. Rendus Geosci. 337, 1184–1193.

Hsieh, C.-S., Shih, T.-Y., Hu, J.-C., Tung, H., Huang, M.-H., Angelier, J., 2011. Using differential SAR interferometry to map land subsidence: a case study in the Pingtung Plain of SW Taiwan. Nat. Hazards 58 (3), 1331–1332. http://dx.doi.org/10.1007/s11069-011-9734-7.

Hu, J.-C., Angelier, J., Lee, J.-C., Chu, H.-T., Byrne, D., 1996. Kinematics of convergence, deformation and stress distribution in the Taiwan collision area: 2-D finite-element numerical modelling. Tectonophysics 255, 243–268.

Hu, J.-C., Yu, S.-B., Angelier, J., Chu, H.-T., 2001. Active deformation of Taiwan from GPS measurements and numerical simulations. J. Geophys. Res. 106, 2265–2280.

Hu, J.-C., Yu, S.-B., Chu, H.-T., Angelier, J., 2002. Transition tectonics of northern Taiwan induced by convergence and trench retreat, in Byrne, T.B., and Liu, C.-S., eds., geology and geophysics of an arc–continent collision, Taiwan. Geol. Soc. Am. Spec. Pap. 358, 149–162. http://dx.doi.org/10.1130/0-8137-2358-2.147.

Hu, J.-C., Chu, H.-T., Hou, C.-S., Chen, R.-F., Lai, T.-H., Nien, P.-F., 2006. The contribution to tectonic subsidence by groundwater abstraction in the Pingtung area, southwestern Taiwan as determined by GPS measurements. Quat. Int. 147, 62–69. http://dx.doi.org/10.1016/j.quaint.2005.09.007.

Huang, S.-Y., Rubin, C.M., Chen, Y.-G., Liu, H.-C., 2007. Prehistoric earthquakes along the Shanchiao Fault, Taipei Basin, northern Taiwan. J. Asian Earth Sci. 31, 265–276. http://dx.doi.org/10.1016/j.jseaes.2006.07.025.

Huang, M.-H., Bürgmann, R., Hu, J.-C., 2016. Fifteen years of surface deformation in Western Taiwan: Insight from SAR interferometry. Tectonophysics 692, 252–264.

Hung, W.-C., Hwang, C., Chang, C.-P., Yen, J.-Y., Liu, C.-H., Yang, W.-H., 2010. Monitoring severe aquifer-system compaction and land subsidence in Taiwan using multiple sensors: Yunlin, the southern Choshui River alluvial fan. Environ. Earth Sci. 59 (7), 1535–1548. http://dx.doi.org/10.1007/s12665-009-0139-9.

Hung, W.-C., Hwang, C., Chen, Y.-A., Chang, C.-P., Yen, J.-Y., Hooper, A., Yang, C.-Y., 2011. Surface deformation from persistent scatterers SAR interferometry and fusion with leveling data: a case study over the Choshui River alluvial fan, Taiwan. Remote Sens. Environ. 115, 957–967.

Hwang, C., Hung, W.-C., Liu, C.-H., 2008. Results of geodetic and geotechnical monitoring of subsidence for Taiwan high speed rail operation. Nat. Hazards 47, 1–16. http://dx.doi.org/10.1007/s11069-007-92115.

Kampes, B.M., Hanssen, R.F., 2004. Ambiguity resolution for permanent scatterer interferometry. IEEE Trans. Geosci. Remote Sens. 42 (11), 2446–2453.

Kampes, B.M., Usai, S., 1999. Doris: the Delft Object-oriented Radar Interferometric Software. Proceedings of the 2nd International Symposium on Operationalization of Remote Sensing, Enschede, The Netherlands.

Kao, H., Shen, S.J., Ma, K.-F., 1998. Transition from oblique subduction to collision: earthquakes in the southernmost Ryukyu arc-Taiwan region. J. Geophys. Res. 103, 7211–7229.

Kim, K.-H., Chang, C.-H., Ma, K.-F., Chiu, J.-M., Chen, K.-C., 2005. Modern seismic observations in the Tatun volcano region of northern Taiwan: seismic/volcanic hazard adjacent to the Taipei metropolitan area. Terr. Atmos. Ocean. Sci. 16, 579–594.

Konikow, L.F., Kendy, E., 2005. Groundwater depletion: a global problem. Hydrogeol. J. 13, 317–320. http://dx.doi.org/10.1007/s10040-004-0411-8.

Konstantinou, K.I., Lin, C.-H., Liang, W.-T., 2007. Seismicity characteristics of a potentially active Quaternary volcano: the Tatun Volcano group, northern Taiwan. J. Volcanol. Geotherm. Res. 160, 300–318. http://dx.doi.org/10.1016/j.jvolgeores.2006.09.009.

Lai, J.-S., Chiu, C.-Y., Chang, S.-K., Hu, J.-C., Tan, Y.-C., 2010. Potential inundation hazards in the Taipei Basin induced by reactivation of the Shanchiao fault in the northern Taiwan. Terr. Atmos. Ocean. Sci. 21, 529–542. http://dx.doi.org/10.3319/TAO.2010.02.22.01(TH).

Lee, C.-T., Wang, Y., 1988. Quaternary stress changes in northern Taiwan and their tectonic implication. Proc. Geol. Soc. China 31 (1), 154–168.

Lin, C.-H., 2005. Seismicity increase after the construction of the world's tallest building: an active blind fault beneath the Taipei 101. Geophys. Res. Lett. 32, L22313. http://dx.doi.org/10.1029/2005GL024223.

Lin, C.-W., Chang, H.-C., Lu, S.-T., Shih, T.-S., and Huang, W.-J., 2000. An Introduction to the Active Faults of Taiwan: Explanatory Text for the Active Fault Map of Taiwan, Scale 1:500,000, Second Ed. Cen. Geol. Surv. Spec. Publ., 13, 122 pp. (in Chinese with English abstract)

Lin, K.-C., Hu, J.-C., Ching, K.-E., Angelier, J., Rau, R.-J., Yu, S.-B., Tsai, C.-H., Shin, T.-C., Huang, M.-H., 2010. GPS crustal deformation, strain rate and seismic activity after the 1999 Chi-Chi earthquake in Taiwan. J. Geophys. Res. 115, B07404. http://dx.doi.org/10.1029/2009JB006417.

Liu, G.-X., Luo, X.-J., Chen, Q., Huang, D.-F., Ding, X.-L., 2008. Detecting land subsidence in Shanghai by PS-networking SAR interferometry. Sensors 8, 4725–4741.

Lu, Z., Danskin, W., 2001. InSAR analysis of natural recharge to define structure of a ground-water basin, San Bernardino, California. Geophys. Res. Lett. 28 (13), 2661–2664. http://dx.doi.org/10.1029/2000GL012753.

Lu, C.-Y., Angelier, J., Chu, H.-T., Lee, J.-C., 1995. Contractional, transcurrent, rotational and extensional tectonics: examples from northern Taiwan. Tectonophysics 246, 129–146.

Massonnet, D., Feigl, K.L., 1998. Radar interferometry and its application to changes in the Earth's surface. Rev. Geophys. 36 (4), 441–500. http://dx.doi.org/10.1029/97RG03139.

Massonnet, D., Rossi, M., Carmona, C., Adragna, F., Peltzer, G., Feigl, K., Rabaute, T., 1993. The displacement field of the Landers earthquake mapped by radar interferometry. Nature 364, 138–142.

Mora, O., Mallorqui, J.J., Broquetas, A., 2003. Linear and nonlinear terrain deformation maps from a reduced set of interferometric SAR images. IEEE Trans. Geosci. Remote Sens. 41 (10), 2243–2253.

Peyret, M., Dominguez, S., Cattin, R., Champenois, J., Leroy, M., Zajac, A., 2011. Present-day interseismic surface deformation along the Longitudinal Valley, eastern Taiwan, from a PS-InSAR analysis of the ERS satellite archives. J. Geophys. Res. 116, B03402. http://dx.doi.org/10.1029/2010JB007898.

Phien-wej, N., Giao, P.H., Nutalaya, P., 2006. Land subsidence in Bangkok, Thailand. Eng. Geol. 82, 187–201. http://dx.doi.org/10.1016/j.enggeo.2005.10.004.

Pritchard, M.E., Simons, M., 2002. A satellite geodetic survey of large-scale deformation of volcanic centres in the central Andes. Nature 418, 167–171.

Rau, R.-J., Ching, K.-E., Hu, J.-C., Lee, J.-C., 2008. Crustal deformation and block kinematics in transition from collision to subduction: GPS measurements in northern Taiwan, 1995–2005. J. Geophys. Res. 113, B09404. http://dx.doi.org/10.1029/2007JB005414.

Schmidt, D.A., Bürgmann, R., 2003. Time-dependent land uplift and subsidence in the Santa Clara valley, California, from a large interferometric synthetic aperture radar data set. J. Geophys. Res. 108 (B9), 2416. http://dx.doi.org/10.1029/2002JB002267.

Shyu, J.B.H., Sieh, K., Chen, Y.-G., Liu, C.-S., 2005. Neotectonic architecture of Taiwan and its implications for future large earthquakes. J. Geophys. Res. 110, B08402. http://dx.doi.org/10.1029/2004JB003251.

Song, S.-R., Tsao, S., Lo, H.-J., 2000. Characteristics of the Tatun volcanic eruptions, North Taiwan; implications for a cauldron formation and volcanic evolution. J. Geol. Soc. China 43, 361–378.

Suppe, J., 1981. Mechanics of mountain building and metamorphism in Taiwan. Mem. Geol. Soc. China 4, 67–89.

Teatini, P., Ferronato, M., Gambolati, G., Bertoni, W., Gonella, M., 2005. A century of land subsidence in Ravenna, Italy. Environ. Geol. 47, 831–846.

Teng, L.S., 1990. Late Cenozoic arc–continent collision in Taiwan. Tectonophysics 183, 57–76.

Teng, L.S., Yuan, P.B., Chen, P.-Y., Peng, C.-H., Lai, T.-C., Fei, L.-Y., Liu, H.-C., 1999. Lithostratigraphy of Taipei Basin deposits. Cent. Geol. Surv. Spec. Publ. 11, 41–66 (in Chinese with English abstract).

Teng, L.S., Lee, C.-T., Tsai, Y.-B., Hsiao, L.-Y., 2000. Slab breakoff as a mechanism for flipping of subduction polarity in Taiwan. Geology 28, 155–158.

Teng, L.S., Lee, C.-T., Peng, C.-H., Chen, W.-F., Chu, C.-J., 2001. Origin and geological evolution of the Taipei Basin, northern Taiwan. West. Pac. Earth Sci. 1 (2), 115–142.

Tung, H., Hu, J.-C., 2012. Assessments of serious anthropogenic land subsidence in Yunlin County of Central Taiwan from 1996 to 1999 by persistent scatterers InSAR. Tectonophysics 578, 126–135. http://dx.doi.org/10.1016/j.tecto.2012.08.009.

Waltham, T., 2002. Sinking cities—Feature. Geol. Today 18 (3), 95–100.

Wang, C.-Y., Hsiao, W.-C., Sun, C.-T., 1994. Reflection seismic stratigraphy in Taipei basin (I) — northwestern Taipei basin. J. Geol. Soc. China 37, 69–95.

Wang, C.-Y., Tsai, Y.-L., Ger, M.-L., 1995. Reflection seismic stratigraphy in Taipei basin (II) — southwestern Taipei basin. J. Geol. Soc. China 38, 141–172.

Wang, J.-H., Huang, M.-W., Huang, W.-G., 2006. Aspects of M ≥ 4 earthquakes in the Taipei metropolitan area. West. Pac. Earth Sci. 6, 169–190.

Wang, C.-T., Chen, K.-S., Hu, J.-C., Chang, W.-Y., Boerner, W.M., 2011. Mapping land uplift and subsidence in the industrial parks in northern Taiwan by radar interferometry. Int. J. Remote Sens. 32 (21), 6527–6538. http://dx.doi.org/10.1080/01431161.2010.512932.

Wei, K., Chen, Y.-G., Liu, T.-K., 1998. Sedimentary history of the Taipei Basin with constraints from thermoluminescence dates. J. Geol. Soc. China 41, 109–125.

Wilson, A.M., Gorelick, S., 1996. The effects of pulsed pumping on land subsidence in the Santa Clara Valley, California. J. Hydrol. 174 (3), 375–396.

Wright, T.J., 2002. Remote monitoring of the earthquake cycle using satellite radar interferometry. Philos. Trans. R. Soc. Lond. Ser. A 360, 2873–2888. http://dx.doi.org/10.1098/rsta.2002.1094.

Wu, C.-M., 1987. Reviews on the land subsidence of the Taipei Basin (in Chinese). Sino-Geotechnics 20, 34–49.

Wu, Y.-Y., Hu, J.-C., Lin, G.-P., Chang, C.-P., Tung, H., Lu, C.-H., 2013. Transient active deformation in Tainan tableland using persistent scatterers SAR interferometry. Bull. Soc. Geol. Fr. 184 (4–5), 441–450.

Yu, S.-B., Chen, H.-Y., Kuo, L.-C., 1997. Velocity field of GPS stations in the Taiwan area. Tectonophysics 274, 41–59.

Yu, S.-B., Chen, H.-Y., Kou, L.-C., Hou, C.-S., Lee, C.-F., 1999. A study on the fault activities of the Taipei Basin. Spec. Publ. Cent. Geol. Surv. 11, 227–251 (in Chinese with English abstract).

Appendix II

Triggered slip on multifaults after the 2018 Mw 6.4 Hualien earthquake by continuous GPS and InSAR measurements
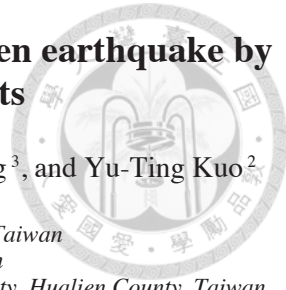
Triggered slip on multifaults after the 2018 M_w 6.4 Hualien earthquake by continuous GPS and InSAR measurements

Hsin Tung[1], Horng-Yue Chen[2], Ya-Ju Hsu[2], Jyr-Ching Hu[1,*], Yo-Ho Chang[3], and Yu-Ting Kuo[2]

[1] Department of Geosciences, National Taiwan University, Taipei City, Taiwan
[2] Institute of Earth Sciences, Academia Sinica, Taipei City, Taiwan
[3] Department of Natural Resources and Environmental Studies, National Dong Hwa University, Hualien County, Taiwan

ABSTRACT

On 6 February 2018 at 23:50 local time, a M_w 6.4 earthquake struck eastern Taiwan. We characterize the instantaneous surface ground motion and the permanent displacement induced by this event from continuous GPS data and SAR images within a short time after the mainshock. We use high-rate GPS positioning techniques to obtain epoch-by-epoch positions peak ground displacement to assess potential seismic damage. The maximum coseismic GPS horizontal displacement of about 450 mm trending to the northeast is observed at the station HUAL located on the hanging wall of the Milun fault. The PEPU located on the footwall of the Milun fault shows a coseismic horizontal displacement of 280 mm trending to the southwest and a coseismic uplift of about 70 mm. Moreover, ascending and descending tracks of ALOS-2 and Sentinel-1 SAR images are processed to estimate coseismic surface deformation along the line-of-sight (LOS) toward the satellite. Then, wide coverage from east-west and uplift components of surface deformation is fulfilled by combining the LOS displacement from ascending and descending interferograms. The main deformation area revealed by both GPS results and D-InSAR interferograms is concentrated around the Milun and Lingding faults. Significant uplift on the footwall of the northern Lingding Fault implies that the Milun fault and an unknown west-dipping fault close to the Lingding fault were triggered. Both the two nodal planes of the M_w 6.4 Hualien event could be different with the kinematic behavior of the Milun fault and Lingding fault. Thus we suggest that slip on multiple faults was triggered during the 0206 event.

1. INTRODUCTION

At 21:56:41 local time on 4 February 2018, a M_w 6.0 (0204 event) occurred in the Hsinchen Ridge offshore the city of Hualien (Fig. 1). According to the focal mechanism of this event, the possible seismogenic fault is a nearly E-W-striking and gently north-dipping thrust fault with a minor dextral strike-slip component. This event could be interpreted as a regular subduction zone earthquake that occurred at the complex junction of convergence boundary of the Philippine Sea plate and Eurasian plate. Two days later, a M_w 6.4 earthquake (0206 event) occurred near the epicenter of 0204 event with a different focal mechanism. The epicenter of this second event was located in the offshore area

~16.5 km northeast of city of Hualien at a depth of 6 km resulting in 17 deaths with 285 injured. Based on the Central Weather Bureau (CWB) intensity scale, the peak ground acceleration (PGA) larger than 400 gals were measured in Hualien. This extremely large ground shaking caused severe building damage, including four that had partially collapsed. Thousands of aftershocks were recorded by Geophysical Database Management System (https://gdms.cwb.gov.tw/index.php) of CWB within 14 days (Kuo-Chen et al. 2019). Aftershocks were propagated southward from the hypocenter of the mainshock to the Longitudinal Valley (Chang et al. 2019; Chen et al. 2019).

According to field investigations, the major surface rupture was identified along the Milun fault (Huang et al. 2019; Lin et al. 2019; Wu et al. 2019), an active fault that

---

* *Corresponding author*
  E-mail: jchu@ntu.edu.tw

ruptured during a M_L 7.1 earthquake in 1951 (Hsu 1962, 1971; Bonilla 1975, 1977). Based on the focal mechanism solution, a NE-striking and NW-dipping nodal plane is considered as the seismogenic fault plane indicating a reverse faulting with a sinistral strike-slip component. An alternative nodal plane is close to a EW-striking south-dipping reverse fault with dextral slip component. However, both these two nodal plane are hard to connect to any known active fault near the epicenter. Furthermore, the coseismic deformation patterns revealed by continuous GPS measurements and SAR interferograms were observed both on the hanging wall and footwall of the Milun fault, which is a NE-striking and east-dipping reverse fault with a sinistral motion based on geological data (e.g., Shyu et al. 2005). In addition, significant coseismic deformation behavior also observed on the footwall part of the Lingding fault which is the northern segment of the Longitudinal Valley fault, suggesting that the 0206 Hualien earthquake triggered multiple ruptures on different fault systems (Huang and Huang 2018; Yang et al. 2018), similar to multiple fault slip founded during the 2010 M_w 6.2 Jia-Shian earthquake (Lin et al. 2016), the 2016 M_w 6.4 Meinong earthquake in southern Taiwan (Huang et al. 2016; Le Béon et al. 2017) and the 2016 M_w 7.8 Kaikōura

earthquake in New Zealand (Hamling et al. 2017). The shallow rupture of the Milun fault and its kinematic behavior are also revealed by optical satellite and numerical modeling (Kuo et al. 2019). They proposed the different locking depth and kinematic behavior in the north and south segment of the Milun fault. In addition, the detailed insights of seismogenic deformation near the Milun fault by 3D displacement field by GPS, InSAR and pixel offsets from ALOS-2 radar image are deduced to suggest the Milun and Lingding faults belong to same fault zone (Yen et al. 2019). The coseismic deformation also conducted by using strong motion recordings (Tian et al. 2019). They indicated that the Milun fault could have experienced a left-lateral motion during the Hualien event.

To better characterize coseismic deformation of multiple fault slip triggered by the 0206 offshore Hualien earthquake, we use continuous GPS (cGPS) data from the Taiwan cGPS array and 12 cGPS sites operated by the NDHU to estimate the coseismic displacement around the epicenter as well as along the Milun and Lingding fault systems. In addition, differential interferometry synthetic aperture radar (D-InSAR) technique from ALOS-2 and Sentinel-1 radar images are used to characterize coseismic deformation
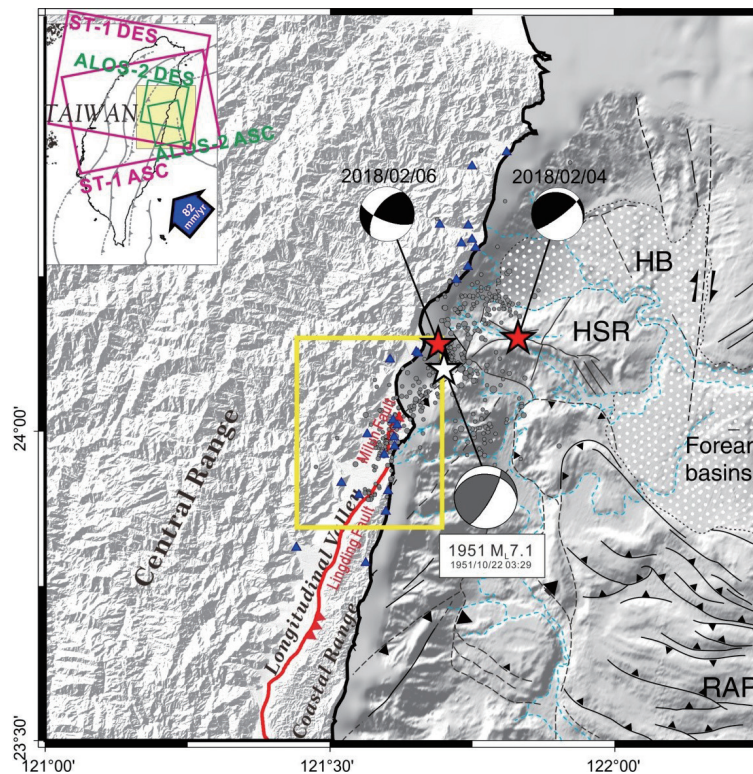

Fig. 1. Locations for continuous GPS stations (blue triangles), SAR coverage (rectangle) and focal mechanism of the 2018 0204 M_w 6.0 and 0206 M_w 6.4 earthquakes in Taiwan. White star is the M_L 7.1 event of the 1951 Hualien-Taitung earthquake sequence, and gray circles are the aftershocks occurred within two weeks after the 0206 event. Yellow rectangle indicates study area. ASC represents ascending orbit while DES represents descending orbit. ST-1 represents Sentinel-1 satellite. Blue arrow shows the plate convergence rate between the Philippines Sea plate and Eurasian plate (after Lin et al. 2010). Offshore bathymetry and tectonic structures are based on Malavieille et al. (2002). HSR represents Hsinchen Ridge, HB represents Hoping Basin, and RAP indicates Ryukyu Accretionary Prism.

patterns and fault ruptures associated with the mainshock. Furthermore, high-rate GPS data (1 Hz sampling rate) of cGPS are used to estimate the peak ground displacement (PGD) adjacent to the hypocenter for assessing the potential seismic damage. Finally, we calculate the arrival time of the PGD from cGPS stations to infer the multiple fault slip triggered by the M_w 6.4 event.

Although there are several papers have been published using geodetic data such as campaign GPS, InSAR, precise leveling and pixel offtrack techniques based on optical and SAR images to explain the coseismic deformation and to inverse the coseismic slip on patches of the seismogenic fault or triggered fault systems. However, all these geodetic results might be contaminated by interseismic and postseismic displacements. In this paper, we provide both instantaneous surface ground motion and the permanent displacement from continuous high-rate GPS data within a short time after the event with detail processing strategy. We also provide reliable high-rate GPS waveforms which could be used for time-dependent modeling of this event for the future study.

2. DATA ACQUISITION AND PROCESSING

To study the instantaneous surface ground motion and the permanent displacement caused by the earthquake, we used GPS observations and SAR images to measure precise positioning coordinates and the differential movements around the epicenter. GPS data provide a nice temporal resolution for the rupture process where as SAR images offer a better spatial coverage of deformation pattern.

2.1 GPS Observations

Taiwan's cGPS array is one of the densest GPS networks in the world. There are more than 400 stations over an area of 36000 km^2 (Tsai et al. 2015). To enhance the near real-time applications, internet transmission and latest generation dual-frequency receiver with multi-satellites recording function were installed in most stations. The data are mainly collected by the Central Weather Bureau (CWB), the Ministry of Interior Affairs (MOI), the Institute of Earth Sciences, Academia Sinica (IESAS), the Central Geological Survey (CGS), and the Water Resources Agency (WRA). Furthermore, the National Dong Hwa University also provides GPS data in Hualien (Fig. 1). In order to precisely determine the coseismic displacement and surface ground motion, we collected cGPS data from 1st to 11th February with sampling rate of 30-s to estimate instantaneous positioning and daily solutions, respectively (Fig. 2). Furthermore, high-rate GPS positioning techniques have been developed to obtain epoch-by-epoch positions and these solutions are capable of recording seismic motion acting as GPS Seismology (e.g., Nikolaidis et al. 2001; Bock et al. 2004). In this study, 1 Hz sampling rate data of cGPS are used both to estimate the instantaneous positioning (Fig. 2) and PGD of the GPS station for assessing the potential seismic damage (detail in discussion).

We utilize the GIPSY-OASIS II software (Webb and

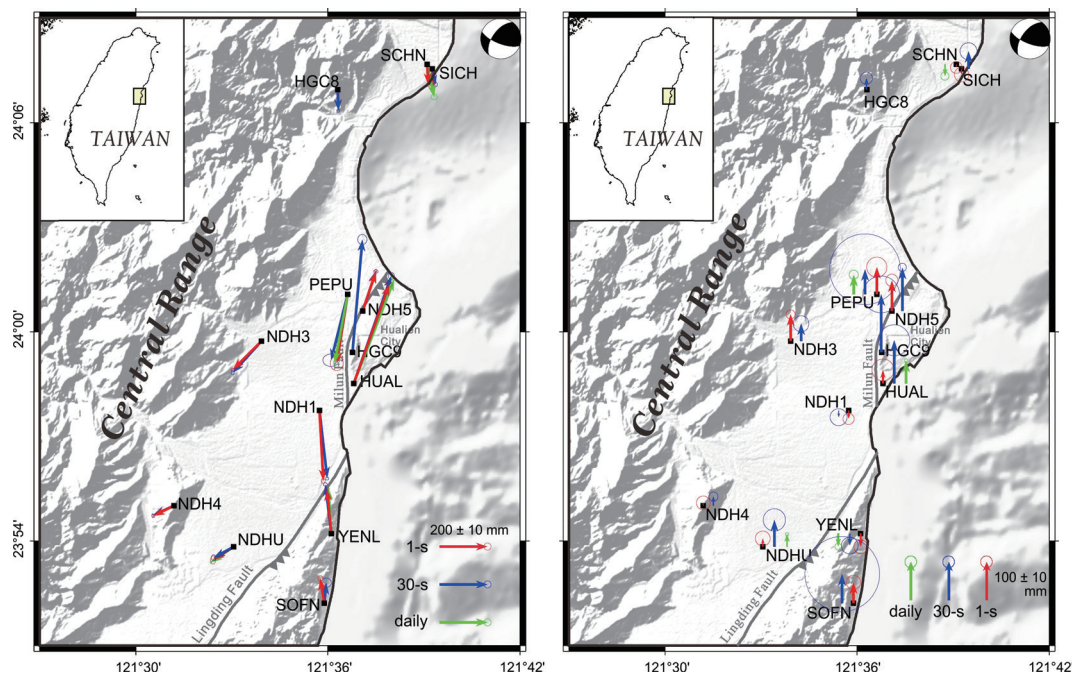Fig. 2. Coseismic displacements of cGPS stations for the M_w 6.4 Hualien earthquake. Blue arrows represent position difference using the average of 30-s solutions 60 min prior to and post the mainshock; red arrows represent 1-hz solutions using 60 s GPS before and after the mainshock, and green arrows represent position differences between the averages GPS positions 5 days prior to and post the mainshock.

Zumberge 1997) to estimate the coordinates in precise point positioning (PPP) method. The PPP technique acquires absolute position using a single GPS station, which has a lower precision than the differential technique (GAMIT from Herring et al. 2009 or Bernese from Dach et al. 2007) with the capability of removing the common errors from two or more stations. The accuracy of PPP depends on the ability of mitigating all kinds of errors. In this study, the International GNSS Service (IGS) final products were used to reduce satellite orbit and clock errors in the data procedures. Besides, Vienna Mapping Function (VMF1) and antenna calibration provided from NOAA's National Geodetic Survey were used to reduce atmosphere delay and receiver error.

2.2 D-InSAR

We combined both ALOS-2 and Sentinel-1 ascending and descending SAR data to measure the coseismic deformation fields of the Hualian earthquake. Table 1 presents the detailed information of the used SAR data, and the coverage of the four tracks is shown in Fig. 1. After the 0206 event, Advanced Land Observing Satellite-2 (ALOS-2) launched by Japan Aerospace Exploration Agency (JAXA) passed over the Hualien area on 10 and 11 February for emergency observation with stripmap mode SAR images. Thus, one ascending interferogram (2016/11/05 - 2018/02/10) and one descending interferogram (2017/06/18 - 2018/02/11) could be generated with two historical images. In addition, Sentinel-1 satellite constellation launched by the European Space Agency (ESA) also provided Wide (IW) mode ascending and descending images in 3 days and 5 days after the 0206 event, respectively. After that, two interferograms with a six-days interval could be generated (2018/02/03 - 2018/02/09 for ascending pair and 2018/02/05 - 2018/02/11 for descending pair). The four interferograms were generated using the ISCE (InSAR Scientific Computing Environment) software developed by the JPL/Caltech (Rosen et al. 2012). One-arc-second resolution Shuttle Radar Topography Mission (SRTM) digital elevation model (Farr et al. 2007) was used to remove the topography phase component during interferogram processing to estimate surface deformation in the area covering the Milun fault and the northern part of the Lingding fault (Fig. 3). Finally, Snaphu version 1.4.2 (Chen and Zebker 2000) has been applied to process phase unwrapping (Fig. 4).

3. COSEISMIC DISPLACEMENT OBSERVED FROM CGPS AND D-INSAR

GPS observations and SAR interferograms can be used to estimate coseismic displacements at different time scales. First, we use GPS daily solution and 1 Hz sampling data to determine the coseismic deformation. Second, we use D-InSAR technique with Sentinel-1 and ALOS-2 images to evaluate the regional deformation patterns over a week after the mainshock and over a longer time period which might include both coseismic and postseismic deformation of the M_w 6.4 Hualien earthquake.

3.1 cGPS Result

From the different precise orbit and clock products released from JPL, we estimate 3 coseismic displacement fields from (1) GPS positions difference between the averages of 30-s solutions 60 min prior to and post the mainshock with rapid orbit in two days after the 0206 event; (2) positions difference between the averages of 1-hz solutions 60 s prior to and post the mainshock; (3) difference between the averages daily solutions 5 days prior to and post the mainshock with final orbit in 14 days after the 0206 event (Fig. 2 and Table 2). Unfortunately, due to the data exchange policy and failure of power supply after the Hualien earthquake, only few GPS stations were available for estimates of daily solutions. However, the results of the 3 different processing strategies indicate similar coseismic deformation patterns observed along the Milun fault and Lingding fault (Fig. 2).

The maximum horizontal displacement is measured in the GPS station HUAL, which is sat in downtown of Hualien and hanging wall of the Milun fault, with a horizontal displacement of about 450 mm trending to northeast and varies in uplift from 35 - 115 mm. Furthermore, the GPS station NDH5 and HGC9 located on the hanging wall of the

Table 1. Parameters of differential SAR interferometric pairs of ALOS-2 and Sentinel-1 images.

| Pair	Satellite	Image Resolution (m)	Flight direction	Acquisition Date	Time Interval (days)	Heading Angle	Incidence Angle	Perpendicular Baseline (m)
1	ALOS-2 ALOS-2	6	Ascending	2016/11/05 2018/02/10	461	347.9°	27.8°	-160.7
2	ALOS-2 ALOS-2	10	Descending	2017/06/18 2018/02/11	238	192.1°	40.6°	229.2
3	Sentinel-1A Sentinel-1B	5 × 20 5 × 20	Ascending	2018/02/03 2018/02/09	6	347.6°	41.6°	-9.8
4	Sentinel-1A Sentinel-1B	5 × 20 5 × 20	Descending	2018/02/05 2018/02/11	6	192.4°	34.2°	-44.0
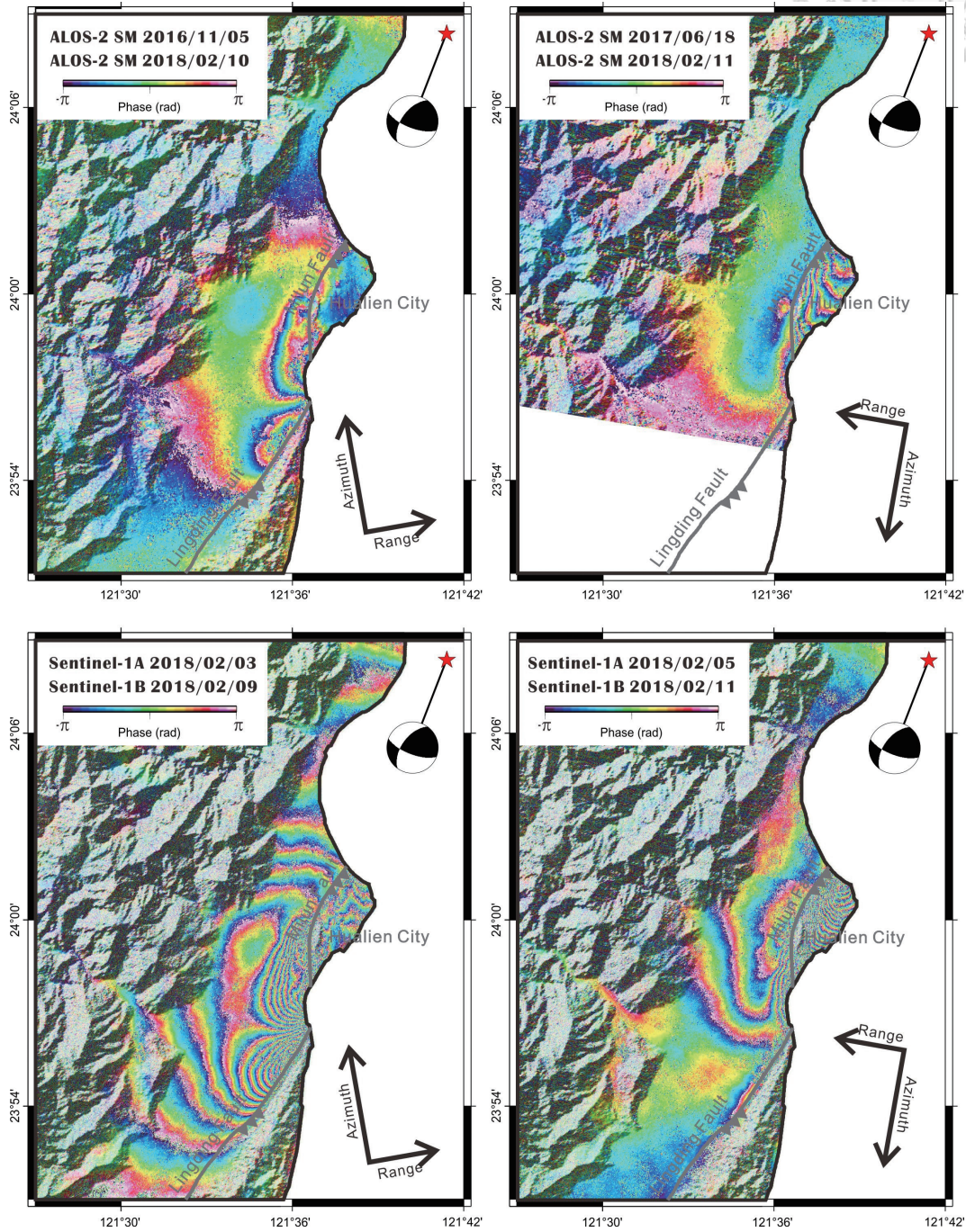
Fig. 3. Wrapped DInSAR interferograms derived from ALOS-2 (upper two figures) and Sentinel-1 radar images (lower two figures) acquired before and after the M_w 6.4 Hualien Earthquake.
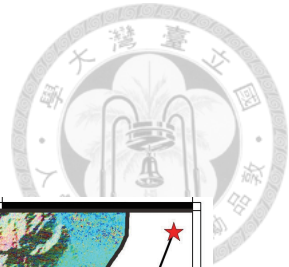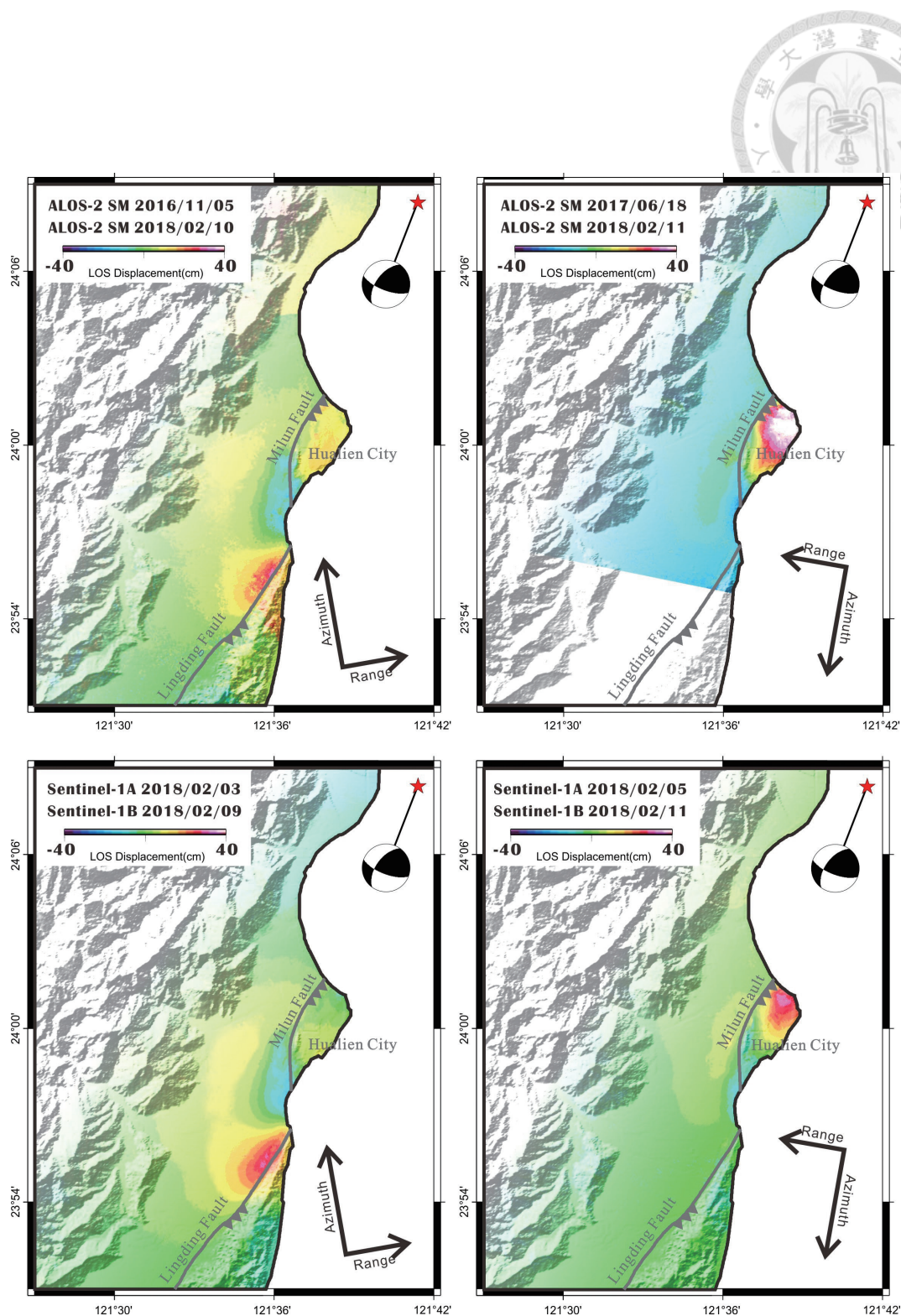
Fig. 4. Unwrapped DInSAR deformation derived from ALOS-2 (upper two figures) and Sentinel-1 radar images (lower two figures) acquired before and after the M_w 6.4 Hualien Earthquake by using Snaphu version 1.4.2 (Chen and Zebker 2000).

Table 2. cGPS coseismic displacements of the M_w 6.4 Hualien earthquake.

Station	Longitude (°)	Latitude (°)	1-s solutions			30-s solutions			24-h static solutions		
			N (mm)	E (mm)	U (mm)	N (mm)	E (mm)	U (mm)	N (mm)	E (mm)	U (mm)
HGC8	121.6051	24.1157				-87.5 ± 4.2	2.8 ± 3.8	29.7 ± 10.6			
HGC9	121.6128	23.9902				469.0 ± 14.2	41.3 ± 12.9	150.5 ± 32.0			
HUAL	121.6135	23.9754	414.1 ± 4.3	146.3 ± 5.4	42.3 ± 16.2	446.7 ± 9.7	156.5 ± 8.2	112.1 ± 27.0	432.0 ± 2.9	167.7 ± 7.0	59.2 ± 3.0
HUAP	121.7464	24.3090	-16.8 ± 5.6	9.4 ± 6.3	-23.1 ± 20.9	37.8 ± 21.6	17.4 ± 12.8	14.4 ± 58.6	-77.6 ± 5.2	20.0 ± 3.4	-31.1 ± 8.9
NDH1	121.5956	23.9624	-279.9 ± 1.9	25.3 ± 4.5	-41.0 ± 9.7	-283.8 ± 4.3	32.2 ± 4.7	-17.1 ± 14.8			
NDH3	121.5653	23.9955	-112.5 ± 1.8	-120.7 ± 4.9	64.9 ± 10.8	-130.8 ± 5.9	-119.3 ± 4.4	45.5 ± 13.9			
NDH4	121.5199	23.9168	-48.1 ± 2.0	-81.1 ± 4.4	8.9 ± 11.0	-40.6 ± 4.7	-88.5 ± 2.9	23.9 ± 7.9			
NDH5	121.6181	24.0100	170.3 ± 2.1	58.5 ± 4.9	74.1 ± 12.2	166.4 ± 3.9	55.4 ± 3.0	112.9 ± 7.1			
NDHU	121.5508	23.8972	-28.6 ± 2.7	-90.0 ± 4.2	16.4 ± 9.1	-45.7 ± 8.6	-83.0 ± 6.2	69.9 ± 19.4	-64.5 ± 3.3	-94.7 ± 1.8	32.6 ± 2.8
PEPU	121.6103	24.0179	-270.0 ± 6.6	-41.4 ± 12.7	88.3 ± 10.5	-273.9 ± 17.3	-68.6 ± 23.1	65.2 ± 61.7	-286.1 ± 7.4	-53.9 ± 3.4	51.2 ± 7.9
SCHN	121.6516	24.1278	-94.2 ± 4.1	6.4 ± 2.3	-22.6 ± 10.5				-136.1 ± 7.7	29.7 ± 8.7	-30.9 ± 7.1
SICH	121.6544	24.1257	-94.8 ± 3.8	3.2 ± 4.2	-32.6 ± 11.4	-65.7 ± 6.2	14.4 ± 4.2	45.6 ± 14.8			
SOFN	121.5982	23.8703	103.5 ± 4.4	-17.5 ± 4.6	41.8 ± 9.7	84.7 ± 12.9	8.2 ± 14.0	75.6 ± 65.4			
YENL	121.6018	23.9035	192.0 ± 3.0	-16.8 ± 4.0	-52.8 ± 11.0	204.3 ± 4.8	-24.5 ± 5.4	-31.0 ± 14.6	188.5 ± 2.3	-12.9 ± 2.0	-34.4 ± 5.7

Milun fault also show significant northeastward horizontal displacement of 175 and 470 mm and uplift of about 100 and 150 mm, respectively. In contrast, on the footwall of the Milun fault, the GPS station PEPU recorded a horizontal displacement of about 280 mm trending to the southwest and a coseismic uplift of about 70 mm. The coseismic motion indicates Milun fault is a left-lateral strike-slip faults with reverse motion which is consistent with the reverse sense based on geological investigations and kinematic behavior of coseismic deformation of the 1951 M_L 7.1 Hualien earthquake (e.g., Hsu 1962, 1971; Bonilla 1975, 1977; Yamaguchi and Ota 2004).

Further south, the GPS station YENL located on the hanging wall of the Lingding fault measured a horizontal displacement of about 200 mm trending to the northwest and a coseismic subsidence of 35 mm; the station NDHU located on the footwall of the Lingding Fault shows a coseismic uplift behavior, the vertical motion of these two stations is inconsistent with the kinematic behavior of the Lingding fault considered as a NS-striking east-dipping reverse fault with left-lateral slip component from geological investigations (Chen et al. 2007) and geodetic measurements during the interseismic period (Chen 1974; Yu and Liu 1989; Yu and Kuo 2001). Thus an unknown west-dipping fault with left-lateral strike-slip component could be triggered during this M_w 6.4 Hualien event.

3.2 D-InSAR Result

D-InSAR is complementary with GPS observations but with more spatial extensive measurements. The main surface deformation with numerous of fringes in interferograms can be observed around the Milun fault and northern Lingding fault. In contrast, only two fringes (representing 56 mm in range difference) are observed from the ascending orbit of Sentinel-1 near the epicenter (Fig. 3). After phase unwrapping, a significant shortening along the LOS can be observed on the hanging wall of the Milun fault in the descending orbit, which implies coseismic uplift and/or eastward motion in this area. Significant shortening along the LOS is presented on the footwall of the Lingding fault in the ascending orbit, suggesting a coseismic uplift and/or a westward motion dominated in this area (Fig. 4).

One of the limitations of for detecting deformation with InSAR is that it only provides one component of the surface deformation along line of sight (LOS) towards the satellite. Previous studies have investigated to map surface deformation in three dimensions by using multiple interferograms with different imaging geometries (e.g., Wright et al. 2004; Biggs et al. 2007). In general, the north-south component of surface deformation is always the most difficult to detect with the lager errors than the signals using data from near-polar orbiting satellites. If we assume north-south component is negligible, the eastward and vertical motion

can be well determined. However, the coseismic deformation along the NE-striking left-lateral strike-slip Milun fault is not the case for the assumption of negligible north-south component, because the north-south component of deformation is significant. For measuring coseismic deformation the, the pixel offset tracking techniques have been applied to characterize the coseismic deformation of the Milun fault (Huang and Huang 2018; Kuo et al. 2019; Yen et al. 2019). These studies provide the valuable information for coseismic deformation along and across the left-lateral strike-slip dominated Milun fault. However, the accuracy of the sub-pixel correlation method highly depends on pixel size. Previous studies suggested that the sub-pixel correlation method using a pair of SPOT panchromatic images could provide fault slip measurements with an accuracy of 0.1 pixel in theory (Michel and Avouac 2002; Dominguez et al. 2003; Leprince et al. 2007). For the coseismic deformation calculated by using offsets tracking with sub-pixel correlation of SAR amplitude (Simons et al. 2002; Fialko et al. 2005; Pathier et al. 2006; Elliott et al. 2007; Huang and Huang 2018), however this technique does not directly provide horizontal displacement. It measures track-parallel (azimuth offsets) and track-perpendicular (range offsets) displacement components (Fialko et al. 2005), thus the east-west and north-south component could be inferred according to azimuth and range offsets. In addition, the accuracy of the displacement filed inferred from offset tracking technique is affected by topographic complexity of the study area and ionospheric distortions. That could be the reason why Huang and Huang (2018) didn't incorporate the offset tracking coseismic deformation filed near the Milun fault in their inversion of rupture model of the Hualien.

To better characterize the coseismic deformation pattern around the Milun and Lingding faults, we combined ascending and descending interferograms to obtain E-W and vertical displacement components (Fig. 5) by following equations:

$$E_{component} = \frac{LOS^{(des)} \cdot \cos(\theta_{asc}) - LOS^{(asc)} \cdot \cos(\theta_{des})}{\cos(\alpha_{des}) \cdot \sin(\theta_{des}) \cdot \cos(\theta_{asc}) + \cos(\alpha_{asc}) \cdot \sin(\theta_{asc}) \cdot \cos(\theta_{des})} \quad (1)$$

$$U_{component} = \frac{LOS^{(asc)} + E_{component} \cdot \cos(\alpha_{asc}) \cdot \sin(\theta_{asc})}{\cos(\theta_{asc})} \quad (2)$$

Where θ is the incidence angle and α is intersection angle between the trace of satellite (Heading Angle) and the north; *asc* represents ascending orbit while *des* represents descending orbit (Table 1). Results obtained from ALOS-2 and Sentinel-1 both show that the uplift area is mainly located on the hanging wall of the Milun fault with the maximum uplift of 55 mm. Meanwhile, minor coseismic uplift is also observed on both sides of the Lingding fault. The maximum coseismic subsidence, reaching to 35 mm, is located in the southmost
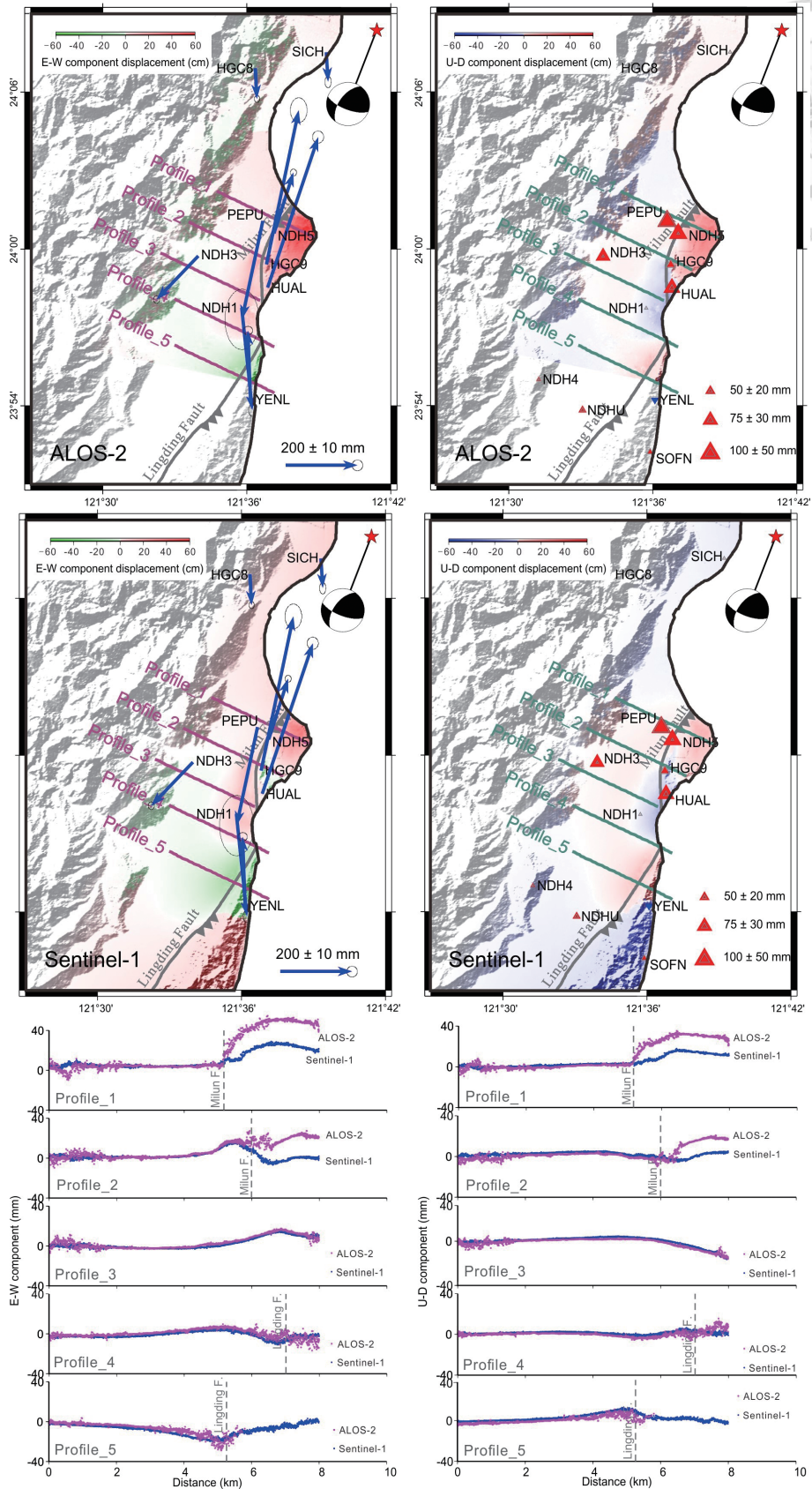
Fig. 5. E-W and vertical component coseismic deformation and profiles across the main deformation area. Red color represents eastward surface rupture and uplift; green color represents westward movement and blue color represents subsidence. Blue arrows represent the GPS horizontal displacements and solid triangles indicate the vertical movements of cGPS stations. Pink dots in profiles represent the deformation signals extracted from ALOS-2, and blue dots represent the deformation signals extracted from Sentinel-1.

footwall of the Milun fault. In general, the coseismic uplift obtained using ALOS-2 data is larger compared to that from Sentilnel-1 data. This difference could have resulted from the ionosphere effect of ALOS-2 pairs.

Five profiles across the main deformation area are shown in Fig. 5. Significant coseismic uplift is observed in the hanging wall of the Milun fault along profiles 1 and 2 in both ALOS-2 and Sentinel-1 data. Furthermore, coseismic uplift is larger in the northern part of the hanging wall of the Milun fault compared to that in the southern part of the hanging wall. On the other hand, moderate coseismic uplift can be observed on the footwall of the Lingding fault, this observation is inconsistent with the kinematic behavior for a NE-striking and east-dipping left-lateral strike-slip fault with a reverse component (Chen et al. 2007). It is worth noting that significant coseismic subsidence observed in an area separating the Milun fault and Lingding fault. For E-W coseismic component, the significant eastward motion of about 55 and 30 mm are observed in ALOS-2 and Senti-nel-1 images on the hanging wall of the Milun fault, respec-tively (Profiles 1 and 2 in left panel of Fig. 5). Although In-SAR technique could not well detect along-track coseismic displacement (subparallel to the strike of the Milun fault), however if we decompose of the fault-parallel displacement revealed by the optical image correlation of aerial photos (the maximum offset of 1 m from Kuo et al. 2019) and field survey (the maximum offset of ~ 77 cm from Huang et al. 2019), the eastward motions are consistent with our results. The main westward coseismic motion dominates in the footwall of the Lingding fault, which is consistent with the observation from GPS stations showing a NW motion in this area. Thus, the coseismic uplift and westward mo-tion also imply that an unknown west-dipping fault system might exist close to the Lingding fault.

4. DISCUSSION

4.1 Hourly Solution

24-hour static solution at GPS station HUAP and SCHN located at northern Hualien show a significant sub-sidence of 31 mm (Table 2). However, estimates of vertical motion from the kinematic solutions do not show the same feature (subsidence of 20 mm in 1-s and uplift of 14 mm in 30-s solutions). Thus, we divide daily data into 6 hours' intervals for static positioning. Here we use two stations HUAP and HUAL to show the time series of 6-hours solu-tions prior to, during and post the 0204 M_w 6.0 event and the 0206 event (Fig. 6). The subsidence and southeastward displacement could only be observed in stations (HGC1~7 and HUAP) located northwest to the epicenter of the 0204 M_w 6.0 event. In contrast, coseismic displacement of 0204 M_w 6.0 event is insignificant at the station HUAL in the city of Hualien. Thus, we suggest that the coseismic vertical motion of HUAP is contaminated by the 0204 event and

kinematic solutions will be useful to distinguish coseismic displacements of multi-events occurred in a short time span compared to the daily solutions.

4.2 Seismic Ground Motion - Peak Ground Displacement

Following the study of magnitude scaling properties of peak ground displacement (Melgar et al. 2015), Eq. (1) is used to determine peak ground displacement, where N(t), E(t), and U(t) are the north, east, and vertical displacement in each epoch, respectively.

$$PGD = \max\left[\sqrt{N(t)^2 + E(t)^2 + U(t)^2}\right] \qquad (3)$$

The peak ground displacement (PGD) derived from GPS waveform in Stations HUAL and PEPU are shown in Fig. 7, the PGD is about 1135 and 386 mm, respectively. We also use the waveform data from two strong motion seis-mometers HWA019 and HWA028 close to GPS stations HUAL and PEPU to compare with the GPS displacement waveform. The good agreement from two data set suggests the high-rate GPS measurements could be used as strong mo-tion data. In addition, we also calculated the arrival time of the PGD estimated from GPS waveforms. Surprisingly, the earliest arrival time of 12 s recorded at the both sides of the Milun fault from 4 GPS stations (PEPU, NDH5, NDH1, and HUAL) and shows a southward increase (Fig. 8). However, two GPS stations SCHN and SICH located in Hsinchen near the epicenter of the 0206 event revealed an arrival time of the PGD of about 15 s. If we assume the S wave velocity of 6.5 km s^{-1}, the shear wave should arrival at these two stations in about only 3 s. This implies that the PGD observed in the epicenter area and along the Milun fault should resulted from the triggered Milun fault after the mainshock.

4.3 Candidate of Unknown West-Dipping Fault

Yang et al. (2018) used three faults to explain the de-formation pattern derived from D-InSAR and GPS after the 0206 event. They suggested a NE-striking and west-dipping fault subparallel to the east-dipping Lingding fault respon-sible for the observed deformation pattern. An alternative fault model proposed by Lee et al. (2019) by using joint inversion of teleseismic and GPS data suggesting a fault-to-fault jumping rupture. They implied that both the slip on Milun and Lingding faults were triggered by 0206 event. They suggested that the initial rupture started from a N-S striking and west-dipping fault and propagated southward with a high rupture speed, then the rupture then jumped to the shallower east-dipping Milun fault. The rupture jumped again to the east-dipping Lingding fault. Wen et al. (2019) also suggested the mainshock ruptured southward on two

fault segments, with a weak but fast imitation in the main west dipping segment and low yet significant slip on shallow east-dipping segment. Moreover, Huang and Huang (2018) suggested this event initiated from a south-dipping fault in offshore near Hsinchen ridge, and slip transferred in to the main west-dipping oblique fault and the east-dipping Milun fault in order by applied joint inversion of seismic, GPS, InSAR, and leveling data. They consider the main west-dipping main fault belongs to a different fault system that is different from the east-dipping Longitudinal Valley fault system (LVF). The west-dipping fault and easting-dipping LVF could be very close in the shallow depth, but close in space at the shallowest part. However, Yen et al. (2019) used 3D displacement field and numerical modeling to characterize the coseismic behavior of the Milun and Lingding faults. They suggest that the Milun and Lingding

faults merge downward into a fault zone, thus they inferred that the Milun and Lingding faults belong to same fault zone with similar kinematic behavior during the Hualien event. This suggestion is quite different with previous models which suggest the west-dipping fault is the major seismogenic fault or trigger rupture around the Lingding fault during the Hualien event (Huang and Huang 2018; Yang et al. 2018; Lee et al. 2019; Wen et al. 2019).

In addition, the M_L 6.4 Ruisui earthquake occurred in the Central Range of eastern Taiwan in 2013 also gave a clue for the existence of NE-striking and west-dipping seismogenic fault in Central Range. The seismogenic fault responsible for the surface deformation was a NNE-SSW-striking and west-dipping fault with a major slip located at a depth between 10 and 20 km (Lee et al. 2014). The seismogenic fault was considered as the central segment of the
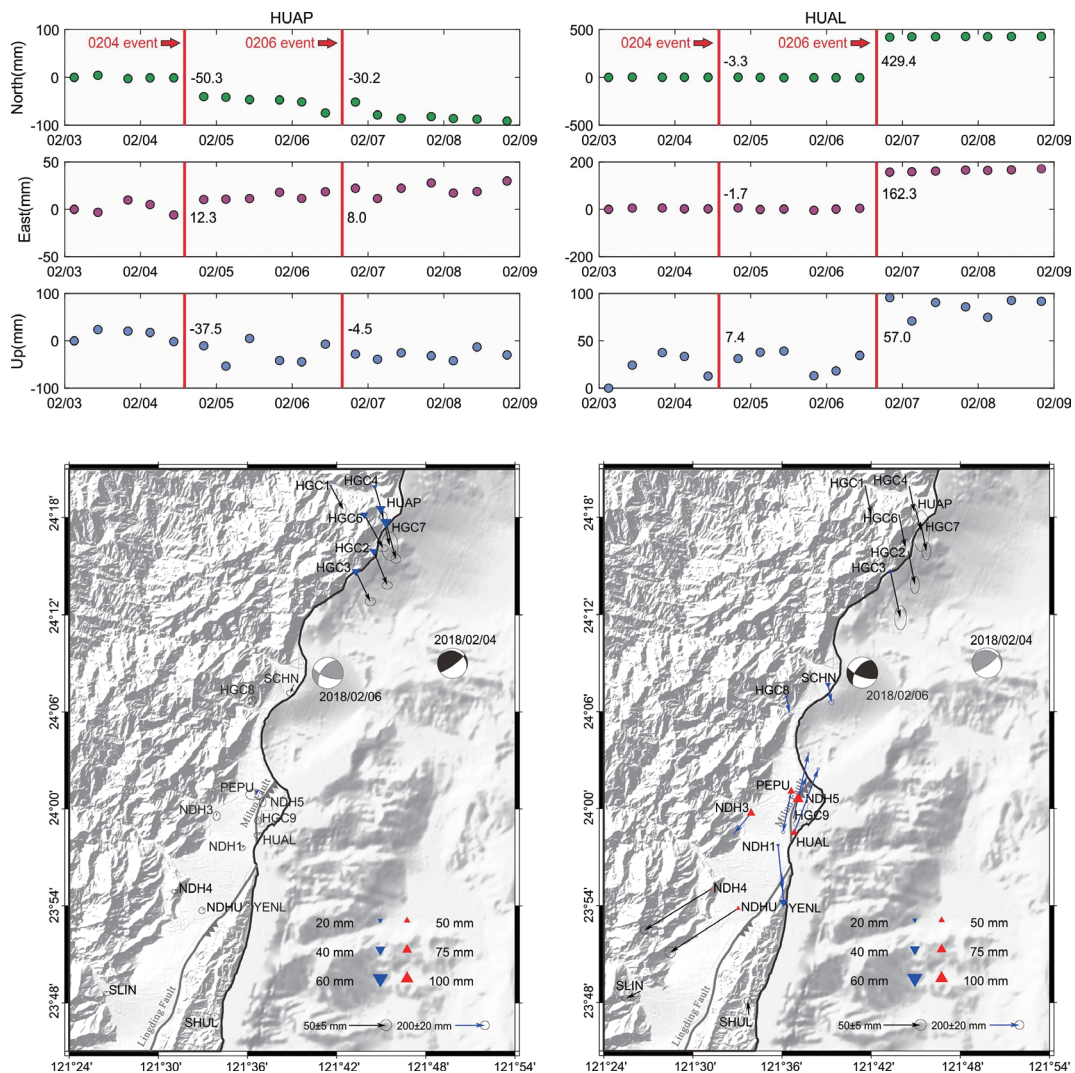

Fig 6. Upper-panel: time-series of cGPS stations HGC7 and HUAL. Two gray lines represent occurring time of the two main shocks of the 0204 M_w 6.0 and 0206 M_w 6.4 events. Numbers represent the coseismic displacements in three components of the two earthquakes. Lower-panel: coseismic displacement of 6-hours solutions of continuous GPS stations for the 0204 (left) and 0206 (right) events. Blue and black arrows represent the GPS horizontal displacements and solid triangles indicate the vertical movements of cGPS stations.
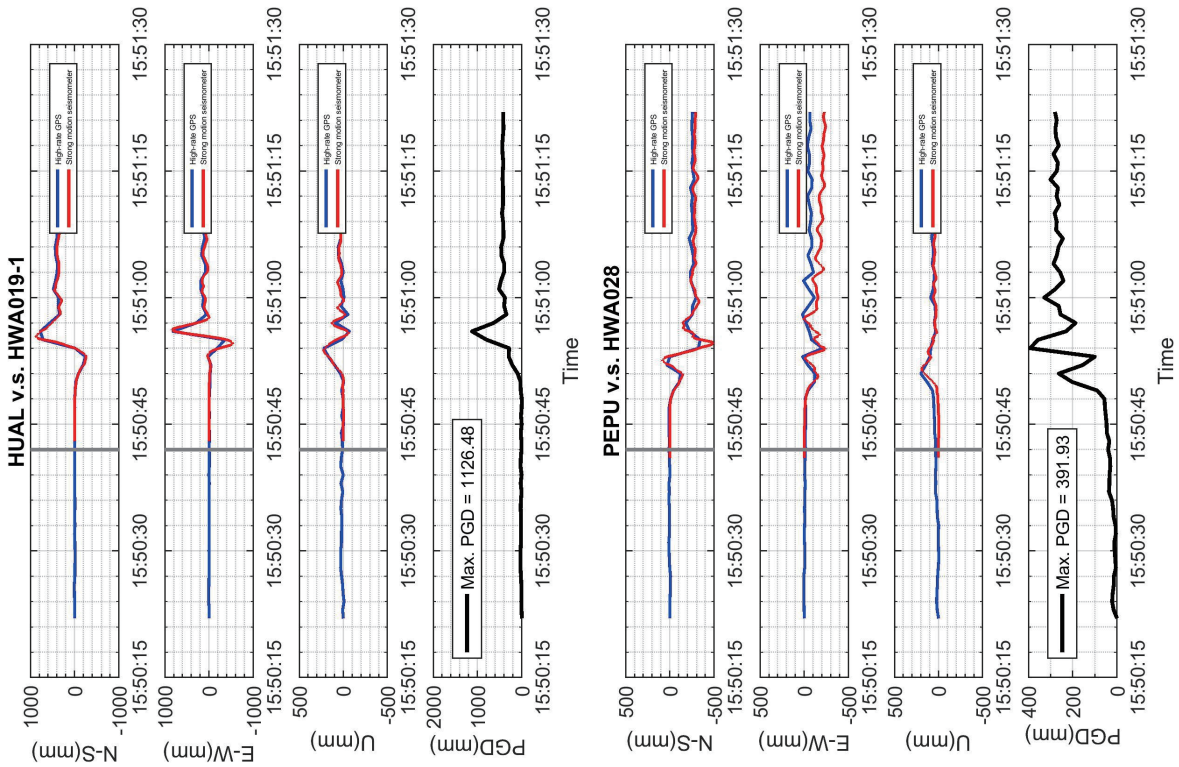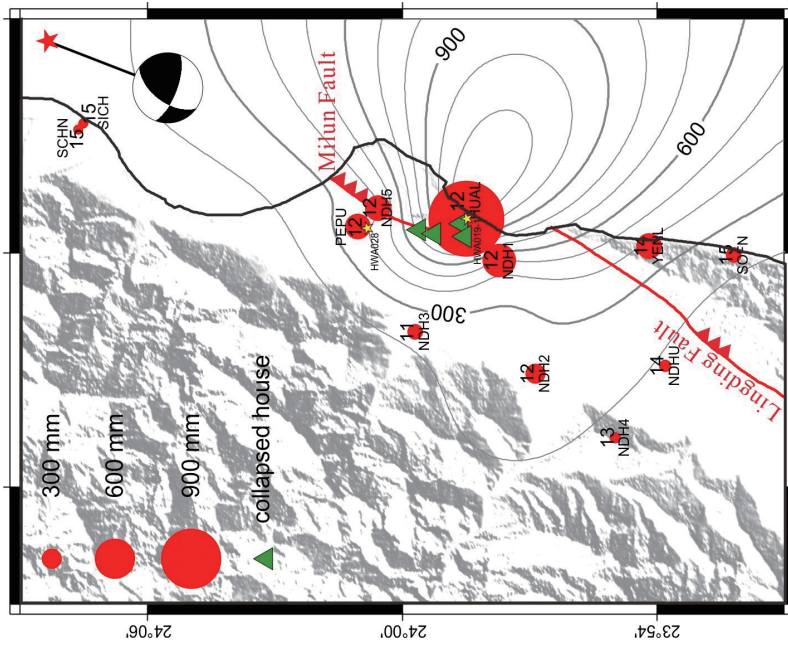
Fig. 8. Peak ground displacement estimation based on epoch-by-epoch solution from high-rate (1-Hz) GPS data. The size of red circles represents the amplitudes of the PGD for each station, and the number represents the arrival time of the PGD in second. The contour lines of PGD values are shown in gray lines.

Fig 7. Comparison of GPS displacement waveform in N-S, E-W and vertical (U) components with adjacent strong motion stations and the Peak Ground Displacement (PGD) derived from GPS waveforms used in this study. Locations of GPS station and strong motion stations are shown in Fig. 8.

Central Range fault, where fault tip could propagate to a shallow depth intersecting with the NE-striking and east-dipping Longitudinal Valley fault (Fig. 9, profile BB'). The west-dipping Central Range Fault has been also observed along the northern segment near the Hualien area as revealed by a study of repeating earthquakes (Chen et al. 2009). This west-dipping Central Range Fault is also proposed cutting across the Lingding fault by geological profile (Fig. 9, modified from Chen 2016). Based on tomography data, focal mechanism and background seismicity, this NE-striking and west-dipping Central Range fault could extend offshore up to the epicenter area of the 0206 event (Wen-Shan Chen, personal communication), this tectonic model could support the possible candidate of the west-dipping fault which was triggered during the 0206 M_w 6.4 Hualien event.

5. CONCLUSION

In this study, we investigate the coseismic deformation field associated with the 2018 M_w 6.4 Hualien earthquake using GPS data and four tracks of InSAR measurement. The GPS-derived coseismic deformation based on kinematic and static positioning show significant coseismic deformation occurred along the Milun fault and extended southward to the northern part of the Lingding fault. The InSAR-derived coseismic deformation field shows similar features with most deformation located on the both sides of the Milun fault and in the footwall of the Lingding fault. In summary, the major coseismic deformation zone occurred along the Milun fault and in the footwall of the Lingding fault far from the epicenter. Additionally, the arrival time of
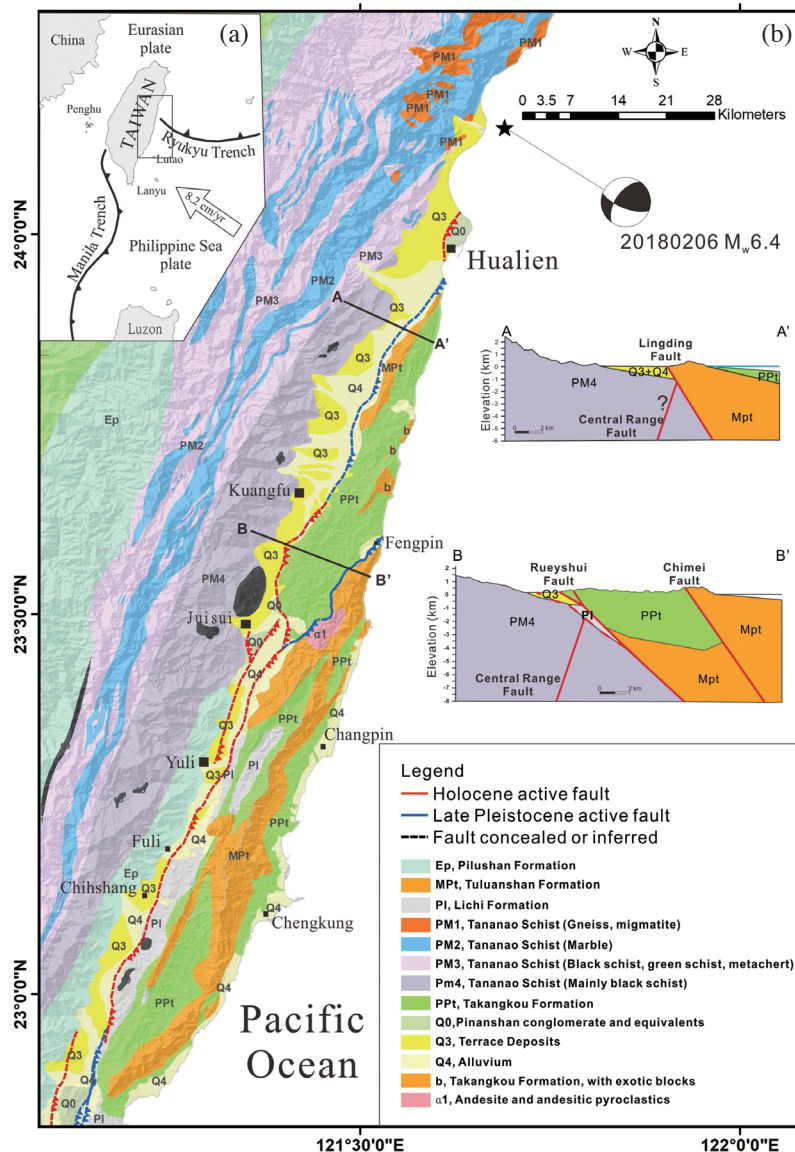

Fig. 9. (a) Simplified tectonic framework of eastern Taiwan and location of the geological map. (b) Simplified geological map of eastern Taiwan with two geological profiles across the Lingding and Ruisui fault (modified from Chen 2016).

the peak ground motion based on high-rate GPS waveforms indicate a long delay compared to a typical wave propagation velocity, suggesting the hypothesis of multi-fault slip triggering during the 0206 event.

REFERENCES

Biggs, J., T. Wright, Z. Lu, and B. Parsons, 2007: Multi-interferogram method for measuring interseismic deformation: Denali Fault, Alaska. *Geophys. J. Int.*, **170**, 1165-1179, doi: 10.1111/j.1365-246X.2007.03415.x. [Link]

Bock, Y., L. Prawirodirdjo, and T. I. Melbourne, 2004: Detection of arbitrarily large dynamic ground motions with a dense high-rate GPS network. *Geophys. Res. Lett.*, **31**, L06604, doi: 10.1029/2003GL019150. [Link]

Bonilla, M. G., 1975: A review of recently active faults in Taiwan. U.S. Geological Survey Open-File Report, 75-41, 58 pp.

Bonilla, M. G., 1977: Summary of Quaternary faulting and elevation changes in Taiwan. *Mem. Geol. Soc. China*, **2**, 43-55.

Chang, Y.-H., S.-H. Hung, and Y.-L. Chen, 2019: A fast algorithm for automatic phase picker and event location: Application to the 2018 Hualien earthquake sequences. *Terr. Atmos. Ocean. Sci.*, **30**, 435-448, doi: 10.3319/TAO.2018.12.23.01. [Link]

Chen, C. W. and H. A. Zebker, 2000: Network approaches to two-dimensional phase unwrapping: Intractability and two new algorithms. *J. Opt. Soc. Am.*, **17**, 401-414, doi: 10.1364/josaa.17.000401. [Link]

Chen, C.-Y., 1974: Verification of the north-northeastward movement of the Coastal Range, eastern Taiwan, by re-triangulation. *Bull. Geol. Surv. Taiwan*, **24**, 119-123. (in Chinese)

Chen, K. H., R.-J. Rau, and J.-C. Hu, 2009: Variability of repeating earthquake behavior along the Longitudinal Valley fault zone of eastern Taiwan. *J. Geophys. Res.*, **114**, B05306, doi: 10.1029/2007JB005518. [Link]

Chen, P.-F., Y.-L. Chen, P.-L. Su, Y.-D. Peng, and L.-F. Chen, 2019: Understanding the 6 February 2018, Hualien earthquake sequence through catalog compilation. *Terr. Atmos. Ocean. Sci.*, **30**, 399-409, doi: 10.3319/TAO.2018.11.15.02. [Link]

Chen, W.-S., 2016: Introduction of Geology in Taiwan. Geol. Soc. China, Taipei, 250 pp. (in Chinese)

Chen, W.-S., I.-C. Yen, K. P. Fengler, C. M. Rubin, C.-C. Yang, H.-C. Yang, H.-C. Chang, C.-W. Lin, W.-H. Lin, Y.-C. Liu, and Y.-H. Lin, 2007: Late Holocene paleoearthquake activity in the middle part of the Longitudinal Valley fault, eastern Taiwan. *Earth Planet. Sci. Lett.*, **264**, 420-437, doi: 10.1016/j.epsl.2007.09.043. [Link]

Dach, R., U. Hugentobler, P. Fridez, and M. Meindl, 2007: Bernese GPS Software Version 5.0, Astronomical Institute, University of Bern.

Dominguez, S., J.-P. Avouac, and R. Michel, 2003: Horizontal coseismic deformation of the 1999 Chi-Chi earthquake measured from SPOT satellite images: Implications for the seismic cycle along the western foothills of central Taiwan. *J. Geophys. Res.*, **108**, doi: 10.1029/2001JB000951. [Link]

Elliott, J. L., J. T. Freymueller, and B. Rabus, 2007: Coseismic deformation of the 2002 Denali fault earthquake: Contributions from synthetic aperture radar range offsets. *J. Geophys. Res.*, **112**, B06421, doi: 10.1029/2006JB004428. [Link]

Farr, T. G., P. A. Rosen, E. Caro, R. Crippen, R. Duren, S. Hensley, M. Kobrick, M. Paller, E. Rodriguez, L. Roth, D. Seal, S. Shaffer, J. Shimada, J. Umland, M. Werner, M. Oskin, D. Burbank, and D. Alsdorf, 2007: The shuttle radar topography mission. *Rev. Geophys.*, **45**, RG2004, doi: 10.1029/2005RG000183. [Link]

Fialko, Y., D. Sandwell, M. Simons, and P. Rosen, 2005: Three-dimensional deformation caused by the Bam, Iran, earthquake and the origin of shallow slip deficit. *Nature*, **435**, 295-299, doi: 10.1038/nature03425. [Link]

Hamling, I. J., S. Hreinsdóttir, K. Clark, J. Elliott, C. Liang, E. Fielding, N. Litchfield, P. Villamor, L. Wallace, T. J. Wright, E. D'Anastasio, S. Bannister, D. Burbidge, P. Denys, P. Gentle, J. Howarth, C. Mueller, N. Palmer, C. Pearson, W. Power, P. Barnes, D. J. A. Barrell, R. Van Dissen, R. Langridge, T. Little, A. Nicol, J. Pettinga, J. Rowland, and M. Stirling, 2017: Complex multifault rupture during the 2016 M_w 7.8 Kaikōura earthquake, New Zealand. *Science*, **356**, eaam7194, doi: 10.1126/science.aam7194. [Link]

Herring, T. A., R. W. King, and S. C. McClusky, 2009: Introduction to GAMIT/GLOBK, Release 10.35, Mass. Inst. of Technol., Cambridge.

Hsu, M.-T., 1971: Seismicity of Taiwan and some related problems. *Bull. Intern. Inst. Seismol. Earthq. Eng.*, **8**, 41-160.

Hsu, T.-L., 1962: Recent faulting in the longitudinal valley of eastern Taiwan. *Mem. Geol. Soc. China*, **1**, 95-102.

Huang, M.-H. and H.-H. Huang, 2018: The Complexity of the 2018 M_w 6.4 Hualien Earthquake in East Taiwan. *Geophys. Res. Lett.*, **45**, 13249-13257, doi: 10.1029/2018GL080821. [Link]

Huang, M.-H., H. Tung, E. J. Fielding, H.-H. Huang, C. Liang, C. Huang, and J.-C. Hu, 2016: Multiple fault slip triggered above the 2016 M_w 6.4 MeiNong earthquake in Taiwan. *Geophys. Res. Lett.*, **43**, 7459-7467, doi: 10.1002/2016GL069351. [Link]

Huang, S.-Y., J.-Y. Yen, B.-L. Wu, I.-C. Yen, and R. Y. Chuang, 2019: Investigating the Milun Fault: The coseismic surface rupture zone of the 2018/02/06 M_L 6.2 Hualien earthquake, Taiwan. *Terr. Atmos. Ocean. Sci.*, **30**, 311-335, doi: 10.3319/TAO.2018.12.09.03. [Link]

Kuo, Y.-T., Y. Wang, J. Hollingsworth, S.-Y. Huang, R. Y. Chuang, C.-H. Lu, Y.-C. Hsu, H. Tung, J.-Y. Yen, and C.-P. Chang, 2019: Shallow fault rupture of the Milun fault in the 2018 M_w 6.4 Hualien earthquake: A high-resolution approach from optical correlation of Pléiades satellite imagery. *Seismol. Res. Lett.*, **90**, 97-107, doi: 10.1785/0220180227. [Link]

Kuo-Chen, H., Z.-K. Guan, W.-F. Sun, P.-Y. Jhong, and D. Brown, 2019: Aftershock sequence of the 2018 M_w 6.4 Hualien earthquake in eastern Taiwan from a dense seismic array data set. *Seismol. Res. Lett.*, **90**, 60-67, doi: 10.1785/0220180233. [Link]

Le Béon, M., M.-H. Huang, J. Suppe, S.-T. Huang, E. Pathier, W.-J. Huang, C.-L. Chen, B. Fruneau, S. Baize, K. E. Ching, and J.-C. Hu, 2017: Shallow geological structures triggered during the M_w 6.4 Meinong earthquake, southwestern Taiwan. *Terr. Atmos. Ocean. Sci.*, **28**, 663-681, doi: 10.3319/TAO.2017.03.20.02. [Link]

Lee, S.-J., H.-H. Huang, J. B. H. Shyu, T.-Y. Yeh, and T.-C. Lin, 2014: Numerical earthquake model of the 31 October 2013 Ruisui, Taiwan, earthquake: Source rupture process and seismic wave propagation. *J. Asian Earth Sci.*, **96**, 374-385, doi: 10.1016/j.jseaes.2014.09.020. [Link]

Lee, S.-J., T.-C. Lin, T.-Y. Liu, and T.-P. Wong, 2019: Fault-to-fault jumping rupture of the 2018 Mw 6.4 Hualien earthquake in eastern Taiwan. *Seismol. Res. Lett.*, **90**, 30-39, doi: 10.1785/0220180182. [Link]

Leprince, S., S. Barbot, F. Ayoub, and J.-P. Avouac, 2007: Automatic and precise orthorectification, coregistration, and subpixel correlation of satellite images, application to ground deformation measurements. *IEEE Trans. Geosci. Remote Sensing*, **45**, 1529-1558, doi: 10.1109/TGRS.2006.888937. [Link]

Lin, K.-C., J.-C. Hu, K.-E. Ching, J. Angelier, R.-J. Rau, S.-B. Yu, C.-H. Tsai, T.-C. Shin, and M.-H. Huang, 2010: GPS crustal deformation, strain rate, and seismic activity after the 1999 Chi-Chi earthquake in Taiwan. *J. Geophys. Res.*, **115**, B07404, doi: 10.1029/2009JB006417. [Link]

Lin, K.-C., B. Delouis, J.-C. Hu, J.-M. Nocquet, and L. Mozziconacci, 2016: Reassessing the complexity of the rupture of the 2010 Jia-Shian Earthquake (M_w 6.2) in Southwestern Taiwan by inverting jointly teleseismic, strong-motion and CGPS data. *Tectonophysics*, **692**, 278-294, doi: 10.1016/j.tecto.2015.09.015. [Link]

Lin, Y.-S., R. Y. Chuang, J.-Y. Yen, Y.-C. Chen, Y.-T. Kuo, B.-L. Wu, S.-Y. Huang, and C.-J. Yang, 2019: Mapping surface breakages of the 2018 Hualien earthquake by using UAS photogrammetry. *Terr. Atmos. Ocean. Sci.*, **30**, 351-366, doi: 10.3319/TAO.2018.12.09.02. [Link]

Malavieille, J., S. E. Lallemand, S. Dominguez, A. Deschamps, C.-Y. Lu, C.-S. Liu, P. Schnuerle, J. Angelier, J. Y. Collot, B. Deffontaines, M. Fournier, S. K. Hsu, J. P. Le Formal, S. Y. Liu, J. C. Sibuet, N. Thareau, F. Wang, and the ACT (Active Collision in Taiwan) Scientific Crew, 2002: Arc-continent collision in Taiwan: New marine observations and tectonic evolution. In: Byrne, T .B. and C.-S. Liu (Eds.), Geology and Geophysics of an Arc-Continent Collision, Taiwan, GSA Special Papers, Geological Society of America, Vol. 358, 187-211, doi: 10.1130/0-8137-2358-2.187. [Link]

Melgar, D., B. W. Crowell, J. Geng, R. M. Allen, Y. Bock, S. Riquelme, E. M. Hill, M. Protti, and A. Ganas, 2015: Earthquake magnitude calculation without saturation from the scaling of peak ground displacement. *Geophys. Res. Lett.*, **42**, 5197-5205, doi: 10.1002/2015GL064278. [Link]

Michel, R. and J.-P. Avouac, 2002: Deformation due to the 17 August 1999 Izmit, Turkey, earthquake measured from SPOT images. *J. Geophys. Res.*, **107**, doi: 10.1029/2000JB000102. [Link]

Nikolaidis, R. M., Y. Bock, P. J. de Jonge, P. Shearer, D. C. Agnew, and M. Van Domselaar, 2001: Seismic wave observations with the Global Positioning System. *J. Geophys. Res.*, **106**, 21897-21916, doi: 10.1029/2001jb000329. [Link]

Pathier, E., E. J. Fielding, T. J. Wright, R. Walker, B. E. Parsons, and S. Hensley, 2006: Displacement field and slip distribution of the 2005 Kashmir earthquake from SAR imagery. *Geophys. Res. Lett.*, **33**, L20310, doi: 10.1029/2006GL027193. [Link]

Rosen, P. A., E. Gurrola, G. F. Sacco, and H. Zebker, 2012: The InSAR scientific computing environment. EUSAR 2012, Proc. 9th European Conference on Synthetic Aperture Radar, Nuremberg, Germany, 730-733.

Shyu, J. B. H., K. Sieh, Y.-G. Chen, and C.-S. Liu, 2005: Neotectonic architecture of Taiwan and its implications

for future large earthquakes. *J. Geophys. Res.*, **110**, B08402, doi: 10.1029/2004jb003251. [Link]

Simons, M., Y. Fialko, and L. Rivera, 2002: Coseismic deformation from the 1999 M_w 7.1 Hector Mine, California, earthquake as inferred from InSAR and GPS observations. *Bull. Seismol. Soc. Am.*, **92**, 1390-1402, doi: 10.1785/0120000933. [Link]

Tian, S., P. Gardoni, and W. Yuan, 2019: Coseismic deformation of the 6 February 2018 M_w 6.2 Hualien Earthquake based on strong-motion recordings. *Seismol. Res. Lett.*, **90**, 108-117, doi: 10.1785/0220180235. [Link]

Tsai, M.-C., S.-B. Yu, T.-C. Shin, K.-W. Kuo, P.-L. Leu, C.-H. Chang, and M.-Y. Ho, 2015: Velocity field derived from Taiwan continuous GPS array (2007 - 2013). *Terr. Atmos. Ocean. Sci.*, **26**, 527-556, doi: 10.3319/TAO.2015.05.21.01(T). [Link]

Webb, F. H. and J. F. Zumberge, 1997: An Introduction to GIPSY/OASIS II, JPL Publication D-11088.

Wen, Y.-Y., S. Wen, Y.-H. Lee, and K.-E. Ching, 2019: The kinematic source analysis for 2018 M_w 6.4 Hualien, Taiwan earthquake. *Terr. Atmos. Ocean. Sci.*, **30**, 377-387, doi: 10.3319/TAO.2018.11.15.03. [Link]

Wright, T. J., B. E. Parsons, and Z. Lu, 2004: Toward mapping surface deformation in three dimensions using InSAR. *Geophys. Res. Lett.*, **31**, L01607, doi: 10.1029/2003GL018827. [Link]

Wu, B.-L., J.-Y. Yen, S.-Y. Huang, Y.-T. Kuo, and W.-Y. Chang, 2019: Surface deformation of 0206 Hualien earthquake revealed by the integrated network of RTK GPS. *Terr. Atmos. Ocean. Sci.*, **30**, 301-310, doi: 10.3319/TAO.2019.05.27.01. [Link]

Yamaguchi, M. and Y. Ota, 2004: Tectonic interpretations of Holocene marine terraces, east coast of Coastal Range, Taiwan. *Quat. Int.*, **115-116**, 71-81, doi: 10.1016/S1040-6182(03)00097-1. [Link]

Yang, Y.-H., J.-C. Hu, H. Tung, M.-C. Tsai, Q. Chen, Q. Xu, Y.-J. Zhang, J.-J. Zhao, G.-X. Liu, J.-N. Xiong, J.-Y. Wang, B. Yu, C.-Y. Chiu, and Z. Su, 2018: Co-Seismic and Postseismic Fault Models of the 2018 Mw 6.4 Hualien Earthquake Occurred in the Junction of Collision and Subduction Boundaries Offshore Eastern Taiwan. *Remote Sens.*, **10**, doi: 10.3390/rs10091372. [Link]

Yen, J.-Y., C.-H. Lu, R. J. Dorsey, H. Kuo-Chen, C.-P. Chang, C.-C. Wang, R.-Y. Chuang, Y.-T. Kuo, C.-Y. Chiu, Y.-H. Chang, F. Bovenga, and W.-Y. Chang, 2019: Insights into seismogenic deformation during the 2018 Hualien, Taiwan, earthquake sequence from InSAR, GPS, and modeling. *Seismol. Res. Lett.*, **90**, 78-87, doi: 10.1785/0220180228. [Link]

Yu, S.-B. and C.-C. Liu, 1989: Fault creep on the central segment of the Longitudinal Valley Fault, eastern Taiwan. *Proc. Geol. Soc. China*, **32**, 209-231.

Yu, S.-B. and L.-C. Kuo, 2001: Present-day crustal motion along the Longitudinal Valley Fault, eastern Taiwan. *Tectonophysics*, **333**, 199-217, doi: 10.1016/s0040-1951(00)00275-4. [Link]